



N°d'ordre

NNT : 2022ISAL0115

THESE de DOCTORAT DE L'UNIVERSITE DE LYON
opérée au sein de
L'Institut National des Sciences Appliquées de Lyon

Ecole Doctorale N° EDA 034
(Matériaux de Lyon)

Spécialité de doctorat: Matériaux

Soutenue publiquement le 09/12/2022, par :
Meng LIANG

**Analysis of small-scale plasticity of bulk Cu-Zr
metallic glasses under deformation by
atomistic simulations**

Devant le jury composé de :

DEQUIDT, Alain	Professeur	Université Clermont Auvergne	Rapporteur
QIAO, Jichao	Professeur	Northwestern Polytechnical University	Rapporteur
MARTENS, Kirsten	Chargé de Recherche	Université Grenoble Alpes	Examinatrice
TANGUY, Anne	Professeur	INSA Lyon	Examinatrice
CHAZEAU, Laurent	Professeur	INSA Lyon	Directeur de thèse
FUSCO, Claudio	Maître de conférences	INSA Lyon	Co-directeur de thèse
MORTHOMAS, Julien	Maître de conférences	INSA Lyon	Invité
ALBARET, Tristan	Maître de conférences	Université Lyon 1	Invité

Département FEDORA – INSA Lyon - Ecoles Doctorales

SIGLE	ECOLE DOCTORALE	NOM ET COORDONNEES DU RESPONSABLE
CHIMIE	CHIMIE DE LYON https://www.edchimie-lyon.fr Sec. : Renée EL MELHEM Bât. Blaise PASCAL, 3e étage secretariat@edchimie-lyon.fr	M. Stéphane DANIELE C2P2-CPE LYON-UMR 5265 Bâtiment F308, BP 2077 43 Boulevard du 11 novembre 1918 69616 Villeurbanne directeur@edchimie-lyon.fr
E.E.A.	ÉLECTRONIQUE, ÉLECTROTECHNIQUE, AUTOMATIQUE https://edeea.universite-lyon.fr Sec. : Stéphanie CAUVIN Bâtiment Direction INSA Lyon Tél : 04.72.43.71.70 secretariat.edeea@insa-lyon.fr	M. Philippe DELACHARTRE INSA LYON Laboratoire CREATIS Bâtiment Blaise Pascal, 7 avenue Jean Capelle 69621 Villeurbanne CEDEX Tél : 04.72.43.88.63 philippe.delachartre@insa-lyon.fr
E2M2	ÉVOLUTION, ÉCOSYSTÈME, MICROBIOLOGIE, MODÉLISATION http://e2m2.universite-lyon.fr Sec. : Bénédicte LANZA Bât. Atrium, UCB Lyon 1 Tél : 04.72.44.83.62 secretariat.e2m2@univ-lyon1.fr	Mme Sandrine CHARLES Université Claude Bernard Lyon 1 UFR Biosciences Bâtiment Mendel 43, boulevard du 11 Novembre 1918 69622 Villeurbanne CEDEX sandrine.charles@univ-lyon1.fr
EDISS	INTERDISCIPLINAIRE SCIENCES-SANTÉ http://ediss.universite-lyon.fr Sec. : Bénédicte LANZA Bât. Atrium, UCB Lyon 1 Tél : 04.72.44.83.62 secretariat.ediss@univ-lyon1.fr	Mme Sylvie RICARD-BLUM Institut de Chimie et Biochimie Moléculaires et Supramoléculaires (ICBMS) - UMR 5246 CNRS - Université Lyon 1 Bâtiment Raulin - 2ème étage Nord 43 Boulevard du 11 novembre 1918 69622 Villeurbanne Cedex Tél : +33(0)4 72 44 82 32 sylvie.ricard-blum@univ-lyon1.fr
INFOMATHS	INFORMATIQUE ET MATHÉMATIQUES http://edinfomaths.universite-lyon.fr Sec. : Renée EL MELHEM Bât. Blaise PASCAL, 3e étage Tél : 04.72.43.80.46 infomaths@univ-lyon1.fr	M. Hamamache KHEDDOUCI Université Claude Bernard Lyon 1 Bât. Nautibus 43, Boulevard du 11 novembre 1918 69 622 Villeurbanne Cedex France Tél : 04.72.44.83.69 hamamache.kheddouci@univ-lyon1.fr
Matériaux	MATÉRIAUX DE LYON http://ed34.universite-lyon.fr Sec. : Yann DE ORDENANA Tél : 04.72.18.62.44 yann.de-ordenana@ec-lyon.fr	M. Stéphane BENAYOUN Ecole Centrale de Lyon Laboratoire LTDS 36 avenue Guy de Collongue 69134 Ecully CEDEX Tél : 04.72.18.64.37 stephane.benayoun@ec-lyon.fr
MEGA	MÉCANIQUE, ÉNERGÉTIQUE, GÉNIE CIVIL, ACOUSTIQUE http://edmega.universite-lyon.fr Sec. : Stéphanie CAUVIN Tél : 04.72.43.71.70 Bâtiment Direction INSA Lyon mega@insa-lyon.fr	M. Jocelyn BONJOUR INSA Lyon Laboratoire CETHIL Bâtiment Sadi-Carnot 9, rue de la Physique 69621 Villeurbanne CEDEX jocelyn.bonjour@insa-lyon.fr
ScSo	ScSo* https://edsciencessociales.universite-lyon.fr Sec. : Mélina FAVETON INSA : J.Y. TOUSSAINT Tél : 04.78.69.77.79 melina.faveton@univ-lyon2.fr	M. Bruno MILLY Université Lumière Lyon 2 86 Rue Pasteur 69365 Lyon CEDEX 07 bruno.milly@univ-lyon2.fr

*ScSo : Histoire, Géographie, Aménagement, Urbanisme, Archéologie, Science politique, Sociologie, Anthropologie

Acknowledgements

This thesis is the result of four years of research work conducted at the laboratory of Matériaux of Institut National des Sciences Appliquées Lyon. This thesis work would not have been accomplished without the support and assistance of the people to whom I wish to take this opportunity to express my sincere appreciation.

First of all, I would like to express my profound respect and gratitude to my supervisor, Prof. Laurent Chazeau, for providing invaluable guidance throughout this research. Discussions with him have always been a learning experience and gave me another point of view for my result. I sincerely thank him for all the confirmation and encouragement he made to relieve my anxiety and motivate.

Second, my deepest gratitude goes to my co-supervisor, Assistant professor Claudio Fusco, who was always there when I need assistance. He has taught me the methodology of numerical simulation, data analysis, presentation and scientific writing with endless patience, training me to be a qualified researcher. I warmly thank him for the suggestions and help he gave me, whether in the technical, scientific, professional and personal field.

Besides my supervisors, I would like to thank the rest of the jury members:

for their detailed reviews, insightful comments and presence on my defense, Assistant professor Julien Morthomas and Tristan Albaret, gave me patient guidance and unselfish assistance during my research.

In addition, I wish to thank China Scholarship Council (CSC) for the financial support during my PhD period, providing precious opportunity to continue my academic study.

I would like to express my acknowledgement to staffs and colleagues in MATEIS laboratory. Mme Antonia Riccobene, the secretary of laboratory, helped me solve many problems.

I would like to extend my thanks to my colleagues and friends, who gave me companionship, encouragement and comfort during my PhD period. Thanks to Dr. Guojian Lyu, Dr. Hang Guo, Dr. Pablo Griffiths, Dr. Robins Kumar and Mr. Junxiong Wang. They gave me much help in my

study and life in France. The activities with my colleagues left me colorful and unforgettable memory. Thanks to my dear Chinese friends: Dr. Xiaoting Zhang, Dr. Rongrong Zhang and Dr. Zexian Wang, for being always prepared to help for academic difficulties as well as accompany in my life.

At last but not least, I would like to express my deepest gratitude to my parents, my lovely young brother and my dear lover, for your unconditional love and cares. Thank you so much for always being with me.

Meng LIANG

9/21/2022

Contents

List of Figures	xiii
List of Tables	xiv
Abstract	1
Résumé	3
General Introduction	5
1 Introduction	9
1.1 General features of metallic glasses	10
1.2 Mechanical properties of metallic glasses	11
1.3 Application of metallic glasses	12
1.4 Atomic-level structure of metallic glasses	14
1.5 Atomic-scale deformation of metallic glasses	17
1.5.1 Free volume model	17
1.5.2 Atomic local shear transformation	19
1.5.3 Formation of shear bands	19
1.6 Eshelby's inclusions	23
1.7 Molecular Dynamics studies on metallic glasses	27
1.7.1 Studies about structure	27
1.7.2 Correlation between microstructure and plastic behavior	28
1.7.3 Effect on microstructure and mechanical properties	30
1.7.3.1 Cooling rate	30
1.7.3.2 Temperature	31

1.7.3.3	Composition	32
1.8	Improvement of plasticity	32
1.8.1	Composite metallic glasses	33
1.8.2	Pre-deformation	34
1.8.3	Thermal pre-treatment	34
1.9	Open questions	36
2	Methodology and modeling	37
2.1	Molecular dynamics simulation	38
2.1.1	Newton's equation and algorithms	38
2.1.2	Interatomic potentials	39
2.1.3	Ensemble of molecular dynamics simulation for an equilibrium system	40
2.1.4	Periodic boundary conditions	44
2.2	Structural analysis	45
2.2.1	Radial distribution function	45
2.2.2	Voronoi polyhedra	46
2.2.3	Local atomic shear strain	46
2.3	Construction of model and deformation	47
2.4	Analysis and mapping of plastic events	48
2.4.1	Definition of plastic events	48
2.4.2	Selection of attractors	50
2.4.3	Rearrangement of plastic events	52
2.4.4	Atomic displacement fitting	52
2.4.5	Fitting of the stress-strain curve	54
2.5	Conclusion	56
3	General analysis of the mechanical behavior of metallic glass from molecular dynamics simulation	57
3.1	Introduction	58
3.2	Effect of quenching rate	58
3.3	Effect of composition	66

CONTENTS

3.4	Effect of strain rate	73
3.5	Effect of temperature	76
3.6	Discussion and conclusion	79
4	Analysis of the plastic events at the origin of the macroscopic plasticity	81
4.1	Introduction	82
4.2	Effect of quenching rates and compositions on plastic events	82
4.2.1	Effect of quenching rates on plastic events	82
4.2.2	Influence of the metallic glass composition	89
4.3	Prospect for tensile tests	94
4.4	Discussion and conclusion	99
5	Effect of thermal cycling on metallic glasses	101
5.1	Introduction	102
5.2	Thermal cycling treatment	102
5.3	Effect of thermal cycling on metallic glasses with different initial quenching rates	103
5.4	Effect of thermal cycling for different metallic glass composition	111
5.5	Discussion and conclusion	117
	Conclusions and Perspectives	119
	Author's publications	123
	Appendix	125
	A Smoothing method	126
	Bibliography	129

List of Figures

1.1	Volume change as a function of temperature from liquid to solid state (the dashed red line represents the equilibrium liquid) [Ritter, 2012]	10
1.2	Microscope diagram of the atomic arrangement of crystalline and amorphous alloy.	11
1.3	Ashby plot of the strength vs. the elastic limit of different classes of materials: amorphous metallic alloys combine the higher strength of crystalline metal alloys with the elasticity of polymers [Telford, 2004].	12
1.4	Deformation of Zr-based MG in experiment [Zhang et al., 2003]. (a) Compressive strain-stress curve (b) Compression fracture morphology characteristics (c) Tensile strain-stress curve (b) Tensile fracture morphology characteristics	12
1.5	Application of MG. (a) Golf stick (b) Armor-piercing projectile (c) Amorphous transformer core (d) Amorphous gastroscope	13
1.6	The illustration of radial distribution function [Weihua, 2013].	14
1.7	$\langle 0,0,12,0 \rangle$ icosahedron in $Cu_{64}Zr_{36}$ metallic glass.	16
1.8	Representative atomic clusters for monatomic hafnium [Şengül and Çeltek, 2018].	16
1.9	SRO clusters connected by (a) VS, (b) ES, (c) FS, and (d) IS in the $Cu_{50}Zr_{50}$ metallic glass (Zr and Cu atoms are represented with blue and brown balls, respectively, and centered Zr and Cu atoms are represented using green and red balls, respectively) [Li et al., 2014].	17
1.10	Free volume model in the flow of metallic glass [Spaepen, 1977]. (a) Single atomic transition (b) Free volume generation	18

LIST OF FIGURES

1.11	The schematic of the relationship between α relaxation and β relaxation on potential energy landscape (PEL) [Ritter, 2012].	19
1.12	The schematic diagram of the temperature gradient of SB [Shimizu et al., 2006].	21
1.13	Diagram of formation of SB in the MG under compression loading(v_p is propagation velocity of structural disorder and v_s is shear velocity) [Greer et al., 2013].	21
1.14	Shear band of Zr-based metallic glass (a) High-resolution TEM image and (b) nanoscale voids within it [Li et al., 2002a].	22
1.15	Evolution of free volume and temperature during the shear localization process.	22
1.16	Scheme of inclusion's removal from the matrix and of its unconstrained transformation.	23
1.17	Applying force on the inclusion and putting it back in the matrix.	24
1.18	Releasing the surface traction of the inclusion.	25
1.19	Comparison of shear stress-strain curves for amorphous silicon with Stillinger and Weber (SW) potential [Stillinger and Weber, 1985] from MD simulations and with Eshelby's inclusion model. The black curve is the result of the MD simulation. Red, dashed blue and orange curves are obtained with Eshelby's inclusion model [Albaret et al., 2016].	27
1.20	Fractions of the five dominant polyhedra types as a function of sample strain in the region that evolves into the localized band [Cao et al., 2009].	29
1.21	The stress-strain curve (the red one), potential energy (the blue one), and unload-reload stress-strain curve (black) with strain [Cao et al., 2009]. . .	29
2.1	2-dimensional schematic diagram of periodic boundary conditions [Stepanov, 2013]. Filled circles to open circles mean the movement of atoms after displacement.	44
2.2	Schematic of atomic displacement calculation with and without minimum image convention.	45
2.3	The schematic diagram of forward deformation and reverse deformation.	48

2.4	2D projection of density of PE of amorphous silicon over the basins on xy plane at shear strain 1.6 % ($40 \text{ \AA} < z < 50 \text{ \AA}$) [Fusco et al., 2010].	49
2.5	Map of plastic energy, $PE(\mathbf{r})$ surrounding a plastic event (the intensity of plastic energy from low to high) corresponding to the color from blue to red [Fusco et al., 2010].	50
2.6	Radial distribution of plastic energy $PE(\mathbf{r})$ around the attractor and exponential fit curve [Albaret et al., 2016].	51
2.7	The distribution of nonaffine atomic displacements between two successive steps from MD simulation (a) and with Eshelby's inclusion model of $Cu_{64}Zr_{36}$ MG at strain 15 % during quasi-static shear deformation (b). Both images are replicated three times.	54
3.1	Volume as a function of temperature (V-T) of $Cu_{64}Zr_{36}$ MGs under different quenching rates (a) and the figure with shifted up curves (b).	58
3.2	Radial distribution function (RDF) of $Cu_{64}Zr_{36}$ MG at 0.1 K under different quenching rates.	60
3.3	The first peak (a) and the second peak (b) on the RDF curves of $Cu_{64}Zr_{36}$ MG at 0.1 K under different quenching rates.	60
3.4	The first peaks on Cu-Cu partial RDF curves (a), the first peaks on Cu-Zr partial RDF curves (b), and the first peaks on Zr-Zr partial RDF curves (c) of $Cu_{64}Zr_{36}$ MG with different quenching rates.	61
3.5	The first peak on RDF and partial RDF of $Cu_{36}Zr_{64}$ MG after quenching with a quenching rate of 10^{10} K/s at 0.1 K.	61
3.6	Shear stress-strain curves of $Cu_{64}Zr_{36}$ MG after quasi-static deformation with different quenching rates at 0.1 K.	62
3.7	Shear modulus (a), yield stress and strain (b), and flow stress (c) for $Cu_{64}Zr_{36}$ prepared with different quenching rates.	62
3.8	Map of atomic shear strain in $Cu_{64}Zr_{36}$ MG prepared with a quenching rate of 10^{10} K/s, sheared at 12.3 % strain (a) and 12.4 % (b), showing the atoms with shear strain larger than 60 % of the maximum atomic shear strain over the whole sample.	63

LIST OF FIGURES

3.9	The atomic shear strain in $Cu_{64}Zr_{36}$ MG prepared with different quenching rates at different shear strains, at 0.1 K.	64
3.10	Fraction of FI of $Cu_{64}Zr_{36}$ prepared with different quenching rates as a function of shear strain at 0.1 K.	65
3.11	Fraction of FI in SB region of $Cu_{64}Zr_{36}$ prepared with the quenching rate 10^{10} K/s as a function of shear strain.	65
3.12	Volume as a function of the temperature for the three different compositions quenched with a quenching rate of 10^{11} K/s. Dotted lines are to determine the glass transition temperature.	66
3.13	The total radial distribution function (RDF) for three compositions of binary Cu-Zr MGs quenched at 0.1 K at a quenching rate of 10^{11} K/s (a) and the magnification of the first peak (b).	67
3.14	Cu-Cu (a) and Zr-Zr (b) partial radial distribution function (PRDF) for three compositions of binary Zr-Cu MGs quenched at 0.1 K at a quenching rate of 10^{11} K/s. The insets in the Figures show a magnification of the first peaks.	67
3.15	The insets in the figures show a magnification of the first peaks. Magnification of the second peaks of the total RDF curves shown in Figure 3.13 (a).	68
3.16	Shear stress-strain curves of three compositions quenched at 0.1 K after quasi-static deformation at a quenching rate of 10^{11} K/s.	69
3.17	Shear modulus (a), yield stress (b), yield strain (c) and flow stress (d) of three compositions quenched at 0.1 K at a quenching rate of 10^{11} K/s.	69
3.18	Normalized shear stress-strain curves by the shear modulus (a) and shear modulus vs. yield stress (b) of three compositions quenched at 0.1 K at a quenching rate of 10^{11} K/s.	70
3.19	Map of atomic shear strain for the three compositions at strain 10.6 % (a), 10.7 % (b), 12.4 % (c), 15 % (d), and 20 % (e) at 0.1 K for a quenching rate of 10^{11} K/s.	70
3.20	Comparison of difference between yield and flow stress of three compositions.	71

3.21	Comparison of fraction of FI with shear strain for the three compositions.	72
3.22	Map of central atoms of FI for the three compositions (brown balls are Cu atoms, and green balls are Zr atoms).	72
3.23	Shear stress-strain curves with different strain rates for of $Cu_{64}Zr_{36}$ MG prepared with a 10^{11} K/s quenching rate at 0.1 K.	73
3.24	Shear modulus (a) and yield and flow stress (b) as a function of the different strain rates for $Cu_{64}Zr_{36}$ MG quenched at 0.1 K, at a quenching rate of 10^{11} K/s.	74
3.25	Distribution of atomic shear strain of $Cu_{64}Zr_{36}$ MGs with different strain rates, at strain 10 %, 12.5 %, 15 %, and 20 %, at 0.1 K.	74
3.26	Comparison of stress-strain curves of $Cu_{64}Zr_{36}$ MGs sheared with different strain rates, at three different temperatures: (a) 0.1 K, (b) 50 K, (c) 200 K.	75
3.27	Map of atomic shear strain of $Cu_{64}Zr_{36}$ MG at strain 30 % with strain rate of $10^7 s^{-1}$, $10^8 s^{-1}$ and $10^9 s^{-1}$ when the temperature is 50 K and 200 K.	75
3.28	The total RDF of $Cu_{64}Zr_{36}$ MG at different temperatures for quenching rate 10^{11} K/s (a), magnified first peak (b) and magnified second peak (c).	76
3.29	The Cu-Cu PRDF of $Cu_{64}Zr_{36}$ MG at different temperatures for quenching rate 10^{11} K/s (a), magnified first peak (b) and magnified second peak (c).	76
3.30	The Cu-Zr PRDF of $Cu_{64}Zr_{36}$ MG at different temperatures for quenching rate 10^{11} K/s (a), magnified first peak (b) and magnified second peak (c).	77
3.31	The Zr-Zr PRDF of $Cu_{64}Zr_{36}$ MG at different temperatures for quenching rate 10^{11} K/s (a), magnified first peak (b) and magnified second peak (c).	77
3.32	Shear stress-strain curves (a) and tensile stress-strain curves (b) of $Cu_{64}Zr_{36}$ MG at different temperatures and strain rate $10^8 s^{-1}$.	77
3.33	Shear modulus (a) and Young's modulus (b) of $Cu_{64}Zr_{36}$ MG deduced from shear tests and tensile tests at different temperatures and strain rate $10^8 s^{-1}$.	78
3.34	Distribution of atomic shear strain at 20 % strain at different temperatures and strain rate $10^8 s^{-1}$ (scale doubled in the y-direction to better visualize).	78
3.35	Fraction of FI of $Cu_{64}Zr_{36}$ MG quenched at different temperatures and sheared at the same temperature with a $10^8 s^{-1}$ shear strain rate.	78

LIST OF FIGURES

4.1	Cumulative numbers of plastic events with strain for $Cu_{64}Zr_{36}$ MG with different quenching rates.	82
4.2	Cumulative plastic intensity of plastic events for different quenching rates.	83
4.3	Shear stress and cumulative plastic intensity of plastic events for different quenching rates.	84
4.4	Numbers of plastic events as a function of the shear strain, for $Cu_{64}Zr_{36}$ MG, for different quenching rates (a) and comparison between quenching rates 10^{10} K/s and 10^{14} K/s after smoothing with SG filter method (b). . .	84
4.5	Plastic intensity of plastic events for the different quenching rates (a) and comparison between quenching rates 10^{10} K/s and 10^{14} K/s after smoothing with SG filter method (b).	85
4.6	Comparison of the average size of plastic events with strain for different quenching rates (a) and comparison between quenching rates 10^{10} K/s and 10^{14} K/s after smoothing with SG filter method (b).	85
4.7	Distribution of orientation of all the plastic events occurring during a shear test of $Cu_{64}Zr_{36}$ MG quenched at different quenching rates.	86
4.8	Comparing the distribution of orientation of plastic events for $Cu_{64}Zr_{36}$ MG with quenching rate 10^{10} K/s before and after the formation of SB. . .	87
4.9	Fitting stress-strain curves and curves after correction with factor α of $Cu_{64}Zr_{36}$ MGs with different quenching rates (10^{10} K/s (a), 10^{11} K/s (b), 10^{12} K/s (c), 10^{13} K/s (d), and 10^{14} K/s (e), respectively; left is the original curves and right is after correction by a factor $\alpha=1.01$ for 10^{10} K/s, $\alpha=1.03$ for 10^{11} K/s, $\alpha=1.03$ for 10^{12} K/s, $\alpha=1.09$ for 10^{13} K/s and $\alpha=1.1$ for 10^{14} K/s).	88
4.10	Cumulative number (a) and plastic intensity (b) of plastic events as a function of the shear strain for the three compositions.	90
4.11	Shear stress and cumulative plastic intensity as a function of the shear strain for the three compositions, $Cu_{64}Zr_{36}$ (a), $Cu_{50}Zr_{50}$ (b), and $Cu_{36}Zr_{64}$ (c).	91
4.12	Average size of plastic events as a function of the shear strain for the three compositions (a) and the curves after smoothed with SG filter method (b).	92

4.13	Number of plastic events as a function of the shear strain for the three compositions (original curves (a) and smoothed one with SG filter method (b)).	92
4.14	Plastic intensity of the plastic events with a function of the shear strain for the three compositions (original curves (a) and smoothed one with SG filter method (b)).	92
4.15	Distribution of the orientation of the plastic events of MGs with three different compositions.	93
4.16	The fitting stress-strain curves of three compositions after quenched with quenching rate 10^{11} K/s before correction ((a), (b) and (c)) and after correction ((d), (e) and (f)).	94
4.17	The schematic of plastic events during tensile deformation. Red ellipses represent the plastic events. Blue square represents the deformed MG system.	95
4.18	Tensile stress-strain curves of $Cu_{64}Zr_{36}$ MG with different quenching rates.	95
4.19	Young's modulus (a), yield stress (b) and yield strain (c) of $Cu_{64}Zr_{36}$ MG for different quenching rates deduced from the tensile stress-strain curve.	96
4.20	Cumulative number (a) and cumulative plastic intensity (b) of plastic events of $Cu_{64}Zr_{36}$ MG after tensile deformation with different quenching rates.	96
4.21	Number of plastic events as a function of the tensile strain for $Cu_{64}Zr_{36}$ MG quenched at different quenching rates (a) and smoothed curve for quenching rate 10^{10} K/s and 10^{14} K/s (b).	97
4.22	Plastic intensity of plastic events as a function of the tensile strain for $Cu_{64}Zr_{36}$ MG quenched at different quenching rates (a), smoothed curve for quenching rate 10^{10} K/s and 10^{14} K/s (b).	97
4.23	Average size of plastic events as a function of the tensile strain for $Cu_{64}Zr_{36}$ MG quenched at different quenching rates (a) and smoothed curves for 10^{10} K/s and 10^{14} K/s (b).	97
4.24	Map of the atomic shear strain for tensile strain 12.5 %, 15 % and 20 % for $Cu_{64}Zr_{36}$ MG quenched at different quenching rates.	98

LIST OF FIGURES

5.1	Temperature as a function of time over one cycle.	103
5.2	Potential energy (PE) as a function of the number of thermal cycles for $Cu_{64}Zr_{36}$ MGs with different quenching rates.	104
5.3	The variation of FI fraction as a function of the number of thermal cycling, for $Cu_{64}Zr_{36}$ MGs prepared with different quenching rates.	104
5.4	Map of the distribution of the non-affine square displacement ($D_{min}^2 > 100\text{\AA}^2$) at the 1st, 5th, 9th and 99th cycle, calculated with the previous cycle as reference, for $Cu_{64}Zr_{36}$ MGs prepared with different quenching rates.	105
5.5	Stress-strain curves of $Cu_{64}Zr_{36}$ MG quenched at different quenching rates (10^{10} K/s (a), 10^{11} K/s (b), 10^{12} K/s (c), 10^{13} K/s (d) and 10^{14} K/s (e), respectively) and submitted or not to 100 thermal cycles.	106
5.6	Shear modulus (a), yield stress and flow stress (b) of $Cu_{64}Zr_{36}$ MG quenched at different initial quenching rates with and without thermal cycling.	107
5.7	Comparison of atomic shear strain of $Cu_{64}Zr_{36}$ MG quenched at different initial quenching rates with and without thermal cycling, at strain 12.7 %.	107
5.8	Comparison of average size of plastic events of $Cu_{64}Zr_{36}$ MG (initial quenching rate 10^{10} K/s) without and with thermal cycling (a) and smoothed curves (b).	108
5.9	Comparison of average size of plastic events of $Cu_{64}Zr_{36}$ MG (initial quenching rate 10^{14} K/s) without and with thermal cycling (a) and smoothed curves (b).	108
5.10	Number of plastic events of $Cu_{64}Zr_{36}$ MG (initial quenching rate 10^{10} K/s) without and with thermal cycling (a) and smoothed curves (b).	109
5.11	Number of plastic events of $Cu_{64}Zr_{36}$ MG (initial quenching rate 10^{14} K/s) without and with thermal cycling (a) and smoothed curves (b).	109
5.12	Plastic intensity of plastic events of $Cu_{64}Zr_{36}$ MG (initial quenching rate 10^{10} K/s) without and with thermal cycling (a) and smoothed curves (b).	110
5.13	Plastic intensity of plastic events of $Cu_{64}Zr_{36}$ MG (initial quenching rate 10^{14} K/s) without and with thermal cycling (a) and smoothed curves (b).	110

5.14	Distribution of orientation of plastic events of $Cu_{64}Zr_{36}$ MG without and with thermal cycling for a quenching rate of 10^{10} K/s (a) and a quenching rate of 10^{14} K/s (b).	110
5.15	Variation of PE for the three compositions as a function of the number of thermal cycles.	112
5.16	Map of the distribution of the non-affine square displacement ($D_{min}^2 > 100\text{\AA}^2$) at the 1st, 5th, 9th and 99th cycle, which the previous cycle is the reference for the three studied compositions.	113
5.17	Stress-strain curves in quasi static shear for the three compositions previously submitted or not to the complete thermal cycling.	113
5.18	Shear modulus G (a), yield stress σ_y (b) and flow stress σ_f (c) deduced from Figure 5.17.	113
5.19	Map of the atomic shear strain in the three compositions previously submitted or not to thermal cycling, at 20 % shear strain.	114
5.20	Cumulative number of plastic events for each compositions submitted or not thermal cycling.	115
5.21	Cumulative plastic intensity for each composition submitted or not to thermal cycling.	115
5.22	Number of plastic events as a function of the shear strain, for each compositions submitted or not to thermal cycling (original curves (a)-(c) and smoothed curves (d)-(f)).	115
5.23	Plastic intensity of plastic events as a function of the shear strain for each composition before and after thermal cycling (original curves (a)-(c) and smoothed ones (d)-(f)).	116
5.24	Orientation distribution (gaussian fit) of the plastics events occurring over the whole shearing test for each composition before and after thermal cycling.	116
A.1	Average size of plastic events as a function of shear strain for the three compositions with a quenching rate of 10^{11} K/s (initial data).	127

LIST OF FIGURES

A.2	Different points window of SG filter method when smoothing the curve of average size of plastic events with shear strain of $Cu_{64}Zr_{36}$ MG with a quenching rate of 10^{11} K/s.	128
A.3	Curves in Figure A.1 after smoothing with 50 points of window.	128

List of Tables

3.1	T_g for $Cu_{64}Zr_{36}$ MGs with different quenching rates.	59
3.2	Relative decrease of FI after a quasi-static shear deformation (up to flow) for the three compositions.	72
4.1	Sigma value of the distribution of orientation of shear transformation with different quenching rates.	87
4.2	Sigma values of the distribution of the orientation of the plastic events for the three compositions.	93
5.1	Yield and flow stress, in quasi static shear test at 0.1 K, for the three compositions submitted or not to thermal cycling.	112
5.2	Relative decrease in shear modulus, yield stress and in the difference between yield and flow stress for the three compositions after thermal cycling.	114
5.3	Width of the orientation distribution of the plastic events and relative variation deduced from Figure 5.24.	116

Abstract

Metallic glasses (MGs) are very promising new materials because of their excellent mechanical properties. They have many potential applications in micromechanics, microelectronics, jewelry, biomedical, aerospace and many other fields. However, their low plasticity at room temperature limits their wide diffusion in the industry for the moment. Therefore, the improvement of their ductility has become a major issue in materials science. The objective of this thesis is to study the plasticity of metallic glasses prepared under different conditions, by molecular dynamics (MD) simulations and to characterize the plastic events occurring at the microscopic scale during their deformation in order to understand how the plasticity evolves, and finally to evaluate under which conditions the ductility can be improved. The system studied in this thesis is a binary Cu-Zr model. We studied the effect of quenching rate, composition, strain rate and temperature. Our simulations show that during quasi-static shear deformation, the plasticity of Cu-Zr glasses is more homogeneous, i.e., the localization of deformation and the formation of shear bands are more limited, when these materials are prepared with higher quenching rates, when they contain less copper, and/or when they are subjected to higher deformation rates and/or temperatures. In order to understand the microscopic mechanisms involved in this plasticity, we have developed a method to identify and characterize individual plastic events. In this way, we can evaluate their number, plastic intensity, average size and orientation. Moreover, we are able to reconstruct the simulated mechanical behavior by considering the plastic events as Eshelby inclusions in an infinite elastic matrix. Finally, we show that thermal cycling below the glass transition temperature can be, under certain conditions, an efficient way to improve the ductility of metallic glasses, via their rejuvenation.

Résumé

Les verres métalliques (MGs) sont de nouveaux matériaux très prometteurs du fait de leurs excellentes propriétés mécaniques. Ils ont potentiellement de nombreuses applications en micromécanique, microélectronique, bijouterie, dans le domaine biomédical, l'aérospatial et bien d'autres domaines. Cependant, leur faible plasticité à température ambiante limite pour l'instant leur large diffusion dans l'industrie. Par conséquent, l'amélioration de leur ductilité est devenue un enjeu majeur pour la science des matériaux. L'objectif de cette thèse est ainsi d'étudier la plasticité de verres métalliques préparés sous différentes conditions, par des simulations de dynamique moléculaire (MD) et de caractériser les événements plastiques survenant à l'échelle microscopique pendant leur déformation afin de comprendre comment la plasticité évolue, et finalement d'évaluer sous quelles conditions la ductilité peut être améliorée. Le système étudié dans cette thèse est un modèle binaire Cu-Zr. Nous avons étudié l'effet de la vitesse de trempe, de la composition, de la vitesse de déformation et de la température. Nos simulations montrent que lors de déformations en cisaillement quasi-statique, la plasticité des verres Cu-Zr est plus homogène, c'est-à-dire que la localisation des déformations et la formation des bandes de cisaillement sont plus limitées, lorsque ces matériaux sont préparés avec des vitesses de trempe plus élevées, lorsqu'ils contiennent moins de cuivre, et/ou lorsqu'ils sont soumis à des vitesses de déformation et/ou des températures plus élevées. Afin de comprendre les mécanismes microscopiques impliqués dans cette plasticité, nous avons développé une méthode pour identifier et caractériser les événements plastiques individuels. De cette façon, nous pouvons évaluer leur nombre, leur intensité plastique, leur taille moyenne et leur orientation. De plus, nous sommes capables de reconstruire le comportement mécanique simulé en considérant les événements plastiques comme

des inclusions d'Eshelby dans une matrice élastique infinie. Enfin, nous montrons que le cyclage thermique sous la température de transition vitreuse peut être, dans certaines conditions, un moyen efficace d'améliorer la ductilité des verres métalliques, via leur rajeunissement.

General Introduction

Metallic glasses (MGs) can be obtained when a liquid metal is cooled at a rapid quenching rate without crystallizing. The atomic structure of MG exhibits short-range order (SRO) or medium-range order (MRO), but does not have a long-range order, like crystalline alloys. Therefore, their physical properties are isotropic. Moreover, due to the absence of defects, such as grain boundaries and dislocations in crystals, MGs have high tensile strength, hardness, high elastic limit and can find applications in various fields. For example, in the field of electronics, due to their superior soft magnetic properties, they can be used in transformers, inductors, and sensors. In the medical field, due to their biocompatibility, MGs can be used to make medical and surgical devices and biological implant materials. In the aerospace field, their high elastic limit can meet the performance requirements of spacecraft. In the military industry, their high strength can be used to make armor-piercing bullets. However, MGs have a low plasticity at room temperature, which dramatically limits their engineering applications. In order to improve this plasticity, many studies have been performed. Nevertheless, a thorough understanding of the origin of plasticity of MGs at the microscopic scale is still lacking.

Thus, the motivation of this thesis is to explore the parameters that promote the plastic deformation of MGs and to study the effect of these parameters on the plasticity at the microscopic scale. The system investigated in this work is a model Cu-Zr binary MG, and the method used is Molecular Dynamics (MD) simulations. Cu-Zr binary MGs have a simple chemical composition and excellent glass-forming ability (GFA). They have been the topic of many experiments and numerical simulations. MD simulations provide a method to study the thermodynamic, structural, and mechanical properties at the atomic scale. The parameters that will be studied are quenching rate, composition, strain rate,

and temperature. The originality of this thesis consists in characterizing and quantifying the plastic events occurring during deformation, in terms of their number, size, and plastic intensity, thus providing a better understanding of the microscopic plasticity of MGs. The method we have used to identify these plastic events is based on the definition of continuous plastic energy field from which we can extract the positions of the centers of the plastic events and determine their size and plastic intensity. This technique is quite unique with respect to the way plasticity of MGs is studied in the literature, since it is a rare example allowing to address in a proper and systematic fashion the identification and the characterization of the shear transformations (STs), which are considered as the elementary plastic rearrangements in amorphous materials.

The manuscript is organized in five chapters.

Chapter 1 introduces the research background, including the MG material studied, structural characteristics, mechanical properties, and applications of MGs. In addition, the microstructural models and the deformation characteristics of MGs are reported from the literature. The explanations of shear band formation from STs are also presented. We then describe the Eshelby's inclusion model, which will be used in Chapter 4 to reconstruct the stress-strain curves from MD simulations. MD simulations of MGs are then introduced and their results regarding the obtained structure, the correlation between microstructure and plasticity, and the effects of quenching rate, temperature, and composition on the microstructure and the mechanical properties. Previous studies about strategies developed to improve the plasticity of MGs are also discussed. Finally, questions which need to be addressed in this thesis are listed.

Chapter 2 presents the research methods used in this thesis, e.g., MD simulations, and the construction of the Cu-Zr binary MG model. The parameters that we need to calculate in Chapters 3, 4, and 5, such as radial distribution functions (RDF), $\langle 0,0,12,0 \rangle$ icosahedral fraction (full-icosahedra, FI), and local atomic shear strain, are described. The definition and characterization of the plastic events, including the calculation of their size, number, and plastic intensity, as well as the reconstruction of stress-strain curves from MD simulations by fitting atomic displacements based on Eshelby's inclusion model, are then detailed.

Chapter 3 focuses on the general analysis of the mechanical properties of MGs through

MD simulations. The effects of quenching rate, compositions, strain rate, and temperature on the microstructure and the mechanical properties of MGs are studied and discussed. At the microscopic scale, their effect on the microstructure of Cu-Zr binary MGs, with respect to SRO and atomic arrangement, is also investigated through the calculation of the radial and partial radial distribution functions and of the fraction of FI. Moreover, maps of local STs are plotted. Concerning the mechanical properties, elastic modulus, yield stress, and stress drop of MGs are then compared and discuss with regards to the previous data.

Chapter 4 then focuses on the origin of the macroscopic plasticity of MGs through the analysis of plastic events at the microscopic scale. In this chapter, the effect of parameters studied in Chapter 3, i.e., quenching rate and composition, on the plastic events, with respect to their average size, number, plastic intensity, and distribution of orientation is analysed. The stress-strain curves from MD simulations are also reconstructed using Es-helby's inclusion model.

The last Chapter 5 is devoted to the impact of thermal cycling of the materials, with the aim to tune the plastic behavior of the MG. The variation of the potential energy and nonaffine square displacement induced by these thermal cycling are investigated for MGs prepared with different quenching rates and compositions. The effect of thermal cycling on the mechanical properties as well as on the plastic events occurring during quasi-static shear deformation are also investigated.

The manuscript ends with a conclusion on the main results and on the research perspectives opened by this work.

Chapter 1

Introduction

Contents

1.1	General features of metallic glasses	10
1.2	Mechanical properties of metallic glasses	11
1.3	Application of metallic glasses	12
1.4	Atomic-level structure of metallic glasses	14
1.5	Atomic-scale deformation of metallic glasses	17
1.5.1	Free volume model	17
1.5.2	Atomic local shear transformation	19
1.5.3	Formation of shear bands	19
1.6	Eshelby's inclusions	23
1.7	Molecular Dynamics studies on metallic glasses	27
1.7.1	Studies about structure	27
1.7.2	Correlation between microstructure and plastic behavior	28
1.7.3	Effect on microstructure and mechanical properties	30
1.8	Improvement of plasticity	32
1.8.1	Composite metallic glasses	33
1.8.2	Pre-deformation	34
1.8.3	Thermal pre-treatment	34
1.9	Open questions	36

1.1 General features of metallic glasses

Metallic glass (MG) is an amorphous alloy produced by cooling it from its liquid state with a rapid cooling rate [Greer, 1995]. As shown in Figure 1.1, when temperature decreases with an infinitely low cooling rate, the liquid crystallizes at the melting temperature (T_m). In contrast, with an extremely high cooling rate, larger than a critical value, it overcomes T_m and keeps its liquid state, called supercooled liquid. When temperature further decreases, viscosity increases, and the liquid freezes and forms the glass at a temperature called glass transition temperature (T_g) [Ediger et al., 1996]. T_g is defined as the temperature where the viscosity takes the value of 10^{12} Pa·s [Debenedetti and Stillinger, 2001, Spaepen and Turnbull, 1984]. Unlike the liquid to crystal transition, a first-order phase transition, the glass transition is not a phase transition but a kinetic phenomenon because T_g depends on the cooling rate. As shown in Figure 1.1, a glass obtained with a higher cooling rate has a higher T_g . The cooling rate is a significant parameter for the formation of glasses. By cooling at high cooling rates, there is no chance for the atoms of MGs to form periodical lattices like crystalline alloy, as shown in Figure 1.2. Compared to crystalline alloy, the arrangement of atoms in MG is disordered at a long distance,

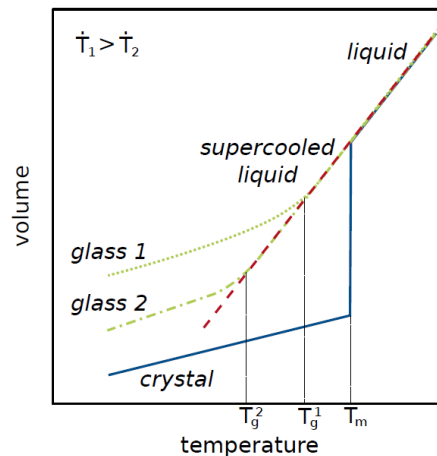


Figure 1.1: Volume change as a function of temperature from liquid to solid state (the dashed red line represents the equilibrium liquid) [Ritter, 2012]

whereas ordered at a short and intermediate distance, giving rise to respectively short-range order (SRO) and medium-range order (MRO). Variation of cooling rates leads to

different initial “frozen” microstructures of MGs and thus plays a vital role in the resulting mechanical properties of them [Fu et al., 2013, Li et al., 2012, Yue et al., 2018], as we will see in this thesis.

Moreover, the large size differences between constituent atoms are beneficial to forming denser atomic packing and hinder atomic diffusion, therefore forming more stable glasses after cooling [Inoue, 2000, Telford, 2004, Wang et al., 2004].

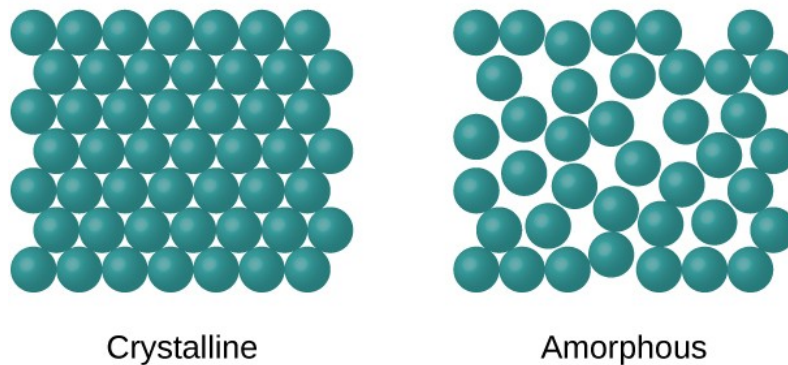


Figure 1.2: *Microscope diagram of the atomic arrangement of crystalline and amorphous alloy.*

1.2 Mechanical properties of metallic glasses

Compared to crystalline counterparts, MGs present excellent mechanical properties, such as higher strength and hardness, higher elastic limit, superior corrosion resistance, etc [Inoue, 2000, Johnson, 1999, Trexler and Thadhani, 2010]. As shown in Figure 1.3, with respect to traditional materials, like crystalline steels, titanium alloys, wood etc., the strength of Mg-based and Ti-based MGs can reach twice and four times that of crystalline alloys [Inoue, 2000]. The elastic limit can be over 2 %, while for crystals, they are lower than 1 %. The fracture strength (tensile yield strength) of MGs is higher than 1 GPa, and elastic energy storage is eight times that of crystalline materials [Telford, 2004]. The hardness of Fe-B based MGs can reach 1250 HV, which is much higher than magnesium and titanium crystalline alloy [Inoue and Shen, 2006].

Even though MGs own so many outstanding mechanical properties, they have some drawbacks, particularly low ductility at room temperature. When they reach their yield point under loading, shear bands form and the MG will crack in a narrow zone (10-20

nm width). Once the crack appears, it will expand rapidly along the stress direction, resulting in a brittle fracture. As shown in Figure 1.4, there is nearly no plastic deformation for Zr-based MG [Inoue and Shen, 2006].

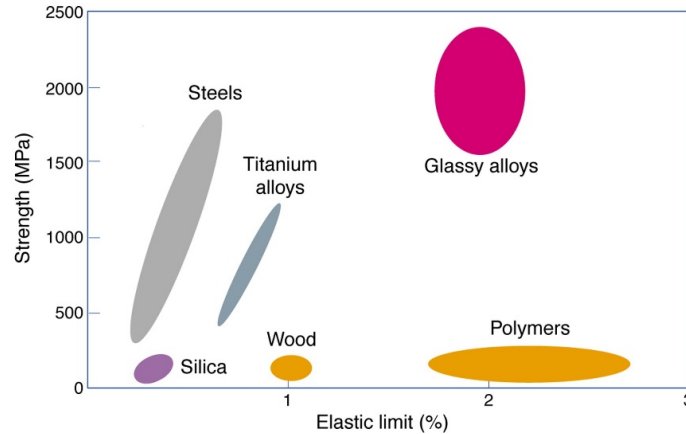


Figure 1.3: Ashby plot of the strength vs. the elastic limit of different classes of materials: amorphous metallic alloys combine the higher strength of crystalline metal alloys with the elasticity of polymers [Telford, 2004].

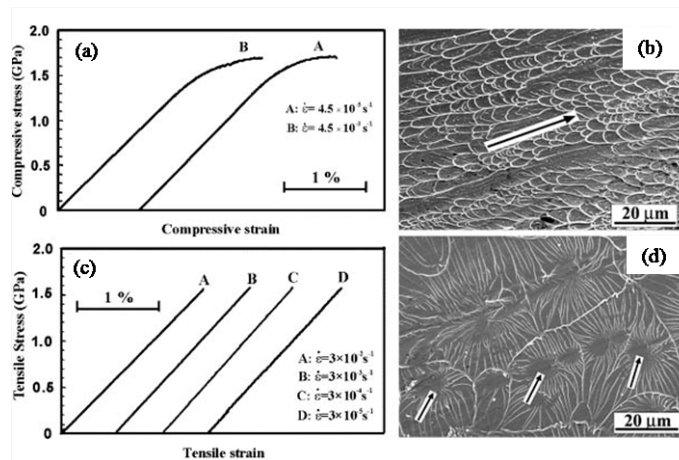


Figure 1.4: Deformation of Zr-based MG in experiment [Zhang et al., 2003]. (a) Compressive strain-stress curve (b) Compression fracture morphology characteristics (c) Tensile strain-stress curve (d) Tensile fracture morphology characteristics

1.3 Application of metallic glasses

The high elastic limit makes MGs a material with excellent elastic storage properties, which can be applied to sports equipment. For example, Zr-based MGs are used as golf

club heads by Liquid metals company. They can transfer 99 % of energy to the ball. Thus, their hitting distance is significantly higher than clubs made of other materials. The MGs with high elasticity can also be used to fabricate armor interlays, which can extend the action time between bullets and armor, slowing impact and damage. The most widespread application of MGs stems from their magnetism. Bulk MGs can be directly cast or processed into miniature iron cores and then made into electrical transformers or sensors used in various electronic or communication equipment. Due to their high strength, corrosion, and wear resistance, MGs are made into miniature medical equipment parts. The biocompatibility, degradability, and non-allergic properties of MGs make them medically useful for manufacturing surgical devices, e.g., surgical scalpels, artificial bones, and biosensing materials. Although there are still bottlenecks in the large-scale industrial application of MGs, the research on them has made significant progress. Thus, the application prospects of MGs are vast.

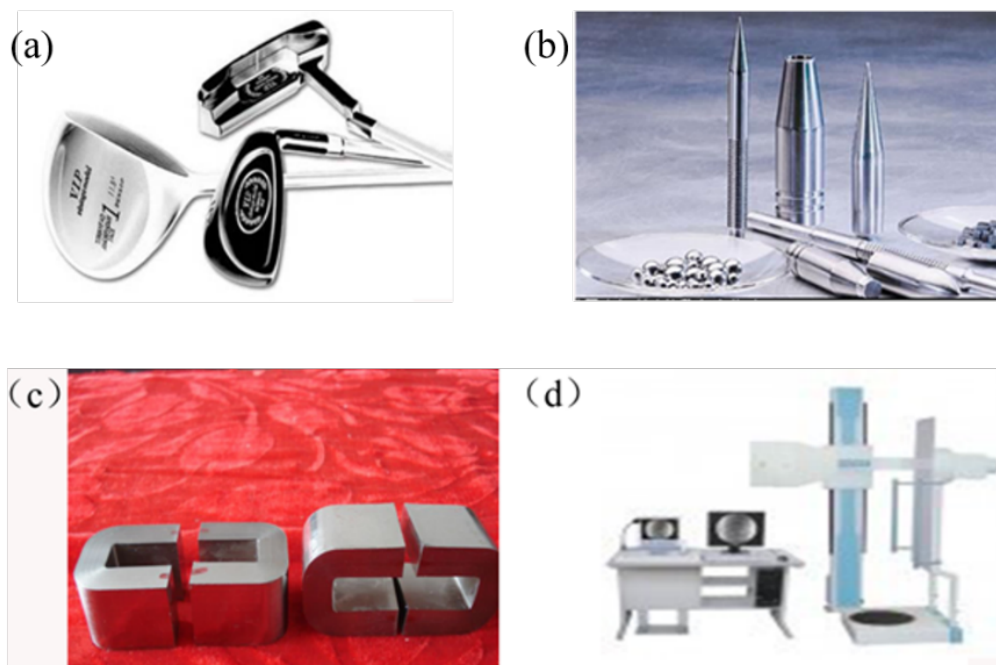


Figure 1.5: *Application of MG. (a) Golf stick (b) Armor-piercing projectile (c) Amorphous transformer core (d) Amorphous gastroscope*

1.4 Atomic-level structure of metallic glasses

Through the observation of Radial Distribution Function (RDF) in experiments, local atomic arrangements present some degree of short-range order (SRO) topologically and chemically [Lamparter et al., 1982]. RDF is shown in Figure 1.6, and it is proportional to the probability of finding an atom at a certain distance of a given central atom.

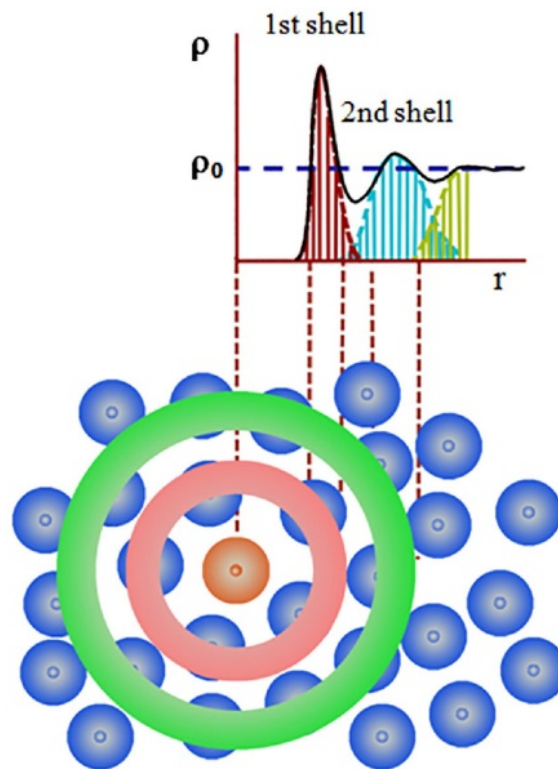


Figure 1.6: *The illustration of radial distribution function [Weihua, 2013].*

Many models of atomic arrangement in MGs have been proposed to facilitate the microstructural study of MGs. Bernal's dense random packing of hard spheres is one of them, which considers atoms as hard spheres, forming network structures randomly without cavities [Bernal, 1960a, Bernal, 1960b]. Cargill simulated Ni-P MG with this model and obtained the RDF in agreement with experimental results [Cargill III, 1975]. After that, many other structural models have been developed. Gaskell proposed the local coordination model, which assumes that local structure in MGs is similar to that in crystals with the same composition, i.e., the local structures both consist of polyhe-

dra with various shapes [Gaskell, 1978]). For metal-metalloid glasses, constituted by transition metals and non-metallic elements [Gaskell, 1978], the RDF calculated by this model corresponds to the result by neutron diffraction. According to Gaskell's local coordination model, metal-metalloid MGs have capped trigonal prism structural units with metalloid atoms as the cores and metal atoms distributed on six corners [Gaskell, 1979a, Gaskell, 1979b]. Some structures of MGs can be explained by Gaskell's model, like Pd-Si [Fukunaga and Suzuki, 1980], $Ni_{82}B_{18}$ [Chadha et al., 1981], Fe-P, etc. However, for metal-metal glasses, this model cannot be applied [Chen, 2008]. Free volume model [Spaepen, 1977] is an alternative model, first issued by Cohen and Turnbull and then improved by Cohen and Spaepen, widely applied to the study of the structure and properties of MGs [Cohen and Turnbull, 1959]. Free volume is thought to provide the physical space for the free motion of a single atom or atomic cluster without external energy. The free volume reduces when cooling the liquid until the system gets frozen with no free volume, thus forming the glass structure. However, the free volume model cannot describe the atomic structure associated with SRO. Therefore, to better understand the SRO of MGs, another model called polytetrahedral packing model was introduced. In this model, we identify basic structural units in the MG, called Voronoi polyhedral [Nelson and Spaepen, 1989], defined as the smallest closed convex polyhedra made up of perpendicular bisector line connecting a central atom with neighbor atoms [Finney, 1970]. Voronoi polyhedra are identified by Voronoi indexes $\langle n_3, n_4, n_5, n_6, \dots \rangle$, where n_i indicates the number of surface with i edges. For example, n_3 means the number of triangles. As shown in Figure 1.7, the $\langle 0,0,12,0 \rangle$ icosahedron, if the polyhedron is unfolded, we can get zero triangles, zero quadrangles, twelve pentangles, zero hexagons, and zero polygons with more than six edges. $\langle 0,0,12,0 \rangle$ icosahedron is also called full-icosahedron(FI). There are various types of polyhedra in MGs, as shown in Figure 1.8.

With the study of supercooled liquid, Frank supposed that central atoms and their nearest neighbors form icosahedra structure [Frank, 1952]. These icosahedra structures present characteristic five-fold symmetry and are abundant in MGs, due to their dense packing and the fact that they are energetically more favorable [Lee et al., 2007, Cheng et al., 2008b, Cheng et al., 2008a, Cheng et al., 2009a, Ding et al., 2014a], and are evidenced by both simulations [Cheng et al., 2009b, Cao et al., 2009, Cheng et al., 2008b] and experi-

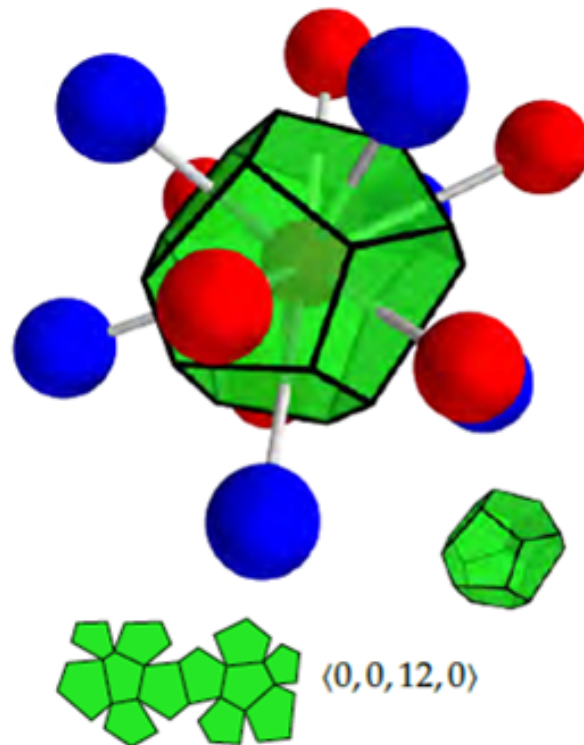


Figure 1.7: $\langle 0,0,12,0 \rangle$ icosahedron in $\text{Cu}_{64}\text{Zr}_{36}$ metallic glass.

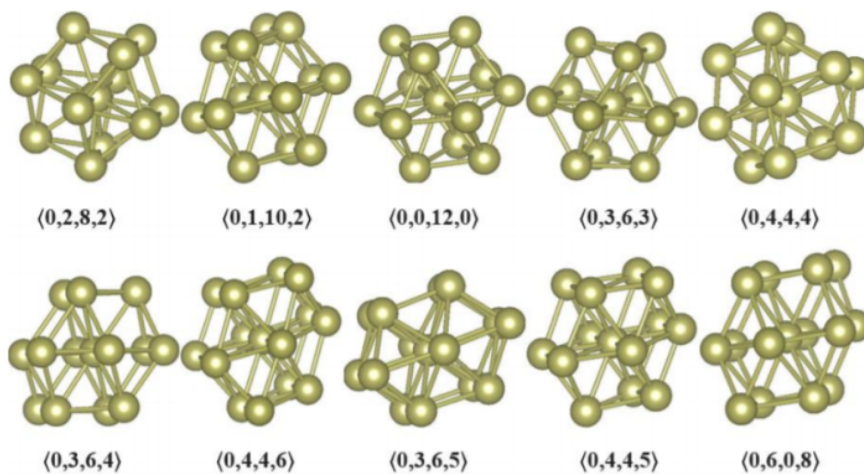


Figure 1.8: Representative atomic clusters for monatomic hafnium [Şengül and Çeltik, 2018].

ments [Luo et al., 2004, Li et al., 2009].

Moreover, SRO clusters can be connect to each other to form larger structures. Miracle proposed connection rules of SRO clusters to form MRO [Miracle, 2006]. These SRO icosahedra structures as central clusters extend spatially in hexagonal close packing (hcp) or face-centered cubic (fcc) configurations forming MRO structures with vertex-sharing (VS), edge-sharing (ES), face-sharing (FS), and intercross-shared (IS) connections, as shown in Figure 1.9 (SRO clusters are shown by dashed red circles in the figure). SRO clusters are remarked with dashed red circles. The connections between SRO clusters allow to form chains, loops, or even networks [Sheng et al., 2006].

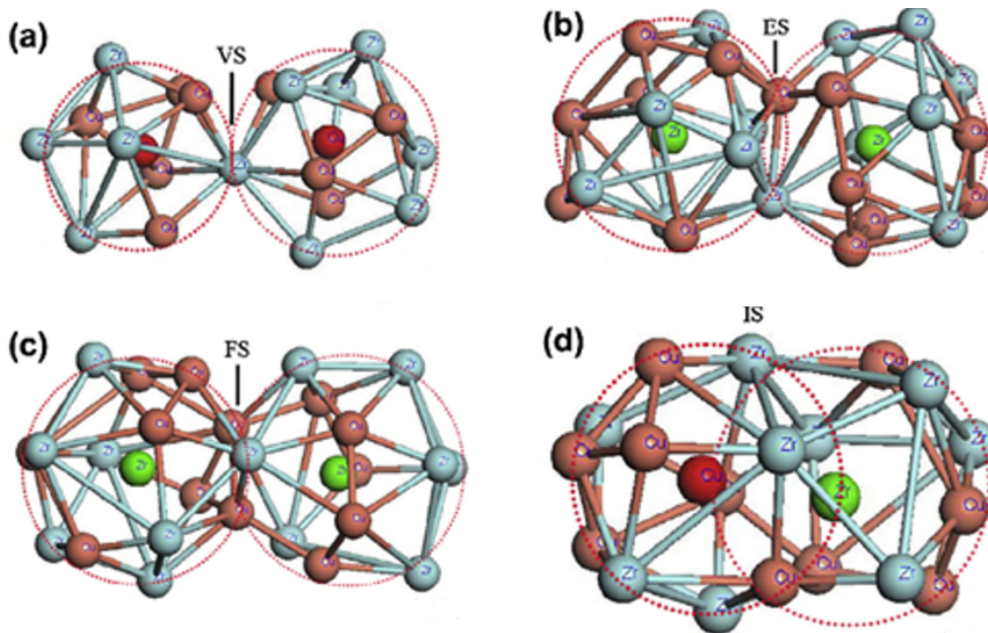


Figure 1.9: SRO clusters connected by (a) VS, (b) ES, (c) FS, and (d) IS in the $\text{Cu}_{50}\text{Zr}_{50}$ metallic glass (Zr and Cu atoms are represented with blue and brown balls, respectively, and centered Zr and Cu atoms are represented using green and red balls, respectively) [Li et al., 2014].

1.5 Atomic-scale deformation of metallic glasses

1.5.1 Free volume model

For traditional crystals, deformation is always accompanied by the proliferation and propagation of dislocations. Thus, the plastic deformation mechanism of the crystal can

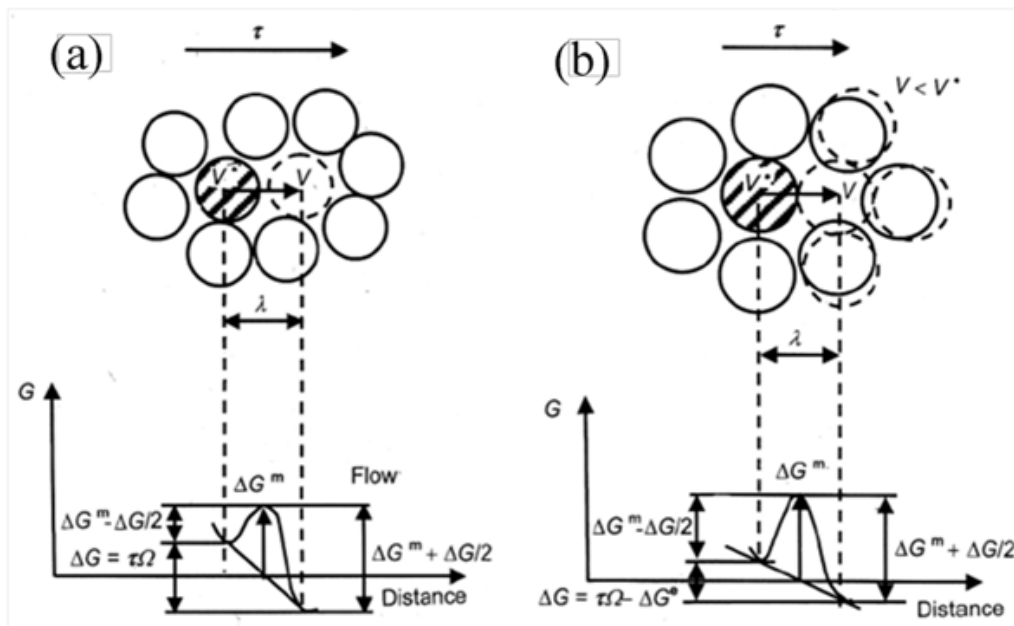


Figure 1.10: Free volume model in the flow of metallic glass [Spaepen, 1977]. (a) Single atomic transition (b) Free volume generation

be explained by the dislocation theory. When the external load exceeds the elastic limit of the crystal, plastic deformation occurs. For MGs, due to the different atomic arrangements, there exists no lattice, so the dislocation mechanism cannot explain the plastic deformation of MGs.

To study the atomic-scale deformation of MGs, people proposed many models. The most mature and widely used one is the free volume model, already introduced in Section 1.4 to describe the atomic-level structure. It considers vacancies randomly distributed as defects [Spaepen, 1977]. The deformation of MGs is based on the "transition" of a single atom. As shown in Figure 1.10, if an atom has a large enough vacancy in its vicinity (approximately equal to the volume of a hard atomic sphere), and the activation energy of the atom is larger than transition energy, the atom will be squeezed into an adjacent vacancy, and free volume redistributes. The free volume model explains the shear localization of MGs at the atomic scale, but it cannot explain the atomic processes in the shear bands (SBs). To describe the deformation mechanism of MGs, the motion of atomic clusters, and not just a single atom, should be considered, as explained in the following subsection.

1.5.2 Atomic local shear transformation

Argon proposed to extend the theory of Spaepen by considering the transition of atomic clusters when deformation occurs [Velasco et al., 2017]. He introduced the concept of shear transformation (ST) as the deformation unit, which is a thermally activated local rearrangement of several up to a few hundred atoms under shear stress [Argon, 1979] around free volume abundant sites.

In 1988, Falk and Langer proposed the shear transformation zone (STZ) model of plasticity of MGs by extending the theory of Argon and Spaepen on the basis of Molecular Dynamics (MD) simulation of viscoplasticity of MGs [Falk and Langer, 1998]. How does individual STZ develop to macroscopic flow? Johnson and Samwer issued the cooperative shear model (CSM) for the plastic flow of MGs [Johnson and Samwer, 2005]. They proposed that STZ and macroscopic flow are related respectively to β relaxation and α relaxation, as shown in Figure 1.11 [Harmon et al., 2007]. Yielding occurs when a critical fraction of STZs leads to global instability.

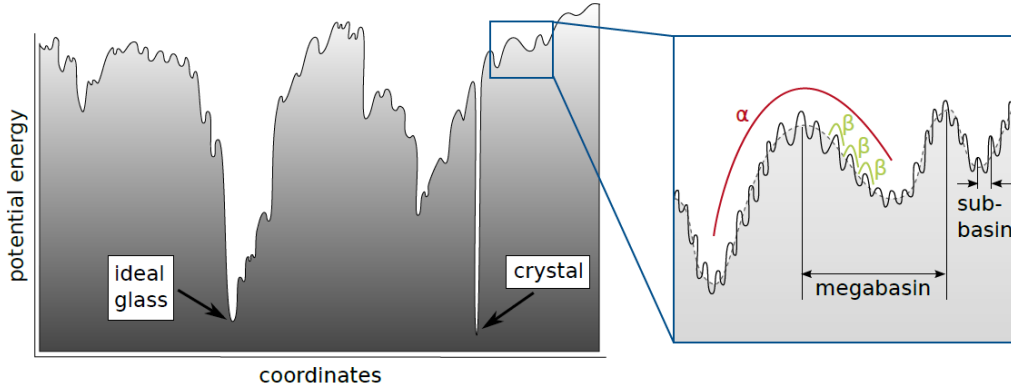


Figure 1.11: *The schematic of the relationship between α relaxation and β relaxation on potential energy landscape (PEL) [Ritter, 2012].*

1.5.3 Formation of shear bands

The plastic deformation of MGs is very heterogeneous at room temperature, and it is likely to form localized shear bands (SBs) in extremely narrow region [Bian et al., 2001, Chen et al., 2011, Jiang et al., 2008, Jiang and Dai, 2011, Pampillo, 1975, Zhang et al., 2003]. In the free volume theory, the transition of atoms or atomic clusters easily occurs where

free volume is large and bond energy is small. The plastic deformation of MGs can be divided into two steps: before the generation of SB, in the region where free volume is abundant, heterogeneous localized plastic deformation occurs; after the generation of SB, the expansion of SBs results in extended plastic deformation, accompanied by strain softening. If there are multiple SBs in various directions, a single SB will be hindered, yielding homogeneous deformation and better plasticity. Therefore, the research about the formation of SBs is essential for understanding the molecular mechanisms of plastic deformation and for improving the plasticity of MGs [Chen et al., 2020, Liu et al., 2009, Sergueeva et al., 2005].

The formation of SBs is a multiscale behavior at the microscopic, mesoscopic, and macroscopic scales. Atomic rearrangements lead to plastic events, which are STZs, containing several tens of atoms. Percolation of STZs can facilitate the formation of SBs on the order of a tenth of a micrometer [Schuh et al., 2007]. At a macroscopic scale, a single SB expands, or several SBs interact, which results in different plastic behaviors [Su and Anand, 2006]. Greer et al. proposed three possible explanations for the formation of SBs [Greer et al., 2013]. In the first one, the formation of the SB is considered to be the percolation of homogeneously activated STZs. After the activation of STZs, there will be a large accumulation of them. When it exceeds the percolation limit, a band with concentrated shear strains will form along the path with maximum shear stress on the plane. The second one considers that an embryonic SB generates due to activating local STZs, and then it grows to a mature SB. With the help of computer simulation and a theoretical model, Shimizu et al. [Shimizu et al., 2006] found that when the size of embryonic SB reaches around 100 nm, mature SB will form. In the second explanation, the SB is nucleated from local STZ resulting from local stress concentration. In this case, there is a temperature gradient along with SB. The SB can be divided in four zones from the front to the tail, as shown in Figure 1.12: aged glass, rejuvenated glass, glue, and liquid (ARGL), in agreement with the experimental results of Yang et al. [Yang et al., 2005, Yang et al., 2006a]. Therefore, the propagation of SB is heterogenous in this case. The third explanation involves two consecutive stages. The first stage is stress concentration (Figure 1.13 (a)), similar to the second explanation. The activation of STZs increases the structural disorder and results in structural rejuvenation. After that, the structural rejuvenation propagates heteroge-

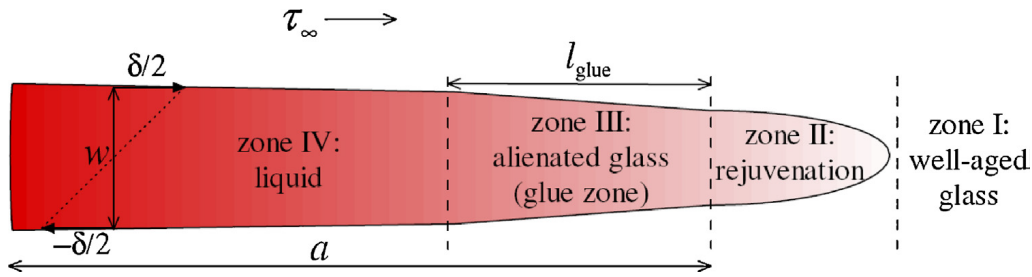


Figure 1.12: The schematic diagram of the temperature gradient of SB [Shimizu et al., 2006].

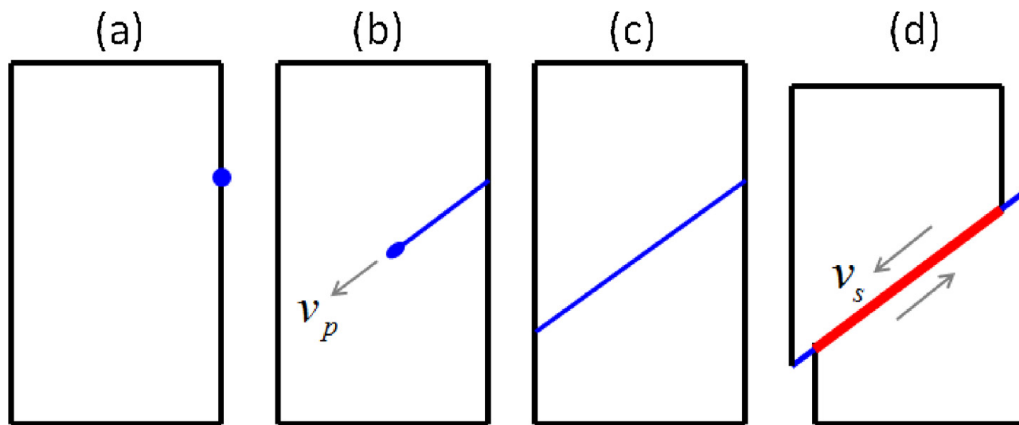


Figure 1.13: Diagram of formation of SB in the MG under compression loading (v_p is propagation velocity of structural disorder and v_s is shear velocity) [Greer et al., 2013].

neously across the material (Figures 1.13 (b) and (c)). The second stage is the sliding and shear offset along the rejuvenation plane simultaneously, accompanied by local heating, which promotes the expansion of SB (Figure 1.13 (d)). This third explanation was verified by computer simulation of Cao et al. [Cao et al., 2009], in which rejuvenation propagates with a disordered structure. In conclusion, the origin of the SB is attributed to the activation of STZs.

Generally, it is thought that the reason for forming localized SBs is the reduction of viscosity in some inhomogeneous regions in MGs. There are two factors for the reduction of viscosity: free volume softening [Huang et al., 2002, Spaepen, 1977, Steif et al., 1982] and adiabatic softening [Leamy et al., 1972, Liu et al., 1998]. In free volume softening the aggregation of localized free volume causes the localized SB of MGs without thermal effect, which has been proved by Li and Gu [Gu et al., 2002, Li et al., 2002a]. As shown in Figure 1.14, dense free volume appears (nanoscale voids in high-resolution TEM image) around SB. On the other hand, in adiabatic softening the transformation of

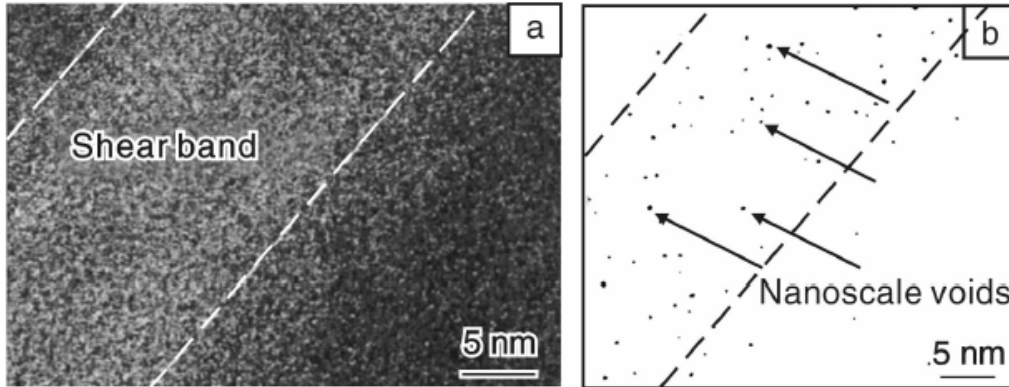


Figure 1.14: Shear band of Zr-based metallic glass (a) High-resolution TEM image and (b) nanoscale voids within it [Li et al., 2002a].

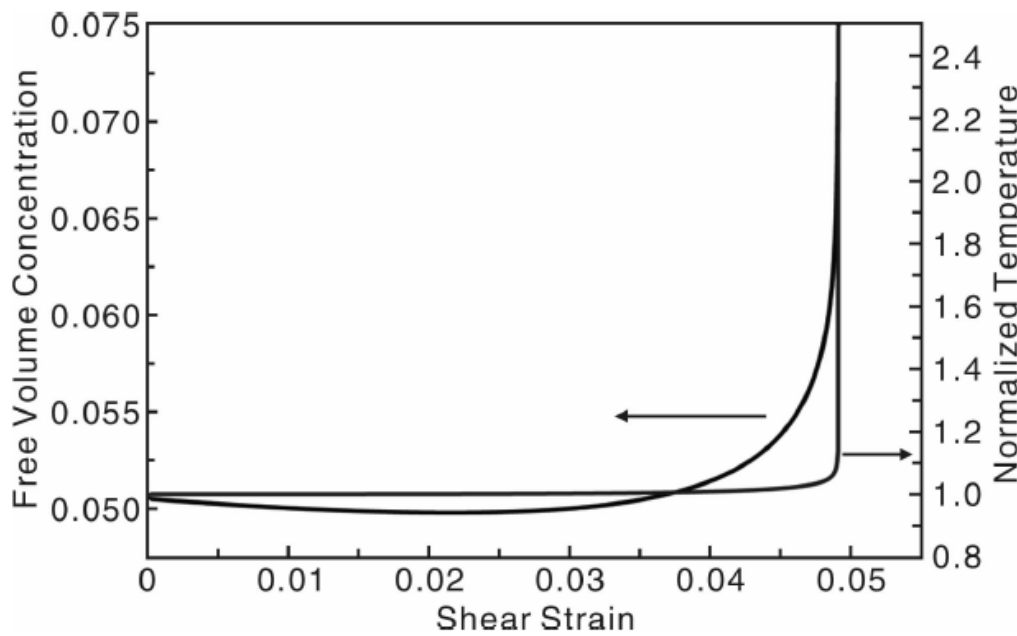


Figure 1.15: Evolution of free volume and temperature during the shear localization process.

deformation energy into heat can lead to the rise in adiabatic temperature. When the adiabatic temperature exceeds the glass transition temperature or even the melting point, thermal expansion and softening will occur, resulting in the reduction of viscosity [YL et al., 1992]. Based on free volume theory, Dai et al. revealed that shear band instability in MGs is the result of the synergistic effect of free volume and adiabatic softening [Dai et al., 2005]. Among them, free volume plays the main controlling role, and heat plays the auxiliary role. Compared with the increase of adiabatic temperature, the free volume appears earlier and much faster [Jiang and Dai, 2009], as shown in Figure 1.15.

1.6 Eshelby's inclusions

Several assumptions to analyze the plastic deformation of MGs have been introduced previously in this chapter. One can make an analogy between local shear transformations (STs) and inclusions in an infinite elastic matrix based on the theory of Eshelby's [Eshelby, 1957, Picard et al., 2004, Rodney et al., 2011]. An Eshelby's inclusion can be described with the following three imaginary steps [Eshelby, 1957].

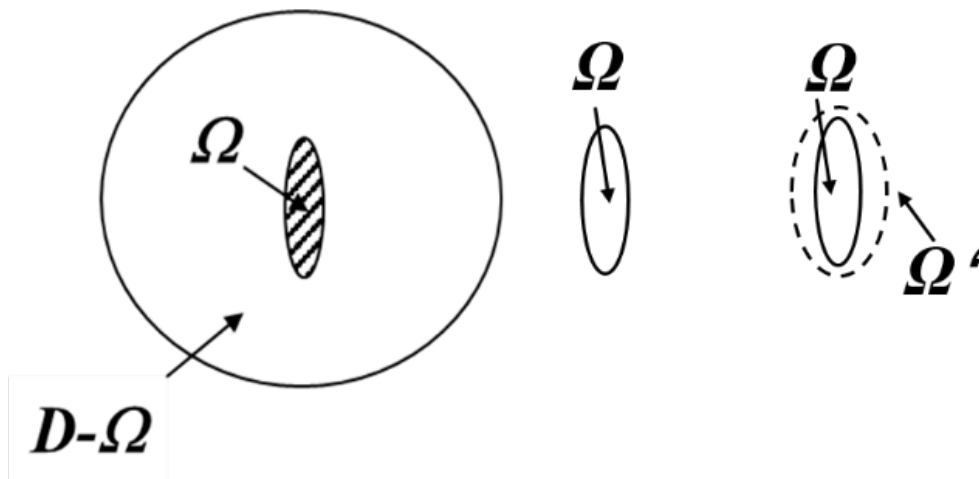


Figure 1.16: Scheme of inclusion's removal from the matrix and of its unconstrained transformation.

Step 1. In an infinite isotropic homogeneous elastic medium (D), we remove an inclusion (Ω) with the surface area S_0 from it and make it unconstrained with stress-free transformation strain tensor ϵ_{ij}^T , as shown in Figure 1.16 ($\Omega \rightarrow \Omega'$). ϵ_{ij}^T is called eigenstrain, i.e., the

strain without undergoing stress. The elastic constant of inclusion Ω , C_{ijkl} is identical to that of the matrix D . Thus, eigenstress σ_{ij}^T can be expressed as, $\sigma_{ij}^T = C_{ijkl} e_{kl}^T$. The strain e_{ij} , stress σ_{ij} , and displacement u_i of the inclusion after removing from the matrix are calculated as:

$$e_{ij} = e_{ij}^T \quad (1.1)$$

$$\sigma_{ij} = 0 \quad (1.2)$$

$$u_i = e_{ij}^T x_j \quad (1.3)$$

where x_j is the component of unit displacement vector in j direction.

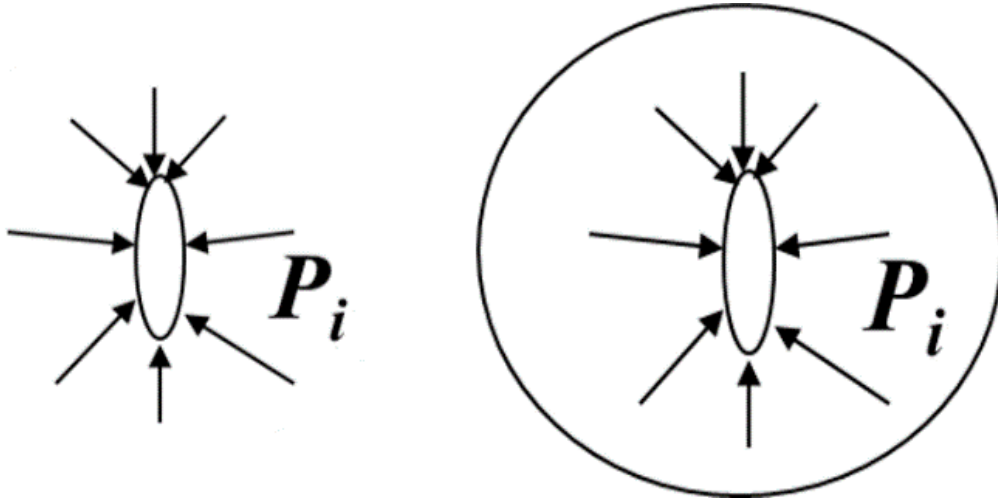


Figure 1.17: Applying force on the inclusion and putting it back in the matrix.

Step 2. We apply a surface traction (P_i) on the inclusion to restore its original form and put it back in the hole in the matrix, as shown in Figure 1.17. The elastic strain should offset the eigenstrain, i.e., $e_{ij}^{el} = -e_{ij}^T$. Surface traction P_i is related to the stress, $P_i = -\sigma_{ij}^T n_j$. n_j is the component form of normal vector. The strain, stress, and displacement of the inclusion are:

$$e_{ij} = e_{ij}^{el} + e_{ij}^T = 0 \quad (1.4)$$

$$\sigma_{ij} = C_{ijkl}e_{kl}^{el} = -C_{ijkl}e_{kl}^T = -\sigma_{ij}^T \quad (1.5)$$

$$u_i = 0 \quad (1.6)$$

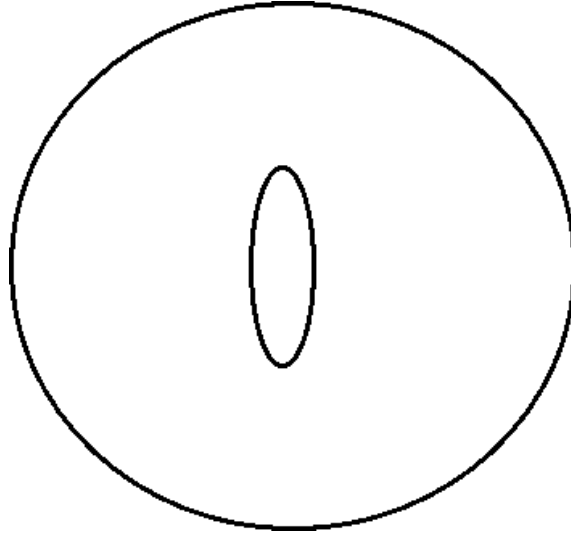


Figure 1.18: *Releasing the surface traction of the inclusion.*

Step 3. We rejoin the material across the cut and remove the inclusion surface traction, which is identical to applying a body force, $F_i = -P_i$ on the surface of the inclusion, as shown in Figure 1.18. We define $u_i(x)$ as the displacement related to F_i .

Based on the expression of Green's function on the elastic body [Challis and Sheard, 2003, Kröner, 1990], $G(x, x')$ is defined as the displacement at x due to the point force at x' . $u_i(x)$ is calculated as:

$$u_i = u_i(x) = \int_0^{S_0} F_i G_{ij}(x, x') dS(x') \quad (1.7)$$

The strain and stress are calculated as :

$$e_{ij} = e_{ij}(x) = \frac{1}{2}(u_{ij}(x) + u_{ji}(x)) \quad (1.8)$$

$$\sigma_{ij} = C_{ijkl}(e_{ij}(x) - e_{ij}^T) \quad (1.9)$$

The strain inside inclusion e_{ij}^{in} can be obtained from the Eshelby's tensor S_{ijkl} through the following relationship:

$$e_{ij}^{in} = S_{ijkl}e_{ij}^T \quad (1.10)$$

The spherical Eshelby's tensor used in our work can be found in Toshio Mura's book [Mura, 2013]. It only depends on the Poisson's ratio, on the shear modulus and on the sphere radius. There are many studies on the plasticity of amorphous systems using Eshelby's inclusion model [Bulatov and Argon, 1994, Dasgupta et al., 2012, Homer et al., 2010, Jagla, 2007, Martens et al., 2011, Nicolas et al., 2015, Picard et al., 2004, Rodney et al., 2011, Talamali et al., 2011, Tanguy et al., 2006] due to its simplicity. The existence of an analytic solution to the inclusion problem for some particular cases, e.g., spherical or cylindrical inclusions, allows for instance to describe the formation of a shear band (SB) as a linear arrangement of Eshelby's inclusions [Dasgupta et al., 2012]. Eshelby's inclusion model is also used within mesoscopic approaches of plasticity [Bulatov and Argon, 1994, Picard et al., 2004, Rodney et al., 2011]. However, these approaches rely on empirical assumptions on the size and the strain of Eshelby's inclusions [Dasgupta et al., 2012, Fusco et al., 2014, Homer et al., 2010, Marmottant and Graner, 2007, Martens et al., 2011, Nicolas et al., 2015, Picard et al., 2004, Talamali et al., 2011, Tanguy et al., 2006], and the mechanisms of nucleation of the inclusions are not well elucidated [Rodney and Schuh, 2009]. Besides, there is still a debate whether stress-strain curves from atomistic simulation can be reproduced with Eshelby's inclusion model. In the recent work of Albaret et al, Eshelby's inclusion model has been successfully applied to study the atomistic plasticity of amorphous silicon for quasistatic shear deformation [Albaret et al., 2016]. It was shown the atomistic stress-strain curves could be reproduced based on Eshelby's inclusion model by combining the information on the stress and displacement field generated by inclusions with atomic-scale displacement from atomistic simulations [Albaret et al., 2016] (Figure 1.19). However, this approach has never been applied to the plasticity of Cu-Zr MGs. An atomic-scale description of plasticity of MG from which we can detect the individual plastic events and determine their numbers, distribution, and sizes, is still lacking.

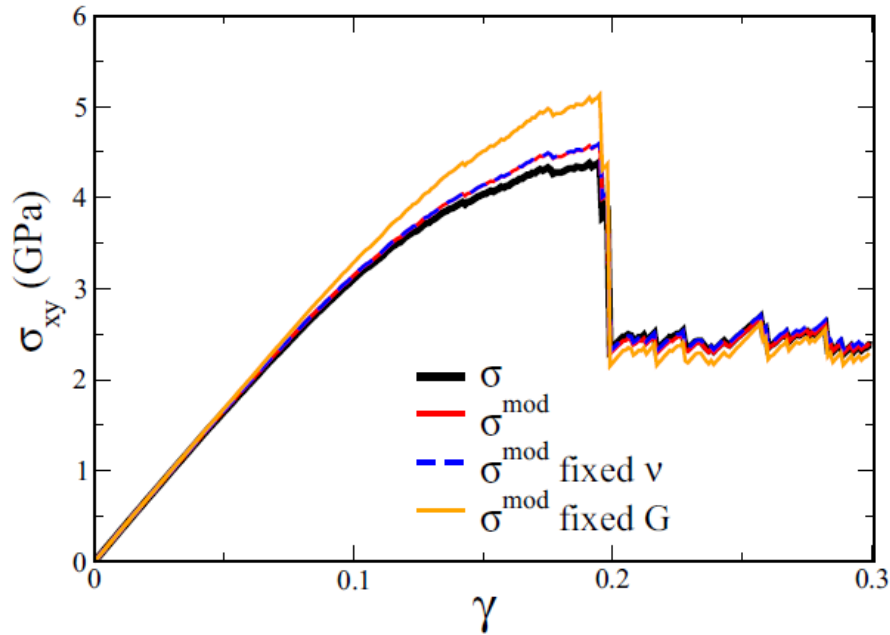


Figure 1.19: Comparison of shear stress-strain curves for amorphous silicon with Stillinger and Weber (SW) potential [Stillinger and Weber, 1985] from MD simulations and with Eshelby's inclusion model. The black curve is the result of the MD simulation. Red, dashed blue and orange curves are obtained with Eshelby's inclusion model [Albaret et al., 2016].

1.7 Molecular Dynamics studies on metallic glasses

Experimentally it is difficult to probe the atomic response of MG during deformation. On the other hand, numerical simulation is very effective in helping us to better understand local dynamical movements at the atomic scale. Molecular dynamics (MD) simulation is a valuable technique to study the dynamics of MGs from the atomistic point of view [Cao et al., 2009].

1.7.1 Studies about structure

SRO and MRO in MGs have been observed with MD simulation [Sha et al., 2011, Sun and Shen, 2009]. Foroughi et al. studied the evolution of the local structure of $Cu_{50}Zr_{50}$ MG during glass formation with the help of MD simulation [Foroughi et al., 2016]. In their research, full and defective full icosahedra (FI) with lower potential energy and mobility are observed from the formation of glass with temperature decrease and the conversion

from other types of icosahedra, mainly $\langle 0,2,8,2 \rangle$ [Foroughi et al., 2016, Zemp et al., 2014]. With temperature decrease, these icosahedra link to each other, and the stability of these connections increases. Moreover, during the deformation of MGs, icosahedra are destroyed and reconstructed. Thus, changes in atomic structure can also be observed with MD [Cao et al., 2009]. It paves the way for studying the correlation between microstructure and plastic behavior of MGs.

1.7.2 Correlation between microstructure and plastic behavior

Many studies have proved that the microstructure of MGs, including morphology, fraction, and distribution, can significantly influence their mechanical properties [Johnson and Samwer, 2005, Khonik et al., 2008, Lewandowski* et al., 2005, Park et al., 2007, Yang et al., 2006b]. Structural heterogeneities inherited from supercooled liquid [Cheng and Ma, 2011] cause heterogeneities of mechanical properties. A great number of soft spots with low energy barriers have been identified in MGs [Manning and Liu, 2011] due to the rapid quenching process. As we mentioned before, the carriers of deformation are regarded as the shear transformation of atomic clusters in STZs [Argon, 1979, Falk and Langer, 1998, Velasco et al., 2017]. Soft spots can turn into potential sites for STZs, i.e., STZs commonly occur where soft spots are fertile [Ding et al., 2014b]. Even though the activation and evolution of STZs are difficult to explore, many relevant studies focus on them by establishing the correlation between microstructure and plastic behavior. Upon deformation, the destruction of FI was identified as the microstructural indication of shear localization [Cao et al., 2009]. According to the research of Cheng et al. [Cao et al., 2009], the formation of a shear band (SB) is accompanied by the breakdown of FI and the localized shear strain squeezed into a narrow band.

Figure 1.20 plots the fraction variation of dominant types of Cu-centered polyhedra with strain. The fraction of FI shows the same trend as stress *vs.* strain. In detail, the fraction of FI changes slightly within the elastic region and plastic flow. However, there is a drop in its fraction when the drop of stress occurs. In general, FI is very stable and shear-resistant [Cheng et al., 2008b, Sheng et al., 2006] and can be significantly destroyed with SB formation. The destruction of FI into fragments leads to structural softening, which

provides potential sites for SB. Therefore, the fraction of FI in the band is much lower than neighboring region.

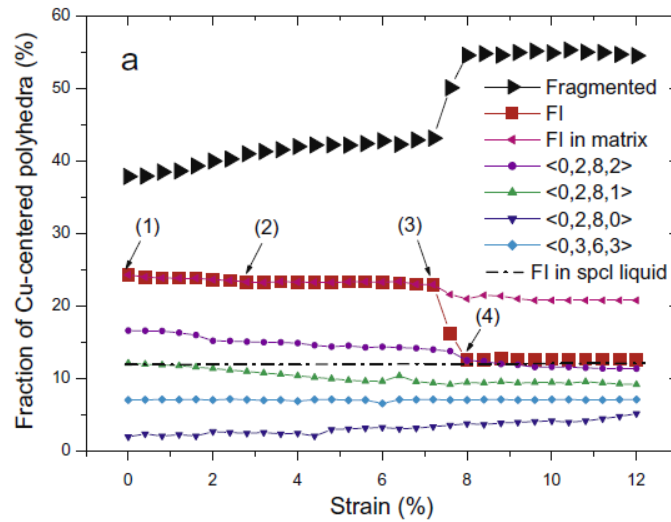


Figure 1.20: Fractions of the five dominant polyhedra types as a function of sample strain in the region that evolves into the localized band [Cao et al., 2009].

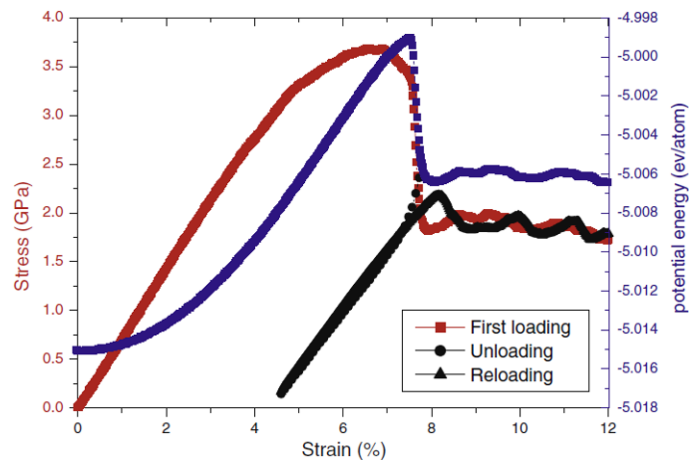


Figure 1.21: The stress-strain curve (the red one), potential energy (the blue one), and unload-reload stress-strain curve (black) with strain [Cao et al., 2009].

Meanwhile, it is observed that the temperature within the SB is higher than the neighboring region, i.e., in SB, there exists thermal softening. As shown in Figure 1.21, an abrupt drop of stress and potential energy is observed upon yielding. In detail, at the beginning of stress decrease after the yield point, potential energy still increases, which is associated with structural rejuvenation within the SB. The accumulated potential energy

within the elastic period is released at the drop of stress. In conclusion, the initiation of unstable shear localization can be attributed to the combined effect of structural rejuvenation, structural softening, and following thermal softening.

1.7.3 Effect on microstructure and mechanical properties

As said previously, the plastic flow of MGs is localized into shear bands (SBs) with a few tens of nm thickness [Greer et al., 2013] when applying loading on them. Therefore, multiple SBs can lead to more homogeneous plastic deformation; nevertheless, catastrophic fracture under a single narrow SB often occurs. The number and distribution of SBs, which can determine mechanical properties, are essential parameters when studying the plasticity of MGs [Conner et al., 2003, Lewandowski* et al., 2005, Liu et al., 2005, Liu et al., 2007, Xing et al., 2001]. Structural characteristics, like icosahedra, free volume, chemical heterogeneity, etc., are related to the nucleation of SBs [Jiang et al., 2009, Lee et al., 2011, Liu et al., 2007, Park and Kim, 2010]. Many experimental researches have proved that the free volume content within SBs is higher than in the matrix, which makes the structural softening and leads to further strain localization or softening [Flores et al., 2002, Li et al., 2002b, Pan et al., 2011, Bei et al., 2006, Yoo et al., 2009].

Many factors can affect the plasticity of MGs, such as cooling rate, temperature, composition, etc. The cooling rate is a critical factor in the atomic arrangement, which plays a vital role in the fraction of FI and the distribution of free volume. Temperature mainly affects thermally atomic mobility. In addition, the fraction of FI is influenced by the atomic arrangement dependent on the difference in atomic sizes.

1.7.3.1 Cooling rate

Yue et al. used MD simulation to study the effect of cooling rate on the microstructure and mechanical properties of $Cu_{50}Zr_{50}$ metallic glass (MG) [Yue et al., 2018]. The result that MGs possess higher T_g with a higher cooling rate is consistent with the experimental result. A lower cooling rate leads to more fraction of full icosahedra clusters [Zemp et al., 2014] and lower free volume [Wang et al., 2009] in MGs, which results in higher yielding strength and elastic modulus. Higher cooling rates induce more free volume in MGs,

which can lead to more homogeneous plastic deformation [Zhong et al., 2016]. Fusco et al. compared the radial distribution of amorphous systems with different quenching rates. They found that more solid-like structures would be formed under lower quenching rates, which results in higher yield stress, flow stress, yield strain (strain where stress is maximum), and larger stress drop [Fusco et al., 2010]. Besides, they obtained detailed information on plastic events in the plastic deformation region under different quenching rates in a model system for amorphous silicon. According to the results, the total number of plastic events decreases when the quenching rate decreases. As for plastic energy, it increases with strain. They also found that plastic events are less and smaller for the amorphous system with a lower quenching rate. In contrast, the plastic energy is larger at the yield point, which means that at yield strain, a larger amount of plastic energy is released rapidly. Therefore, it is more likely to generate a shear band at the yield point for the amorphous system with lower quenching rates. However, similar studies about the detailed analysis of the local plastic events of MGs are lacking.

1.7.3.2 Temperature

At high temperature (2000 K), metallic glasses (MGs) are liquid-like structures as it can be seen from the radial distribution function (RDF) analysis [Song et al., 2017, Wen et al., 2021]. When the temperature decreases to the glass transition temperature (T_g), the liquid is frozen to solid glass. Below the T_g , the atomic packing density increases with the temperature decreasing while atomic mobility and diffusion decrease [Song et al., 2017, Wen et al., 2021] because the atomic diffusion is thermally activated. Less shear transformation zones (STZs) are activated, attributed to the less atomic diffusion [Sepulveda-Macias et al., 2018]. More full icosahedra (FI) and less free volume are observed in MGs [Yue et al., 2020]. Regarding mechanical properties, as a consequences, during deformation, the plastic flow is less homogeneous, and the plasticity is poorer [Yue et al., 2020]. However, the yield strength, shear and bulk moduli increase when temperature decreases [Sepulveda-Macias et al., 2018, Yue et al., 2020].

1.7.3.3 Composition

The effect of composition on the plasticity of MGs can be ascribed to its influence on the formation of icosahedra clusters with different central elements [Zhong et al., 2016]. In a binary metallic glass with Zr and Cu elements, the initial fraction of FI increases dramatically with the rise of copper composition. In a ternary metallic glass with Zr, Cu, and Al elements, when the fraction of Cu is fixed, the fraction of FI increases slightly with the fraction of Al [Cheng et al., 2008a]. Correspondingly, the mechanical behavior is strongly affected by the composition. For example, by increasing the Cu content, the overshoot stress (τ_{over}) and flow stress (τ_{flow}) are larger. Moreover, the difference between overshoot stress and flow stress, $\Delta\tau$, measuring the propensity to strain localization, also increases with more Cu content, which can be correlated with a higher of FI. Likewise, the fraction of FI and $\Delta\tau$ both increase slightly with the Al fraction. Therefore, to sum up, Cu and Al content negatively affect the plasticity of MG due to the formation of more FI, which are resistant to shear transformation and reduce ductility [Cheng et al., 2008b, Park et al., 2007].

1.8 Improvement of plasticity

Many studies evaluate different methods to improve the plasticity of metallic glasses (MGs). On the experimental side, plasticity can be improved by shot peening (SP), laser-shot-peening (LSP), laser surface melting (LSM), etc. Both types of shot peening have a similar effect on MGs, i.e., introducing a soft layer and residual stress. This enhances shear band nucleation and structural dilation, further resulting in lower yield strength [Wang et al., 2011] and plastic stability. Compared to SP, LSP can locate the target precisely via laser beam and cause a deeper residual stress layer [King et al., 2006]. LSM applies laser on the surface of MGs to remelt and resolidify, introducing residual stress and improvement of strength [Chen et al., 2012]. In addition, after pre-deformation, like cold rolling, the entire material experiences structural dilation and softening [Liu et al., 2010], which is beneficial to stable and homogeneous plastic deformation [Yokoyama, 2003, Yokoyama et al., 2002]. Apart from the surface modification, the addition of other

elements inducing a larger amount of excess free volume [Chen et al., 2008] can also help to improve the plasticity of MGs [Li et al., 2021]. Molecular Dynamics (MD) simulation is also widely applied to better understand the microstructural mechanisms allowing to improve plasticity of MGs. At the microscopic scale, plasticity can be improved by activating more STZs, generating multiple homogeneous shear bands (SBs) and avoiding the propagation of a single SB. In the following, studies about the enhancement of ductility of MGs via MD simulation will be introduced.

1.8.1 Composite metallic glasses

The introduction of a second phase is a practical approach to improving the ductility of MGs. The presence of a crystalline phase causes the existence of interfaces, which leads to the increase of free volume [Shete et al., 2016]. In addition, STZ localization and embryo SBs are likely to generate near structural heterogeneities, such as interfaces. Simultaneously, interfaces hinder the catastrophic extension of a single SB, further promoting the formation of homogeneous distribution of local shear strain and improving the global plasticity of MGs [Lee et al., 2005, Şopu et al., 2011, Zhou et al., 2013]. For instance, a copper crystallized phase was embedded in $Cu_{64}Zr_{36}$ MG, and the generation and development of the SB were observed [Albe et al., 2013]. Precipitates can also promote the generation of multiple SBs and block the propagation of a single SB. However, at high strains, SBs can still go through precipitates because the thickness of SBs can cover the diameter of precipitates.

The impact of the introduction of an amorphous second phase was also studied via MD simulation [Song et al., 2019]. Song et al. introduced a soft phase with structural defects into the MG matrix. They observed that when the defective atomic fraction is up to 12.5 %, it can cause a free volume gradient at the interfaces. It results in a stress concentration, activating more STZs with large atomic shear strain. Interfaces can also be formed in nanoglasses, which are obtained by powder consolidation [Jing et al., 1989].

1.8.2 Pre-deformation

The introduction of a notch can enhance the ductility of MGs, as it has been proved by experiments [Guo et al., 2011, Pan et al., 2017, Qiao, 2013, Zhao et al., 2010a]. There is evidence of a transition from brittle to ductile fracture in the notched MG under deformation [Zhao et al., 2010b]. Zhao et al. found that two symmetrical notches can improve the plasticity by up to 10 % through the initiation of SBs and hinder the propagation of a single SB. They also found that the initiation of SBs can be attributed to the stress concentration around the notches, and the obstruction of propagation of a single SB was due to the intersection of multiple SBs. The notched samples will finally fracture via necking [Guo et al., 2007].

In addition, computer simulations about notches in the MG were also performed, including finite element analysis [Dutta et al., 2018] and molecular dynamics (MD) [Feng et al., 2020]. At the microscopic scale, it was demonstrated that the nucleation of SBs in the indent-notch affected region was hindered by the formation of densely-packed clusters. Meanwhile, the stress concentration around notch roots is observed. Therefore, there will be a competition between the nucleation of SBs outside the indent-notch affected region and the localized deformation due to stress concentration around notch roots. The plastic behavior depends on the depth of notches. When the depth of notches is relatively larger, the nucleation of SBs outside the indent-notch affected region plays a dominant role, and there will be ductile behavior.

Feng et al. studied the rejuvenation of $Zr_{46}Cu_{46}Al_8$ MG through pressure preloading on it [Feng et al., 2018]. The stress-strain curves and distribution of atomic local shear strain obtained by MD simulation demonstrate that the preloading on MG leads to the increase of SRO and decrease of MRO, resulting in the structural rejuvenation and more stable plastic deformation.

1.8.3 Thermal pre-treatment

Thermal pre-treatment process is another useful method that can improve the plastic behavior of MGs without destroying the integrity of the material. For instance, an annealing treatment above T_g brings in more flow units, STZs, and more free volume, which is

beneficial to homogeneous plastic deformation for MGs [Feng et al., 2015]. Through MD simulation, Wakeda et al. investigated the microstructure and mechanical properties of binary Zr-Cu MG under pre-thermal process, i.e., after a secondary heating and quenching process [Wakeda et al., 2015]. When the re-quenching rate is lower than or equal to the initial quenching rate, aging appears, no matter how high the annealing temperature. Rejuvenation occurs only when the re-quenching rate is higher than the initial quenching rate and the annealing temperature is higher than a specific value. Thus, it is concluded that the level of rejuvenation does not depend on the absolute value of the re-quenching rate, but rather on the ratio between the re-quenching rate and the initial quenching rate. Another commonly applied thermal treatment is the cryogenic thermal cycling (CTC), i.e. a thermal cycle from room temperature to a lower temperature repeatedly at a constant pressure [Song et al., 2018]. It has been proved by Shang et al. that CTC can lead to a rejuvenation effect on MGs by inducing structural heterogeneity and triggering local shear transformations [Shang et al., 2018]. It is found that the number of cycles and amplitude of temperature are two significant factors for CTC. When the number of cycles increases, the density of plastic events grows gradually leading to a pronounced rejuvenation effect. Similarly, internal thermal stress increases correspondingly by increasing the amplitude of the cycle high temperature. Thus, an approximate increase of the number and amplitude (towards higher temperature) of thermal cycles has a positive effect on the improvement of plasticity. The influence of several relevant parameters on the rejuvenation of MGs was also studied by Shang et al. via MD simulation [Shang et al., 2021]. They concluded that a cycle with a lower initial quenching rate, less holding time at the lowest or highest temperatures, and higher re-quenching and re-heating rate is more efficient to rejuvenate MGs and therefore improve their ductility. Nikolai found the enhancement of CTC on the plasticity of MGs was supported by experimental studies. [Priezjev, 2019]. Guo et al. [Guo et al., 2018] compared compressive stress-strain curves of MG sample before and after deep cryogenic treatment from 20 °C to -180 °C, repeated over 30 cycles (DCT30), and they observed that the MG sample can form more SBs during compressive deformation after cryogenic thermal cycling treatment. In conclusion, the improvement of the plasticity of MGs by various methods has attracted much attention, both in experiments and numerical simulations. However, the

deep understanding of the impact of these methods on the development of plastic events during deformation is still missing. Thus, this thesis focuses on the detailed characterization of these plastic events.

1.9 Open questions

The literature devoted to the microstructure and mechanical properties of MGs is already very abundant. However, some open questions still remain, that we will address in this thesis.

How do we detect plastic events and extract the relevant information about them?

A well-established method to identify and characterize individual plastic events in MGs has not been fully developed yet. In this work, we will use an approach for their detection based on local energy variations, through a coarse-graining procedure [Goldenberg and Goldhirsch, 2004]. In this way, the distribution, size, and intensity of plastic events will be obtained. This is mandatory to study the activation and propagation of plastic events with deformation.

What is the effect of quenching rates on the occurrence of plastic events of metallic glasses during deformation?

As already illustrated in Section 1.7.3.1, the effect of quenching rates on the microstructure of MGs has been studied a lot. However, only very few works address the effect of the quenching rate on the plastic events, which determine the initiation and development of shear transformation with deformation. This is crucial to understand the microscopic origin of the plastic behavior of MGs, and in particular the transition from localized to homogeneous plasticity when the quenching rate is increased.

What is the effect of cryogenic thermal cycling treatment (CTC) on the plastic events of metallic glasses occurring during deformation?

According to the previous studies, cryogenic thermal cycling (CTC) treatment promotes more homogeneous plastic deformation on metallic glasses, through structural rejuvenation, inducing extra free volume, higher energy, and enthalpy. The effect of CTC on the development of plastic events is however missing. We will establish the link between the local atomic dynamics and the observed mechanical properties by analyzing them.

Chapter 2

Methodology and modeling

Contents

2.1	Molecular dynamics simulation	38
2.1.1	Newton's equation and algorithms	38
2.1.2	Interatomic potentials	39
2.1.3	Ensemble of molecular dynamics simulation for an equilibrium system	40
2.1.4	Periodic boundary conditions	44
2.2	Structural analysis	45
2.2.1	Radial distribution function	45
2.2.2	Voronoi polyhedra	46
2.2.3	Local atomic shear strain	46
2.3	Construction of model and deformation	47
2.4	Analysis and mapping of plastic events	48
2.4.1	Definition of plastic events	48
2.4.2	Selection of attractors	50
2.4.3	Rearrangement of plastic events	52
2.4.4	Atomic displacement fitting	52
2.4.5	Fitting of the stress-strain curve	54
2.5	Conclusion	56

2.1 Molecular dynamics simulation

In Molecular Dynamics (MD) simulation, Newton's equations of motion determine the movement of atoms and molecules under the action of the force fields created by surrounding atoms. At time t , the force on each atom can be obtained from the interaction potential between atoms. After Δt , the position and velocity of each atom i can be computed through the equation of motion. Moreover, thermodynamic, structural, and other macroscopic properties can be calculated using statistical methods.

2.1.1 Newton's equation and algorithms

The position and velocity of atoms are determined by Newton's equation in MD simulation, which is:

$$m_i a_i = f_i = \sum_{j \neq i} f_{ij} \quad (2.1)$$

where m_i is the mass of atom i , a_i is the acceleration of atom i and f_i is the interaction force between atoms. Newton's equation needs to be solved by the numerical integration method to study the many-body problem. The numerical algorithms include Verlet algorithm [Verlet, 1967], Velocity-Verlet algorithm [Swope et al., 1982], Leap-frog algorithm [Hockney, 1970], Beeman algorithm [Beeman, 1976], Gear algorithm [Gear, 1971] and Rahman algorithm [Rahman, 1964], among which, Verlet algorithm and Velocity-Verlet algorithm are commonly used.

The principle of the Verlet algorithm is to compute the positions $\mathbf{r}(t+\Delta t)$ and $\mathbf{r}(t-\Delta t)$ by two Tertiary Taylor Polynomials about position $\mathbf{r}(t)$, respectively.

$$\mathbf{r}(t + \Delta t) = \mathbf{r}(t) + \mathbf{v}\Delta t + \frac{1}{2}\mathbf{a}(t)\Delta t^2 + \frac{1}{6}\mathbf{b}(t)\Delta t^3 + \mathbf{O}(\Delta t^4) \quad (2.2)$$

$$\mathbf{r}(t - \Delta t) = \mathbf{r}(t) - \mathbf{v}\Delta t + \frac{1}{2}\mathbf{a}(t)\Delta t^2 - \frac{1}{6}\mathbf{b}(t)\Delta t^3 + \mathbf{O}(\Delta t^4) \quad (2.3)$$

where $\mathbf{r}(t)$ is the position, $\mathbf{v}(t)$ is the velocity, $\mathbf{a}(t)$ is the acceleration, and $\mathbf{b}(t)$ is third derivative of the position with respect to the time. By combining these two equations, we

obtain:

$$\mathbf{r}(t + \Delta t) = 2\mathbf{r}(t) - \mathbf{r}(t - \Delta t) + \mathbf{a}(t)\Delta t^2 + \mathbf{O}(\Delta t^4) \quad (2.4)$$

The truncation error is of order Δt^4 . Verlet algorithm is accurate, stable, and easy to use, but it cannot compute velocity directly. Thus, the Velocity-Verlet algorithm, is used for this purpose. In this one, positions and velocities are updated every timestep. At first, the position is updated:

$$\mathbf{r}(t + \Delta t) = \mathbf{r}(t) + \mathbf{v}(t)\Delta t + \frac{1}{2}\mathbf{a}(t)\Delta t^2 \quad (2.5)$$

and then forces are obtained from potential. At last, velocities are updated:

$$\mathbf{r}(t + \Delta t) = \mathbf{r}(t) + \mathbf{v}(t + \frac{1}{2}\Delta t)\Delta t \quad (2.6)$$

$$\mathbf{v}(t + \frac{1}{2}\Delta t) = \mathbf{v}(t) + \frac{1}{2}\mathbf{a}(t)\Delta t \quad (2.7)$$

$$\mathbf{a}(t + \Delta t) = -\frac{1}{m}\nabla V(r(t + \Delta t)) \quad (2.8)$$

$$\mathbf{v}(t + \Delta t) = \mathbf{v}(t + \frac{1}{2}\Delta t) + \frac{1}{2}\mathbf{a}(t + \Delta t)\Delta t \quad (2.9)$$

The accuracy of the Velocity-Verlet algorithm is controlled by the timestep, Δt , i.e., smaller timestep means better accuracy, while larger timestep means faster performance. Therefore, it is crucial to choose a suitable Δt . The optimal choice is 1/100 of the period of the fastest vibration of the system.

2.1.2 Interatomic potentials

Potentials describe interatomic potential energy based on atomic coordinates, which include pair potential and multibody potentials. The accuracy and relevancy of MD calculation depends on them. Pair potentials consider attractive and repulsive contribution between a pair of atoms. The most widely used one is Lennard-Jones (L-J) potential [Allen

and Tildesley, 2017, Ashcroft and Mermin,], and it can be expressed as:

$$\phi(r_{ij}) = \varepsilon[(\sigma/r_{ij})^{12} - (\sigma/r_{ij})^6] \quad (2.10)$$

ε is an energetic parameter; σ is a length parameter; r_{ij} is the distance between atom i and atom j . The first term indicates the attractive long-range interaction, and the second indicates the short range repulsing interaction. Multibody potentials can describe the interaction of the N -body ($N \geq 3$). Widely used multibody potentials are the embedded atomic method (EAM) [Daw and Baskes, 1984] and Finnis-Sinclair (FS) potential [Finnis and Sinclair, 1984]. According to the Hohenberg-Kohn theorem [Hohenberg and Kohn, 1964], Stott and Zaremba supposed that the energy of an embedded atom at position x is a function of electron density ρ [Stott and Zaremba, 1980]. The principle of EAM is to treat each atom in the system as an embedded atom in the matrix of other atoms [Daw and Baskes, 1984, Daw and Baskes, 1983]. The total potential energy is the sum of the pair potential between the atoms in the lattice and the embedded energy of the atoms embedded in the electron cloud. EAM potential can be expressed as:

$$E_{pot} = \sum_i F_i(\rho_i) + \frac{1}{2} \sum_{ij} \phi_{ij}(r_{ij}) \quad (2.11)$$

where $F(\rho_i)$ is embedding energy function, i.e., the energy of an atom surrounded by electron density ρ_i , which is the sum of electron density of all atoms j surrounding atoms of atom i ($\rho_i = \sum_j \rho(r_{ij})$); $\phi_{ij}(r_{ij})$ is pair potential depending on the distance (r_{ij}) between atom i and j . Finnis-Sinclair (FS) potential is issued based on EAM potential. The only difference between them is the explanation of electron density, ρ_i , and embedded potential energy [Finnis and Sinclair, 1984].

2.1.3 Ensemble of molecular dynamics simulation for an equilibrium system

In statistical physics, an ensemble represents a large set of possible states of a system under certain conditions. In other words, an ensemble is a probability distribution of the states of a system. The commonly used ensembles in MD simulation are micro-canonical ensemble, canonical ensemble, isothermal isobaric ensemble and isothermal isenthalpic

ensemble.

Micro canonical ensemble, also called NVE ensemble, is an isolated, conservative statistical ensemble of systems. It keeps the total number of atoms N , volume V and energy E all constant. Canonical ensemble, also called NVT ensemble, keeps the number of atoms N , volume V and temperature T constant and total kinetic energy zero. Isothermal isobaric ensemble, which is NPT ensemble, keeps the number of atoms N , pressure P , and temperature T constant. The temperature and pressure are controlled as explained later. Temperature is controlled by methods such as velocity calibration method [Heerman, 1987], Berendsen method [Berendsen et al., 1984], Gaussian method [Hoover, 2012], and Nose-Hoover method [Hoover, 2012, Nosé, 1984].

In the velocity calibration method, due to the relationship between velocity and temperature of the system, the temperature can be adjusted by calibrating velocity. If the temperature of the system at time t is $T(t)$, and velocity is calibrated with a factor λ , then the variation of temperature can be determined:

$$\Delta T = T_{exp} - T(t) \quad (2.12)$$

$$\Delta T = (\lambda^2 - 1)T(t) \quad (2.13)$$

$$\lambda = \sqrt{\frac{T_{exp}}{T(t)}} \quad (2.14)$$

T_{exp} is the expected value of temperature.

Berendsen method is another algorithm that assumes that the system couples to a heat bath, whose temperature is the target value and keeps the temperature of the system constant by heat exchange with the heat bath. The variation of temperature at each step is:

$$\Delta T = \frac{\delta t}{\tau} (T_{bath} - T(t)) \quad (2.15)$$

where δt is the time interval, T_{bath} is the temperature of the heat bath, and τ is the time constant. Calibration factor of velocity, λ :

$$\lambda = \sqrt{1 + \frac{\delta t}{\tau} \left(\frac{T_{bath} - T(t)}{T(t)} \right)} \quad (2.16)$$

The Gaussian method adds a frictional force, ζ_G on each atom as follows:

$$\frac{m_i d^2 r_i}{dt^2} = F_i - m_i \zeta_G v_i \quad (2.17)$$

where, $m_i \zeta_G v_i$ is the term of friction force. $\zeta_G = (\sum_j v_j F_j) (\sum_k m_k v_k \cdot v_k)^{-1}$ is the damping factor. If ζ_G is positive, it means the temperature is higher than that of the heat bath, and the system should be cooled, otherwise, the system should be heated. The temperature control is based on the kinetic energy of the total system.

The Nose-Hoover method supposes that the system is coupled to a virtual heat bath, in which the system can release and receive heat freely from the heat bath. The equation of motion of this method is similar to that of the Gaussian method, and differs only by the expression of the factor of the friction force. In this method, a Hamiltonian H^* (total energy of the system) with an extra degree of freedom for the heat bath, s , is defined:

$$H^* = \sum_i \frac{\mathbf{p}_i^2}{2ms^2} + \frac{1}{2} \sum_{ij, i \neq j} U(\mathbf{r}_i - \mathbf{r}_j) + \frac{p_s^2}{2Q} + 3Nk_B T_{exp} \ln s \quad (2.18)$$

where N is the number of particles, and $k_B = 1.38 \times 10^{-23}$ J/K is the Boltzmann's constant. Q is an effective mass controlling the coupling of the system to the heat bath and \mathbf{p}_s is the conjugate momentum of s . \mathbf{p}_i and \mathbf{r}_i are so-called "virtual coordinates", which are related to the real coordinates \mathbf{r}_i' and \mathbf{p}_i' as follows:

$$\mathbf{r}_i' = \mathbf{r}_i, \mathbf{p}_i = \frac{\mathbf{p}_i}{s} \quad (2.19)$$

where the coordinates with accents are the real ones. Hamiltonian deduced the motion equation:

$$\dot{\mathbf{r}}_i' = \frac{\partial H}{\partial \mathbf{r}_i'} = \frac{\mathbf{p}_i'}{m} \quad (2.20)$$

$$\eta = \frac{\mathbf{p}_s}{Q} \quad (2.21)$$

$$\dot{\mathbf{p}}'_i = -\frac{\partial H}{\partial \mathbf{p}'_i} = F_i - \eta \dot{\mathbf{r}}'_i \quad (2.22)$$

$$\ddot{\mathbf{r}}'_i = \frac{\mathbf{F}_i}{m} - \eta \dot{\mathbf{r}}'_i \quad (2.23)$$

$$\dot{\eta} = \frac{1}{\tau^2} \left(\frac{T}{T_{exp}} - 1 \right) \quad (2.24)$$

$$\tau = \sqrt{\frac{Q}{3Nk_B T_{exp}}} \quad (2.25)$$

where $F_i = \frac{\partial U}{\partial \mathbf{r}_i}$ is the force acting on atom i , η is the damping factor and τ is the relaxation time of heat bath. τ is the input data in the command file of LAMMPS. Typical values are used such as 1 ps. T_{exp} is the target temperature imposed to the system.

The commonly used methods of controlling pressure are Berendsen [Berendsen et al., 1984] and Parrinello-Rahman [Parrinello and Rahman, 1981, Parrinello and Rahman, 1982]. In the Berendsen method (similar to that used for temperature control), it is assumed that the system is coupled to a virtual pressure bath. The calibration factor of volume, λ , is expressed as:

$$\lambda = 1 + k \frac{\delta t}{\tau_p} [P(t) - P_{bath}] \quad (2.26)$$

where k and τ_p are coupling parameters, P_{bath} is the expected pressure and $P(t)$ is the instant pressure at time t . This method can adjust the pressure in three directions simultaneously. But it cannot realize the change of dimensions in three spatial directions of the system under shear stress. To realize the change of shape and volume simultaneously and obtain the equilibrium with external pressure, Parrinello-Rahman issued Parrinello-Rahman method of controlling pressure [Parrinello and Rahman, 1981], which is widely used in MD simulation.

2.1.4 Periodic boundary conditions

Due to the limitation of the number of particles that can be introduced in MD simulation and the necessity of a large system size to study the macroscopic properties of the material, periodic boundary conditions are implemented. The principle is to consider the system containing the particles as a cell and replicate it in three directions so that cells can extend periodically. Meanwhile, atoms around the left boundary and right boundary, atoms around the top and bottom boundary, and atoms around the front boundary and back boundary all have interaction, which can cause atoms to go through boundaries, as shown in Figure 2.1. In this thesis, we calculate the atomic displacement using minimum image convention, which is illustrated in Figure 2.2. When an atom moves from the position of light blue circle to the dark blue one, we can get two atomic displacement vectors due to periodic boundary condition: when we use minimum image convention, we just calculate the smallest one for the atomic displacement.

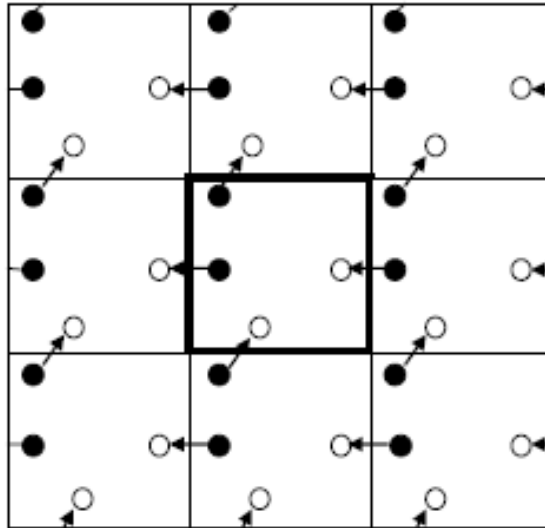


Figure 2.1: 2-dimensional schematic diagram of periodic boundary conditions [Stepanov, 2013].
Filled circles to open circles mean the movement of atoms after displacement.

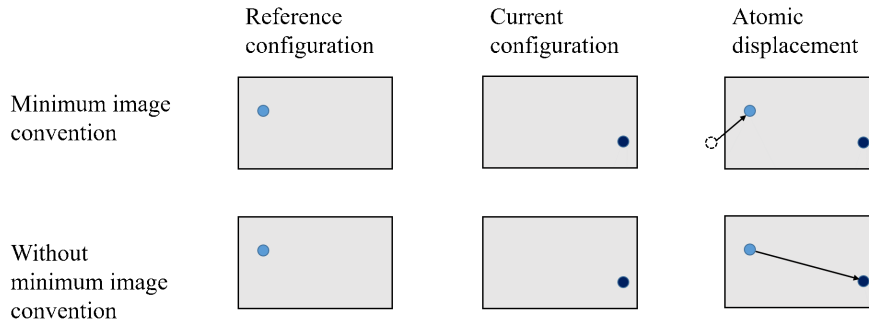


Figure 2.2: Schematic of atomic displacement calculation with and without minimum image convention.

2.2 Structural analysis

2.2.1 Radial distribution function

Several important parameters are used for the structural analysis of metallic glasses (MGs). First, the radial distribution function (RDF), $g(r)$, is defined by the probability of finding another atom at a distance, r , from a given atom [Bernal, 1960a], which has been briefly introduced in Section 1.4. $g(r)$ can be calculated as follows:

$$g(r) = \frac{L^3}{N^2} \left\langle \left[\sum_{i=1}^N n(r) \right] / 4\pi r^2 \Delta r \right\rangle \quad (2.27)$$

where L is the length of the simulation box, N is the number of atoms, and $n(r)$ is the number of atoms within the radius of the spherical shell from r to $r + \Delta r$. When more than one element is present in the modeling system, we can define partial RDFs, $g_{\alpha\beta}(r)$, by calculating the number of β atoms within the radius of the spherical shell from r to $r + \Delta r$, taking each α atom as the center atom of the sphere. Its expression is:

$$g_{\alpha\beta}(r) = \frac{L^3}{N_\alpha N_\beta} \left\langle \left[\sum_{i=1}^{N_\alpha} n_{i\beta}(r) \right] / 4\pi r^2 \Delta r \right\rangle \quad (2.28)$$

L is still the length of the box, N_α , N_β is the number of α and β atoms, and $N_{i\beta}$ is the number of β atoms within the radius of the spherical shell from r to $r + \Delta r$ when the α atom is the center atom of the sphere. According to the definition of partial RDFs, $g_{\alpha\beta}(r) = g_{\beta\alpha}(r)$. There are $N(N+1)/2$ partial RDFs in an N -tuple system, and the total partial RDF

is the weighted sum of $N(N+1)/2$ partial RDFs.

2.2.2 Voronoi polyhedra

Even though the RDF can give an idea of the distribution of atoms, it cannot describe the geometric diagram and characteristics of atomic clusters. Therefore, Voronoi polyhedra are used to describe the local structure of MGs. They have been already introduced In Section 1.4. Voronoi polyhedral volume can be used to study the local packing density, and the fraction variation of Voronoi polyhedron is a key parameter during MG's deformation. These two parameters can be calculated by the software Open Visualization Tool (OVITO) through the operation "Voronoi analysis". In our case, it will be used to calculate the fraction of $\langle 0, 0, 12, 0 \rangle$ icosahedra (full-icosahedra FI) at a given strain.

2.2.3 Local atomic shear strain

To visualize shear transformations (STs) and shear bands (SBs), and understand the atomic rearrangement during the deformation of MGs, the local atomic shear strain, η_j^{Mises} can also be calculated [Shimizu et al., 2007]. The calculation needs two atomic configurations, the referenced one and the current one. First, a local transformation gradient tensor J_i must be calculated. It conforms to the following relationship [Shimizu et al., 2007]:

$$\{\mathbf{d}_{ji}^0\} \rightarrow \{\mathbf{d}_{ji}\}, \forall j \in N_i^0 \quad (2.29)$$

where \mathbf{d} 's are vector separations (row vectors) between atom j and i (superscript 0 means the reference configuration). Here, j is one of atom i 's nearest neighbors, N_i^0 is the total number of the nearest neighbor of atom i . J_i can be obtained via minimizing the following expression:

$$\sum_{j \in N_i^0} |\mathbf{d}_{ji}^0 J_i - \mathbf{d}_{ji}|^2 \rightarrow J_i = \left(\sum_{j \in N_i^0} \mathbf{d}_{ji}^{0T} \mathbf{d}_{ji}^0 \right)^{-1} \left(\sum_{j \in N_i^0} \mathbf{d}_{ji}^{0T} \mathbf{d}_{ji} \right) \quad (2.30)$$

And then Lagrangian strain matrix can be calculated by:

$$\eta_i = \frac{1}{2} (J_i J_i^T - 1) \quad (2.31)$$

The local shear invariant of atom i can be obtained by:

$$\eta_i^{Mises} = \sqrt{\eta_{yz}^2 + \eta_{xz}^2 + \eta_{xy}^2 + \frac{(\eta_{yy} - \eta_{zz})^2 + (\eta_{xx} - \eta_{zz})^2 + (\eta_{yy} - \eta_{xx})^2}{6}} \quad (2.32)$$

η_j^{Mises} is the parameter measuring local non-elastic deformation [Falk and Langer, 1998], which can be calculated by analysis and visualization software OVITO. Meanwhile, the intensity of η_j^{Mises} can be visualized through color coding by OVITO [Stukowski, 2009].

2.3 Construction of model and deformation

The metallic glass (MG) model used in this thesis is Cu-Zr binary alloy, for which reliable interatomic potentials are available, and the atomic structure has been well investigated [Cheng and Ma, 2011]. The potential we used is Sheng's EAM potential [Cheng and Ma, 2011]. Most of the simulation performed in this thesis, where the material is sheared, include 32000 atoms. They are cubic lattices with lengths of approximately 8 nm. For tensile deformation simulation, parallelepiped boxes with 64000 atoms are created, i.e., the edge along the tensile direction is twice as large as that of the model for shear.

When studying the effect of composition, We selected three different compositions, i.e., $Cu_{64}Zr_{36}$, $Cu_{50}Zr_{50}$, and $Cu_{36}Zr_{64}$. The potentials used for all of the models are Sheng's potential [Cheng et al., 2009b]. First, we prepare the cubic or parallelepiped lattice with Cu atoms and then replace some of them randomly with Zr atoms to obtain the desired compositions. The MG system is obtained by melt quenching to obtain a random atomic arrangement. In our cases, the system is heated to 2000 K and maintained at this temperature for 2 ns to ensure the chemical homogeneity; it is then quenched down to 0.1 K, with different quenching rates, ranging from 10^{10} K/s to 10^{14} K/s, and kept at this low temperature for 2 ns likewise.

After the construction of the MG model, we apply quasi-static and dynamic shear and tensile deformation to the box.

For quasi-static deformation, strain reaches 30 %, and strain increment $\delta\gamma=0.1$ % at each step. After each strain step, the potential energy is minimized with the Fast Inertial Relaxation Engine (FIRE) algorithm at very low temperature, 0.1 K. FIRE algorithm can

add velocity modifications and adaptive time steps according to the last iteration result, which is rather faster than the conjugate gradient (CG) algorithm [Bitzek et al., 2006, Eidel et al., 2011]. The criterion of force after minimization should be magnitude of 10^{-3} .

For dynamic deformation, different strain rates are tested: 10^7 s^{-1} , 10^8 s^{-1} and 10^9 s^{-1} . Pressure is kept at 0 during preparation and deformation, and temperature is controlled at 0.1 K, or at higher temperatures if thermal effects are studied (cf. Chapter 3). The thermostat is Nose-Hoover thermostat.

2.4 Analysis and mapping of plastic events

2.4.1 Definition of plastic events

To analyze the quasi-static simulations, we treat plasticity as an inclusion problem. The local plastic transformation zones are considered as inclusions in an isotropic homogeneous elastic medium, as introduced in Section 1.6. The intensity of plastic energy is computed to identify the plastic events. Since the temperature is kept at 0.1 K all the time, thermal effect can be ignored. After application of quasi-static shear deformation on the system, we define $\{i\}^{curr}$ as the configuration of forward deformation with $\delta\gamma$ at step i , and $\{i\}^{rev}$ as the configuration of reverse deformation with $-\delta\gamma$ at step i .

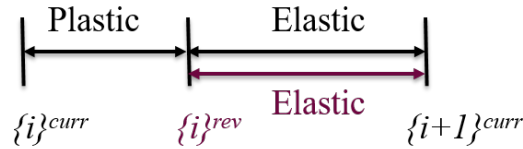


Figure 2.3: The schematic diagram of forward deformation and reverse deformation.

From step $\{i\}^{curr}$ to $\{i+1\}^{curr}$, the energy variation includes plastic and elastic contributions, as shown in Figure 2.3. When applying reverse deformation on it, $\{i\}^{rev}$ is reached instead of $\{i\}^{curr}$ from $\{i+1\}^{curr}$, because the plastic contribution is irreversible. When, there is no plastic event occurring, the difference of energy between $\{i\}^{rev}$ and $\{i\}^{curr}$, $\delta E_{i \rightarrow i+1}^{pl} = E_i^{curr} - E_i^{rev}$ is nearly zero within numerical accuracy. In contrast, if a plastic event exists, then the plastic energy between two successive steps can be computed. For each atom, it can be computed considering the interaction of the center atom with the

surrounding ones. The plastic energy on atom i_a follows:

$$PE_{at}(i_a) = \left(\sum_{j_a} \left| V_{i_a, j_a}^{2b}(\{\mathbf{r}\}^{curr}) - V_{i_a, j_a}^{2b}(\{\mathbf{r}\}^{rev}) \right|^2 + \sum_{j_a} \sum_{k_a} \left| V_{i_a, j_a}^{mb}(\{\mathbf{r}\}^{curr}) - V_{i_a, j_a}^{mb}(\{\mathbf{r}\}^{rev}) \right|^2 \right)^{\frac{1}{2}} \quad (2.33)$$

where, $\{\mathbf{r}\}^{curr}$ and $\{\mathbf{r}\}^{rev}$ are the current configuration and reverse configuration, respectively. V_{i_a, j_a}^{2b} and V_{i_a, j_a}^{mb} are respectively the two-body and multi-body part of the EAM potential introduced in Eq. 2.11.

In order to build a continuous plastic energy field $PE(\mathbf{r})$ from the atomic plastic energy defined in Eq. 2.33, we use a coarse-graining procedure [Goldenberg and Goldhirsch, 2004] by averaging the atomic plastic energy with a spatial Gaussian function as follows:

$$PE(\mathbf{r}) = \sum_{i_a} PE_{at}(i_a) \left(\frac{1}{(\pi\omega^2)^{\frac{3}{2}}} e^{-\frac{|\mathbf{r}-\mathbf{r}_{i_a}|^2}{\omega^2}} \right) \quad (2.34)$$

where ω is the Gaussian width, which is taken of the order of the average first-neighbor distance. For the binary metallic glass system $Cu_{64}Zr_{36}$ used, the value of ω is 2.8 Å. $PE(\mathbf{r})$ can be plotted on a 3D grid, where we can notice the presence of several peaks, as shown in Figure 2.4. We define these peaks as attractors, which are indicated in in Figure 2.5, and the whole region surrounding an attractor is defined as a basin of attraction, i.e., the region of the space traversed by all the gradient paths that terminate at this attractor.

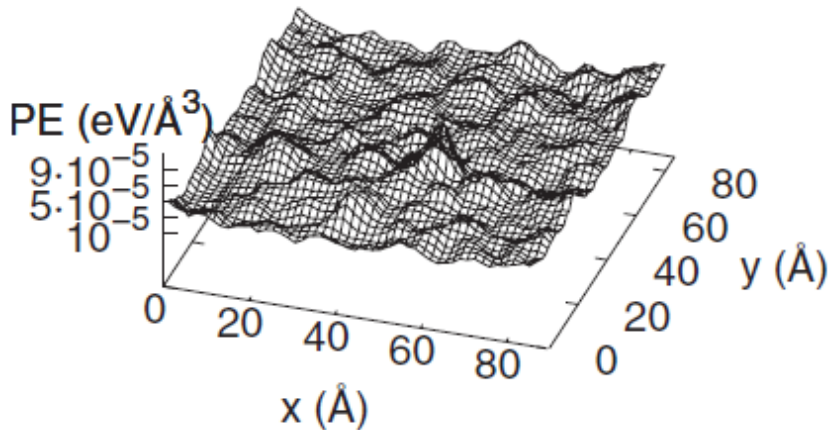


Figure 2.4: 2D projection of density of PE of amorphous silicon over the basins on xy plane at shear strain 1.6 % ($40 \text{ \AA} < z < 50 \text{ \AA}$) [Fusco et al., 2010].

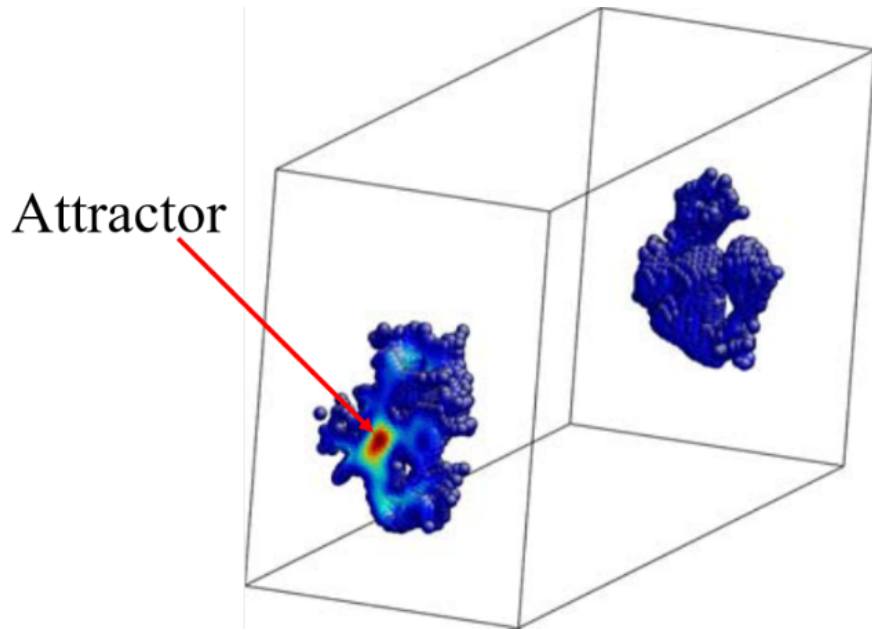


Figure 2.5: Map of plastic energy, $PE(\mathbf{r})$ surrounding a plastic event (the intensity of plastic energy from low to high) corresponding to the color from blue to red [Fusco et al., 2010].

The locations of plastic events are determined by the position of the attractors. The intensity of an individual plastic event is computed integrating the plastic energy density over its basin of attraction. In order to calculate the size of an attractor, we plot the radial distribution of the plastic energy around the attractors and fit it with an exponential function, $f(r) = a + b * e^{-\frac{r}{\lambda}}$, as shown in Figure 2.6. The damped exponential parameter λ is defined as the size of the attractor and therefore used to estimate the size of the plastic events. Thus, it is not necessary to totally display the detailed characteristics of $PE(r)$.

The input parameters used in this step are the number of atoms, the interatomic potential and the cut-off radius used to calculate the plastic intensity (PI) on a grid. The outputs are the results of plastic intensity and the position of each attractor at each step. At the same time, we can calculate the size of each attractor with the method mentioned before.

2.4.2 Selection of attractors

In fact, not all attractors are relevant. We set two criteria to select valid and important attractors. First, at low strain, due to numerical accuracy, there appears a large number

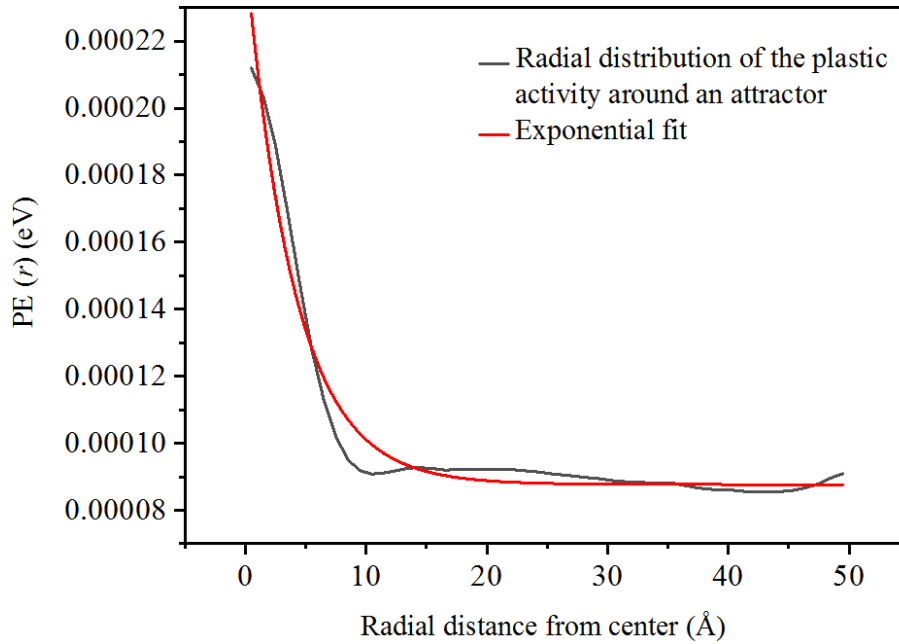


Figure 2.6: Radial distribution of plastic energy $PE(r)$ around the attractor and exponential fit curve [Albaret et al., 2016].

of attractors with low intensities even after reversible deformation, as shown in Figure 2.4. In order to get rid of them, we order the n_{att} attractors at a given strain as a function of their intensity so that the first in the list ($n=1$) has the highest intensity and the last one ($n=n_{att}$) the lowest one. If the plastic energy increment is more than 20 % between two successive attractors, n and $n+1$, i.e., $\frac{PI_n - PI_{n+1}}{PI_{n+1}} > 20\%$, then all attractors below $n+1$ are collected and the others are discarded. With this first criterion, we can select large plastic events at lower strain [Fusco et al., 2010]. On the other hand, at large strains, plastic events can bear larger PI even without large PI differences between events. In this case, the application of the first criterion would lead to discard significant plastic events. In order to avoid this, we set a threshold of minimum valid PI value. If the PI of attractors is larger than the threshold, they are selected. Here, this value is 1.5 eV to select 90 % valid plastic events. This arbitrary value of the energy threshold has been chosen in light of a parametric study, and leads to stable results with respect to the statistic of the plastic events, specifically yielding a good comparison between the behavior of the total plastic intensity integrated over all the basins and the total dissipated plastic energy calculated with the method explained in Section 2.4.1.

After having selected the valid plastic events with these two criteria, the cumulative number and cumulative energy of plastic events with strain can be computed.

At this stage, the main input parameters are two criteria for selecting valid attractors, and outputs are the selected attractors.

2.4.3 Rearrangement of plastic events

At this stage, plastic events are further reorganized, either grouped or killed, and input files for the following fitting procedure (see Section 2.4.4) are prepared. Here we define global parameters, like Poisson's ratio and the size of Eshelby's inclusion. The value of Poisson's ratio is 0.43, typical value in glass. The Eshelby's inclusion radius is taken as 12 Å, i.e., the simulated distance of the surrounding region at a distance from the center of Eshelby inclusion beyond 12 Å is defined as the part outside inclusion and can participate in displacement fitting. That means if the distance between two attractors is smaller than 12 Å, they can be merged. Otherwise, they are separate. The value of 12 Å for the Eshelby's inclusion radius corresponds to a "typical" size of plastic events, as calculated by the method illustrated in Section 2.4.1, and it has been chosen after testing several values of this parameter and searching for the one giving the best agreement between the simulated stress-strain curves and the ones obtained using the Eshelby's inclusion model (see Section 2.4.5). We notice that this value of 12 Å is larger than the typical size of the plastic events in amorphous Si, suggesting that the nature of the plastic events in these two amorphous systems is rather different. The input of this stage is the list of the selected relevant attractors obtained in the previous stage. All attractors at each step are ordered from the largest plastic energy intensity to the lowest. The output is the list of reorganized plastic events.

2.4.4 Atomic displacement fitting

At this stage, we fit the MD atomic displacements with the displacement field obtained from the Eshelby's inclusion model. For the sake of simplicity we consider that the inclusions are spherical. Additionally, homogeneous elastic constants are equal inside and outside the inclusions. Thus, a spherical inclusion with radius a , shear modulus G for

quasi-static shear deformation, and Poisson's ratio ν is embedded in an infinite homogeneous isotropic medium. The stress-free strain transformation tensor is ϵ_{ij}^T , and surface tension can be obtained by $p_{ij} = 2G(\epsilon_{ij}^T + \nu\delta_{ij}\frac{\epsilon_{kk}^T}{1-2\nu})$.

The fitting is based on displacement fitting. Thus, we need to calculate the displacement inside and outside inclusions from MD simulation and Eshelby's inclusion. Displacement u_i outside the inclusion and stress σ_{ij}^{out} follow [Bower, 2009].

$$u_i = \frac{a^3}{4(1-\nu)G} \left(\frac{2p_{ik}x_k + p_{kk}x_i}{15R^5} (3a^2 - 5R^2) + \frac{p_{jk}x_j x_k x_i}{R^7} (R^2 - a^2) + \frac{4(1-\nu)p_{ik}x_k}{3R^3} \right) \quad (2.35)$$

where R is the distance from the center of the inclusion.

$$\begin{aligned} \sigma_{ij}^{out} = & \frac{a^3}{2(1-\nu)R^3} \left(\frac{p_{ij}}{15} (10(1-2\nu) + 6\frac{a^2}{R^2}) + \frac{p_{ik}x_k x_j + p_{jk}x_k x_i}{R^2} (2\nu - 2\frac{a^2}{R^2}) \right. \\ & + \frac{\delta_{ij}p_{kk}}{15} (3\frac{a^2}{R^2} - 5(1-2\nu)) + \frac{\delta_{ij}p_{kl}x_k x_l}{R^2} ((1-2\nu) - \frac{a^2}{R^2}) \\ & \left. - \frac{x_i x_j p_{kl} x_k x_l}{R^4} \times (5 - 7\frac{a^2}{R^2}) + \frac{x_i x_j p_{kk}}{R^2} (1 - \frac{a^2}{R^2}) \right) \end{aligned} \quad (2.36)$$

Inside the inclusion, the strain ϵ_{ij}^{in} has the following relationship with stress-free transformation strain tensor $\epsilon_{ij}^{in} = S_{ijkl}\epsilon_{kl}^T$, where \bar{S} is the Eshelby tensor [Bower, 2009], and ϵ_{kl}^T is the transformation strain with the surrounding elastic matrix. Due to the presence of surface traction P_{ij} , the stress inside the inclusion is $\sigma_{ij}^{in} = C_{ijkl}\epsilon_{kl}^{in} - P_{ij} = C_{ijkl}(\epsilon_{kl}^{in} - \epsilon_{kl}^T)$. Since the displacement inside the inclusions is strongly dependent on the local atomic structure, only the displacements outside the inclusions are fitted using Eq. 2.35.

How does the fitting proceed? Input includes initial cell, initial configuration, the information of plastic events after selection (location, size, and the intensity of plastic energy), reverse configuration, numbers of atoms, Poisson's ratio, and Eshelby radius. From the atomistic simulation, the atomic displacement can be calculated by MD simulation. The atomic displacement d_{i,i_a} of atom i_a at i direction is computed by $d_{i,i_a} = r_{i,i_a}^{rev} - r_{i,i_a}^{curr}$. The total number of plastic events is defined as N_{sel} (selected plastic events). The center of plastic events is identified by $i_c(e)$, the index of the closest atom to the center of the inclusion. If atom i_a runs over the N^{out} atoms outside the inclusions, i.e., $|\mathbf{r}_{i_a}^{curr} - \mathbf{r}_{i_c(e)}^{curr}| > a(e)$, where $a(e)$ is the size of the plastic event, then we can set an objective function f to com-

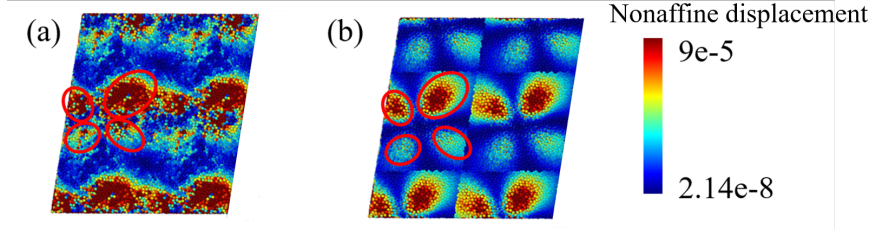


Figure 2.7: The distribution of nonaffine atomic displacements between two successive steps from MD simulation (a) and with Eshelby's inclusion model of $\text{Cu}_{64}\text{Zr}_{36}$ MG at strain 15 % during quasi-static shear deformation (b). Both images are replicated three times.

pare the atomic displacement computed by atomistic simulation and from Eshelby's inclusion. The distribution of atomic displacement from MD simulation and with Eshelby's inclusion is shown in Figure 2.7. The objective function f ,

$$f = \sum_{i_a=1}^{N^{out}} \sum_i \frac{1}{2} \left| d_{i,i_a} - \sum_{e=1}^{N_{sel}} u_i(\mathbf{r}_{i_a}^{curr} - \mathbf{r}_{i_c(e)}^{curr}, \overline{\overline{\epsilon^T}}(e)) \right|^2 \quad (2.37)$$

is minimized by damped MD, and then we can get the strain tensor, $\overline{\overline{\epsilon^T}}(e)$. It can also be used to estimate the precision of fitting.

2.4.5 Fitting of the stress-strain curve

At this stage we compare the stress-strain curve from the model with the MD results. From the previous results, we know the number and location of plastic events at each strain step. From Figure 2.3, we can see that the difference between $\{i\}^{curr}$ and $\{i-1\}^{rev}$ is the elastic part. So shear modulus at step i can be obtained by the ratio:

$$G(\gamma_i) = G_i = (\sigma_{xy}(\gamma_i) - \sigma_{xy}^{rev}(\gamma_{i-1})) / \delta\gamma_{xy} \quad (2.38)$$

We decompose strain increment, $\delta_i\epsilon_{xy}$ between step i and $i+1$, into an elastic and plastic part:

$$\delta_i\epsilon_{xy} = \delta_i\epsilon_{xy}^{el} + \delta_i\epsilon_{xy}^{pl} \quad (2.39)$$

We can get therefore the shear stress variation:

$$\delta_i \sigma_{xy} = 2G(\gamma_i) \delta_i \epsilon_{xy}^{el} = 2G(\gamma_i) (\delta_i \epsilon_{xy} - \delta_i \epsilon_{xy}^{pl}) = \delta_i \sigma_{xy}^* - \delta_i \sigma_{xy}^{pl} \quad (2.40)$$

where $\delta_i \epsilon_{xy} = \delta \gamma_{xy} / 2$ and $\delta_i \sigma_{xy}$ is obtained from the atomic simulation. $\delta_i \sigma_{xy}^*$ is the stress increment without plasticity, called elastically extrapolated stress. From configuration $\{i\}^{curr}$ to $\{i-1\}^{rev}$ through reverse deformation, in Figure 2.3, the difference between $\sigma_{xy}^{curr}(\gamma_i)$ and $\sigma_{xy}^{rev}(\gamma_{i-1})$ is the elastic component, thus, $\delta_i \sigma_{xy}^* = \sigma_{xy}^{curr}(\gamma_i) - \sigma_{xy}^{rev}(\gamma_{i-1})$. Then, the total elastically extrapolated stress, $\sigma_{xy}^*(\gamma_i)$ can be computed by $\sigma_{xy}^*(\gamma_i) = \sum_{j=0}^{i-1} \delta_j \sigma_{xy}^*$. The total shear stress $\sigma_{xy}(\gamma_i) = \sum_{j=0}^{i-1} \delta_j \sigma_{xy}$ is obtained from MD simulation, and plastic stress $\sigma_{xy}^{pl}(\gamma_i) = \sigma_{xy}^*(\gamma_i) - \sigma_{xy}(\gamma_i)$ can be obtained and compared to the plastic shear stress computed with Eshelby's inclusion introduced in the following.

According to the former Eq. 2.40, the stress can be considered to be based on the contribution of the stress field. Therefore, the plastic stress contribution $\delta \sigma_{xy}^{pl,esh}(e)$ of a single inclusion can be deduced to be:

$$\delta \sigma_{xy}^{pl,esh}(e) = -\frac{V_{esh}(e)}{V_{cell}} \sigma_{xy}^{in}(e) = \frac{2G(\gamma_i) V_{esh}(e)}{V_{cell}} (\epsilon_{xy}^T(e) - \epsilon_{xy}^{in}(e)) \quad (2.41)$$

where $\sigma_{xy}^{in}(e)$ is the shear stress inside inclusion, e , (σ_{ij}^{out} is the stress outside the inclusion, the angular sum over the terms of σ_{ij}^{out} vanishes). $V_{esh}(e)$ is the volume of the spherical inclusion e , and V_{cell} is the volume of the simulation cell. The Eshelby theory assumes that Eshelby's inclusion is in an infinite medium. However, in our computation we use a fixed cell, since at each strain γ_i the simulation box is first deformed in the forward direction and then comes back to its original shape after the reverse step. This condition implies a zero total strain on the cell. However, the total shear strain due to sum of the shear strains of all the inclusions in the cell is $\epsilon_{xy}^{esh,tot} = \sum_{e=1}^{N_{sel}} \frac{V_{esh}(e)}{V_{cell}} \epsilon_{xy}^{in}(e)$. Thus, a homogeneous correction, $-\epsilon_{xy}^{esh,tot}$, is required to preserve zero shear strain over the cell. Thus, when taking the boundary conditions into account, we can get:

$$\begin{aligned} \delta \sigma_{xy}^{pl,esh+bc}(e) &= \delta \sigma_{xy}^{pl,esh}(e) + 2G(\gamma_i) \epsilon_{xy}^{esh,tot} = \\ &= 2G(\gamma_i) \frac{V_{esh}(e)}{V_{cell}} (\epsilon_{xy}^T(e) - \epsilon_{xy}^{in}(e) + \epsilon_{xy}^{in}(e)) = \\ &= 2G(\gamma_i) \frac{V_{esh}(e)}{V_{cell}} \epsilon_{xy}^T(e) \end{aligned} \quad (2.42)$$

Finally, the shear stress from Eshelby's inclusion is

$$\sigma^{mod}(\gamma_i) = \sum_{j=0}^{i-1} \delta_j \sigma_{xy}^* - \sum_{j=0}^{i-1} \delta_j \sigma_{xy}^{pl,esh+bc} \quad (2.43)$$

The first term is the elastically extrapolated shear stress and the second term represents the sum of the plastic stress drops due to each Eshelby's inclusions (Eq. 2.42) and cumulated up to strain γ_i .

2.5 Conclusion

This chapter describes the methods used in this thesis, the molecular dynamics (MD) simulation, and the way quasi-static and dynamic tests are implemented. It also introduces the calculation of the parameters used to analyse the evolution of the microstructure. In addition, we presented the method for defining and analyzing plastic events, and the reconstruction of the stress-strain curve from MD simulation from the use of the description of the plastic event as Eshelby's inclusions.

Chapter 3

General analysis of the mechanical behavior of metallic glass from molecular dynamics simulation

Contents

3.1	Introduction	58
3.2	Effect of quenching rate	58
3.3	Effect of composition	66
3.4	Effect of strain rate	73
3.5	Effect of temperature	76
3.6	Discussion and conclusion	79

3.1 Introduction

As mentioned in Chapter 1 , the factors affecting the mechanical properties of metallic glasses (MGs) are various [Mukai et al., 2002, He et al., 2003, Shen et al., 2007]. In this chapter we study the influence of quenching rate, composition, strain rate, and temperature on the microstructure and the mechanical properties of MGs. Through molecular dynamics (MD) simulation, we analyze the effect of these factors and establish the link between microstructure and mechanical properties of MGs.

3.2 Effect of quenching rate

Quenching rate is a vital factor affecting the microstructure and mechanical properties of MGs [Wang et al., 2009, Yan et al., 2007, Huang et al., 2014]. Here, we study the microstructural characteristics of a binary MG, $Cu_{64}Zr_{36}$, with 32000 atoms under quenching rates from 10^{10} K/s to 10^{14} K/s. The global characteristics at each time step, like volume and temperature, can be obtained through MD simulation [Daw et al., 1993].

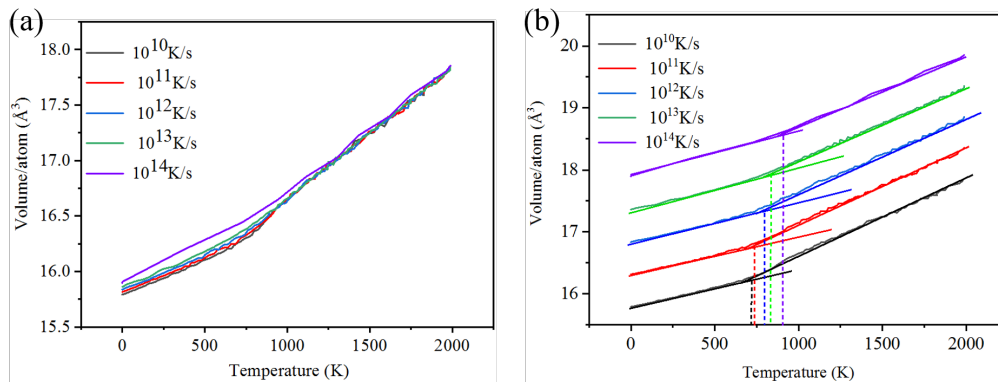


Figure 3.1: Volume as a function of temperature ($V-T$) of $Cu_{64}Zr_{36}$ MGs under different quenching rates (a) and the figure with shifted up curves (b).

Figure 3.1 shows the change of volume change of the sample as a function of temperature from the liquid state at 2000 K, to the solid glass state at very low temperatures. From Figure 3.1, it can be seen that below the inflection points, the volume per atom is larger for MGs with higher quenching rate at the same temperature, which shows that higher quenching rates can induce more free volume in MG system [Cheng and Ma, 2008]. The

inflection points correspond to the glass transition temperature T_g , which can be obtained by extrapolation and intersection of the two straight lines tangent to the curves for temperatures below and above this point. To make it clear, the curves have been shifted up in Figure 3.1 (b), and the values of T_g are shown in Table 3.1. We can conclude that T_g depends on the quenching rate, and is higher for higher quenching rates. In fact, higher quenching rates provide less time for atoms to relax, and the materials “freezes” earlier, leading to higher T_g [Debenedetti and Stillinger, 2001].

Table 3.1: T_g for $Cu_{64}Zr_{36}$ MGs with different quenching rates.

Quenching rate (K/s)	10^{10}	10^{11}	10^{12}	10^{13}	10^{14}
T_g (K)	690	730	783	821	897

Another indicator of the microstructure of the MG that we consider is the radial distribution function (RDF), already introduced in Chapter 2. The RDF for the final glass states after quenching with different quenching rates is presented in Figure 3.2. It clearly shows the typical features of an amorphous system, namely a highest sharp first peak, a splitting of the second peak, and a blunt third peak [Yue et al., 2018]. A subpeak before the first peak is observed in Figure 3.2. The existence of subpeak is also evidenced by both experiments [Mattern et al., 2008] and simulations [Yue et al., 2020, Feng et al., 2018]. A zoom in of the peaks displayed in Figure 3.3, shows that this subpeak appears at around 2.5 \AA , the highest one is at around 2.8 \AA , and the second peak is located at around 4.75 \AA . On the other hand, by inspection of the Cu-Cu partial RDF in Figure 3.4 we see that the first peak of Cu-Cu partial RDF in Figure 3.4 (a), is located at around 2.5 \AA , and the first peak on Cu-Zr partial RDF curve is at around 2.8 \AA . Thus, it can be speculated that the first peak of Cu-Cu partial RDF leads to the first subpeak of the total RDF. To confirm it, we plotted the RDF and partial RDF curves for another composition, $Cu_{36}Zr_{64}$, shown in Figure 3.5. Indeed, it can be observed that there are two subpeaks around the first peak, the left one is at 2.5 \AA , the right one is at 3.2 \AA , and the main peak is at 2.8 \AA , which respectively corresponds to the peak of Cu-Cu, Zr-Zr, and Cu-Zr partial RDF, respectively. Dziegielewski et al. also made the same conclusion in Cu-Zr MGs [Dziegielewski et al., 2020].

As a general remark, the effect of the quenching rate on the RDF is very slight and the

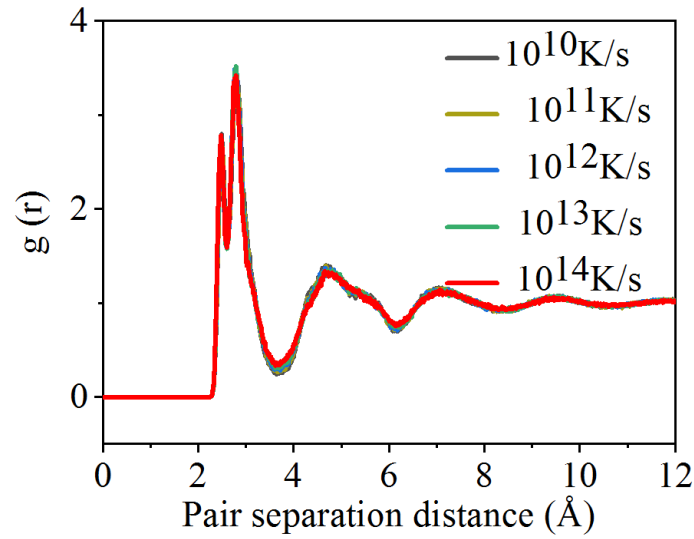


Figure 3.2: Radial distribution function (RDF) of $\text{Cu}_{64}\text{Zr}_{36}$ MG at 0.1 K under different quenching rates.

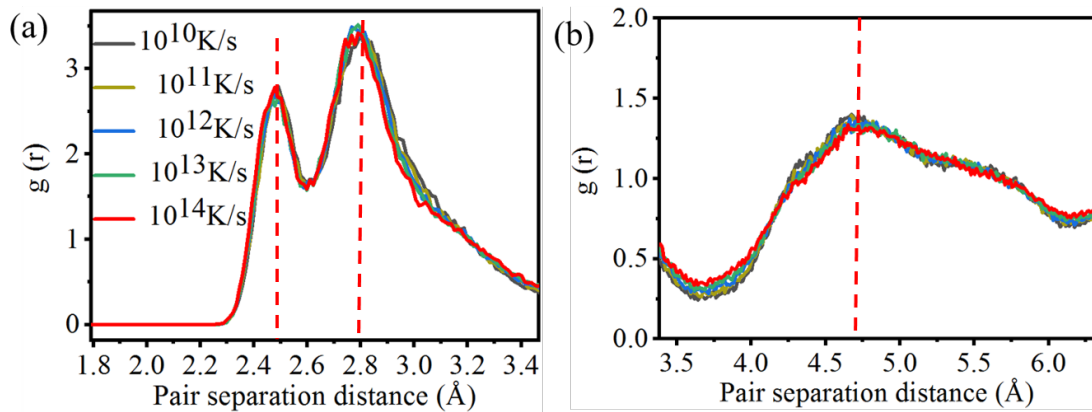


Figure 3.3: The first peak (a) and the second peak (b) on the RDF curves of $\text{Cu}_{64}\text{Zr}_{36}$ MG at 0.1 K under different quenching rates.

average interatomic distances are not affected, in agreement with previous results of the literature [Wang et al., 2009, Yue et al., 2018].

In order to study the effect of quenching rates on the mechanical behavior of MGs, we apply quasi-static shear deformation to MG system prepared with different quenching rates. The resulting shear stress-strain curves are shown in Figure 3.6. The shear modulus, measured as the slope of the linear part of the stress at very small strains, decreases when increasing the quenching rate, indicating that higher quenching rates result in easier deformation of MGs, as shown in Figure 3.7 (a). The yield stress, obtained as the

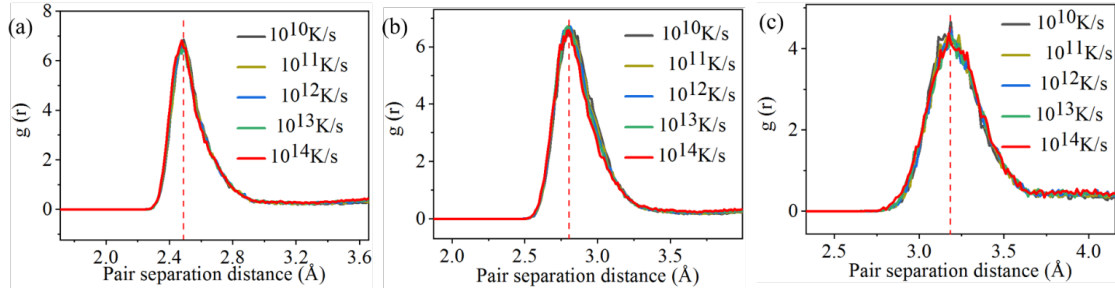


Figure 3.4: The first peaks on Cu-Cu partial RDF curves (a), the first peaks on Cu-Zr partial RDF curves (b), and the first peaks on Zr-Zr partial RDF curves (c) of $\text{Cu}_{64}\text{Zr}_{36}$ MG with different quenching rates.

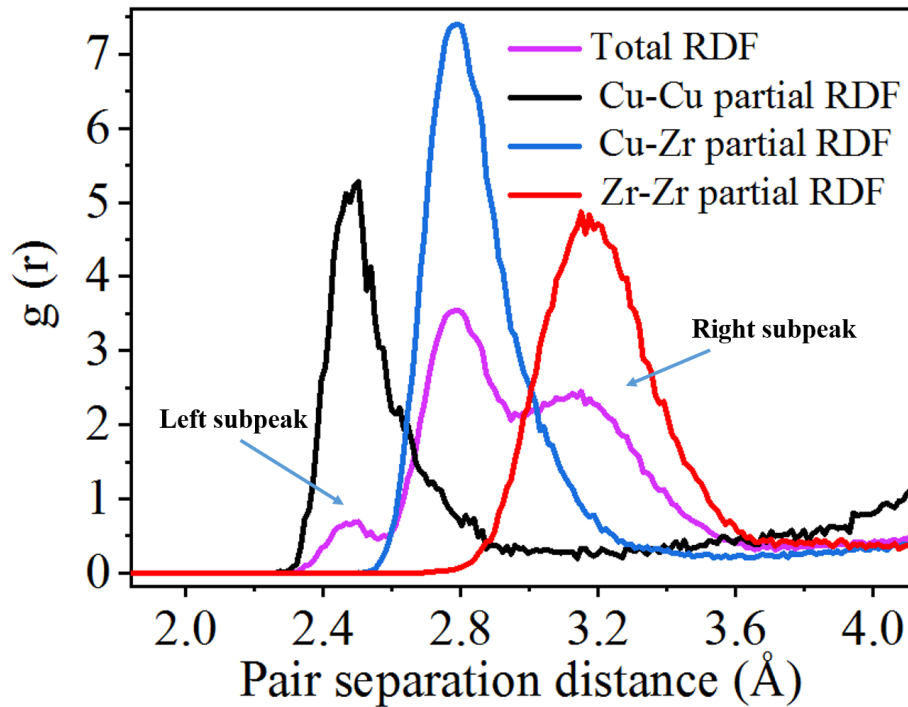


Figure 3.5: The first peak on RDF and partial RDF of $\text{Cu}_{36}\text{Zr}_{64}$ MG after quenching with a quenching rate of 10^{10} K/s at 0.1 K.

maximum of shear stress and the corresponding yield strain also decrease by increasing the quenching rate, as shown in Figure 3.7 (b). This means that the resistance to the initiation of flow decreases, and or in other words that it is easier to rejuvenate MG structure prepared with higher quenching rates [Cheng et al., 2008a, Shimizu et al., 2006]. We also calculate the flow stress as the average stress during the last 10 % strain. Figure 3.7 (c) shows that except the quenching rate of 10^{11} K/s, the flow stress slightly decreases with the quenching rate (even though the data are affected by large error bars due to the small signal to noise ratio, characteristic of the serrated flow in the stress-strain curves). This slight decreasing trend has been also observed with amorphous silicon by Fusco et al. [Fusco et al., 2010] and in $Cu_{46}Zr_{47}Al_7$ MG by Cheng et al. (in this study, the flow stress is the average stress of the last 60 % strain) [Cheng et al., 2008a].

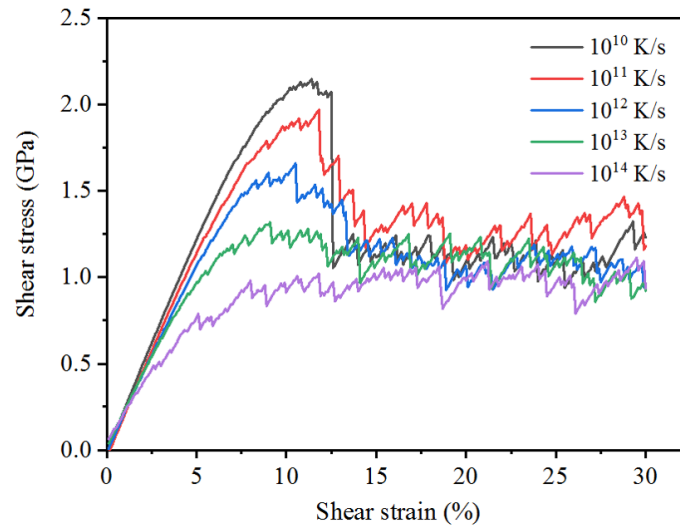


Figure 3.6: Shear stress-strain curves of $Cu_{64}Zr_{36}$ MG after quasi-static deformation with different quenching rates at 0.1 K.

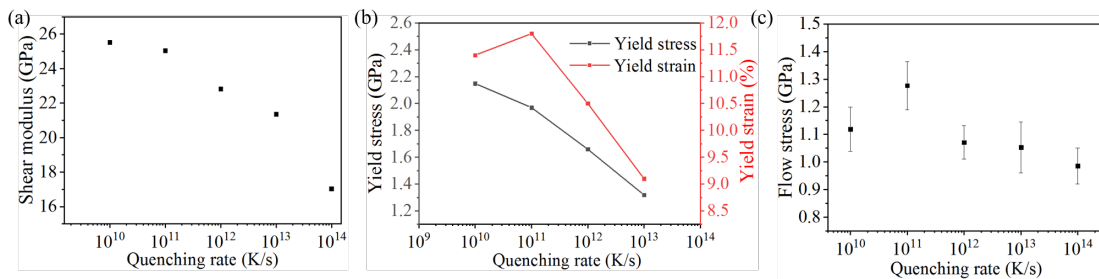


Figure 3.7: Shear modulus (a), yield stress and strain (b), and flow stress (c) for $Cu_{64}Zr_{36}$ prepared with different quenching rates.

The stress-strain curves in Figure 3.6 show that the stress drop occurs between 12 % and 15 % strain. Figure 3.8 at strain 12.3 % shows the map of the atoms with large atomic shear strains (larger than 60 % of the maximum atomic shear strain) in $Cu_{64}Zr_{36}$ MG prepared with a quenching rate 10^{10} K/s. Several localized shear transformations (STs) are visible. At strain 12.4 %, some STs develop as a shear band (SB), while, some diffuse out. According to Shimizu et al. [Shimizu et al., 2007], for Zr-based MGs, the length scale of SB should reach few ten nm. In our case, the length of the sample is 8 nm, thus, a band throughout the entire sample can be defined as an SB. Here we use a criterion to define the occurrence of an SB region: we consider all the atoms having an atomic shear strain larger than 60 % of the maximum local strain over the whole sample and we check whether this region percolates across the system. If it percolates we define it as an SB. In the case of Figure 3.8 we can identify 12.4 % as the strain where an SB forms.

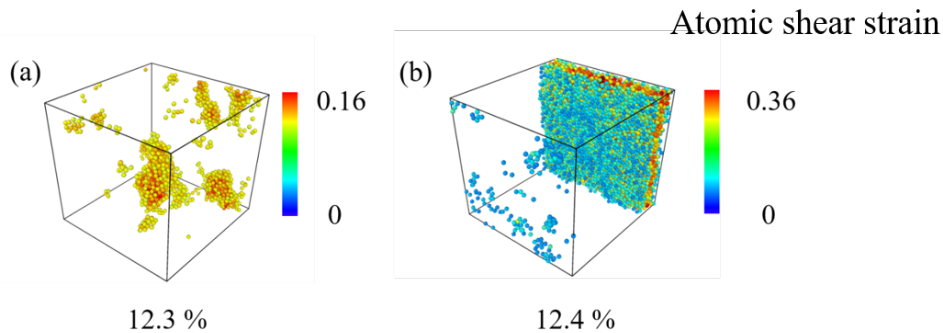


Figure 3.8: Map of atomic shear strain in $Cu_{64}Zr_{36}$ MG prepared with a quenching rate of 10^{10} K/s, sheared at 12.3 % strain (a) and 12.4 % (b), showing the atoms with shear strain larger than 60 % of the maximum atomic shear strain over the whole sample.

Moreover, 20 % strain being in the flow stress region, we plot the distribution of atomic shear strain at 12.3 %, 12.4 %, 12.5 %, 15 %, and 20 %, respectively, as shown in Figure 3.9. We compare the distribution of atomic shear strain for these different configurations for different quenching rates. At 12.4 % strain we can observe a complete shear band (SB) for the $Cu_{64}Zr_{36}$ MG with quenching rate of 10^{10} K/s, while for the other quenching rates, although localized STs exist, they do not form a complete band. At 20 % strain, for quenching rate from 10^{11} K/s to 10^{13} K/s, multiple SBs with different orientations are formed (in this system, both horizontal and vertical SBs can be formed with equal

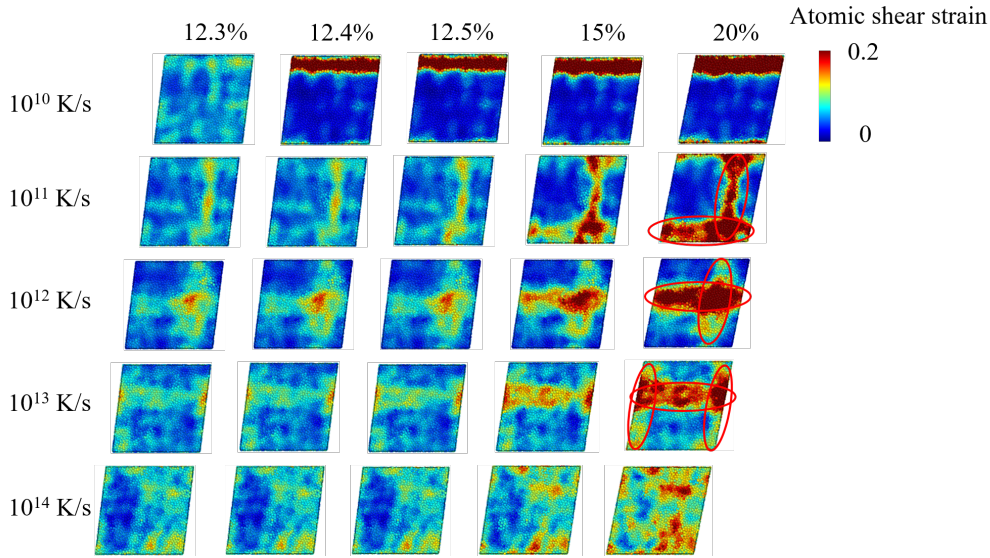


Figure 3.9: The atomic shear strain in $\text{Cu}_{64}\text{Zr}_{36}$ MG prepared with different quenching rates at different shear strains, at 0.1 K.

probability, with a slight preference for the horizontal orientation since we shear in xy plane). For quenching rate 10^{14} K/s, the distribution of atomic shear strain is gradually concentrated and localized with the strain increase. A clear SB is not visible even in the flow stress region. From these observations, it can be concluded that higher quenching rates lead to more homogeneous strain, in agreement with previous experimental [Huang et al., 2014, Shen et al., 2007] and simulation results [Yue et al., 2018, Zhong et al., 2016].

In order to relate the mechanical behavior to the MG microstructure, we plot in Figure 3.10 the fraction of FI (full icosahedra, FI), already introduced in Chapter 1, as a function of the shear strain of MG quenched under different quenching rates. It can be observed that a lower initial fraction of FI is obtained with higher quenching rates, which is consistent with previous results [Zemp et al., 2014]. With increasing shear strain, the fraction of FI decreases, proving their destruction during the deformation. Especially in the 12 %-15 % strain domain, the decrease of FI is considerable for the lowest quenching rate. Additionally, the fraction of FI in the SB region of $\text{Cu}_{64}\text{Zr}_{36}$ with shear strain is plotted in Figure 3.11. From strain 12.3 % to 12.4 %, the fraction of FI in SB region decreases significantly, from 2.23 % to 1.43 % whereas the total fraction of FI in the system decreases only by 0.01 % (as shown in Figure 3.10). In other words, the FI fraction decrease is mainly

due to their destruction in the SBs.

Through the former results, we can assess the effect of quenching rates on the microstructure and mechanical behavior of MGs: glasses are more relaxed when prepared with a lower quenching rate and they contain more FI, leading to stronger mechanical properties, i. e., larger yield strength and shear modulus, but poorer plasticity. Inversely, higher quenching rate leads to lower FI fraction of FI, related to more free volume, which can be beneficial for homogeneous deformation of the MGs [Zhong et al., 2016].

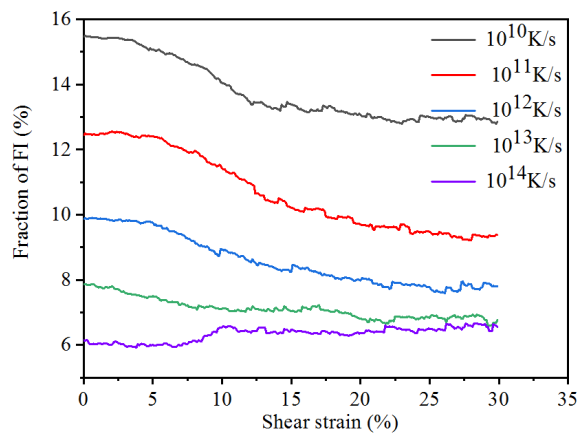


Figure 3.10: Fraction of FI of $\text{Cu}_{64}\text{Zr}_{36}$ prepared with different quenching rates as a function of shear strain at 0.1 K.

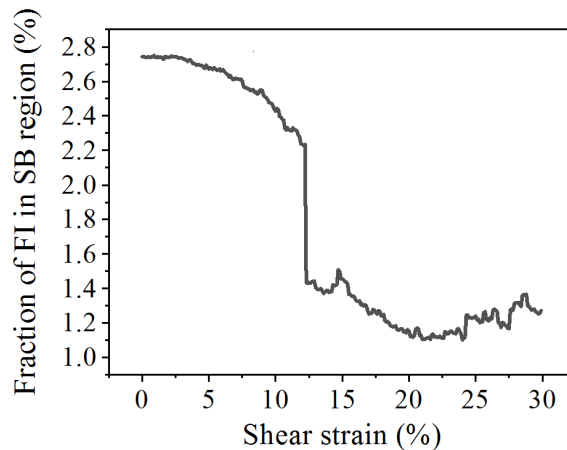


Figure 3.11: Fraction of FI in SB region of $\text{Cu}_{64}\text{Zr}_{36}$ prepared with the quenching rate 10^{10} K/s as a function of shear strain.

3.3 Effect of composition

Many researchers have focused on the effect of composition on the mechanical properties of MGs [Liu et al., 2007, Chen et al., 2008, Kim et al., 2009]. In this section, to study this question, we selected three different compositions of binary Cu-Zr MG system, i.e., $\text{Cu}_{64}\text{Zr}_{36}$, $\text{Cu}_{50}\text{Zr}_{50}$, and $\text{Cu}_{36}\text{Zr}_{64}$, quenched at a quenching rate of 10^{11} K/s. Figure 3.12 shows the volume change as a function of the temperature. The volume of the system increases with the ratio of the Zr element, which is expected since the equilibrium distance of Zr atom is larger than that of the Cu atom [Wang et al., 2009]. T_g of the MG increases with the Cu content which agrees with the result of Mattern et al [Mattern et al., 2008].

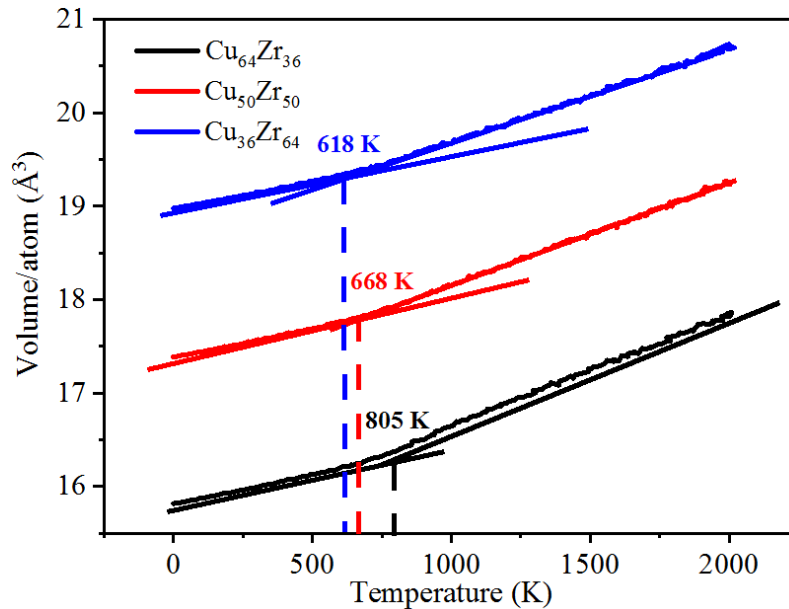


Figure 3.12: Volume as a function of the temperature for the three different compositions quenched with a quenching rate of 10^{11} K/s. Dotted lines are to determine the glass transition temperature.

The total radial distribution functions (RDF) of the three compositions of binary Zr-Cu MGs quenched down to 0.1 K at 10^{11} K/s are shown in Figure 3.13 (a). The enlarged first peak is shown in Figure 3.13 (b). For the total RDF, the composition has a very small effect on the position of the main peak at 2.8 \AA . This result is consistent with the work Wang et al. [Wang and Wong, 2012] and Mattern et al [Mattern et al., 2008]. Figure 3.13 (b) shows detail of this peak which is actually made of three peaks. As discussed earlier

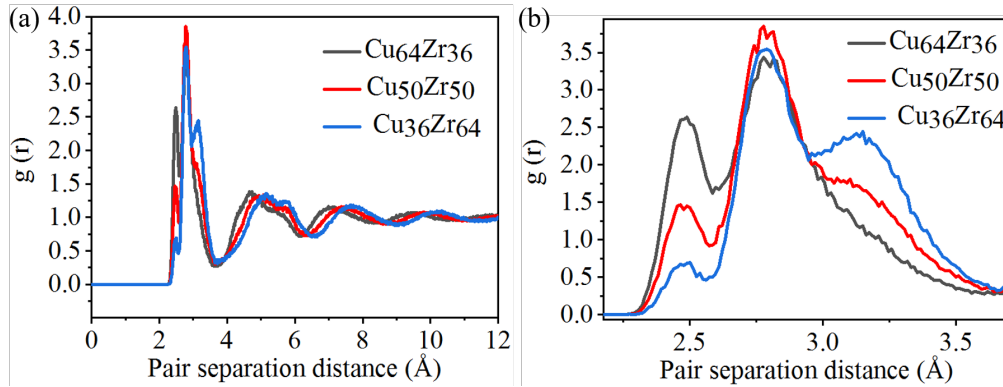


Figure 3.13: The total radial distribution function (RDF) for three compositions of binary Cu-Zr MGs quenched at 0.1 K at a quenching rate of 10^{11} K/s (a) and the magnification of the first peak (b).

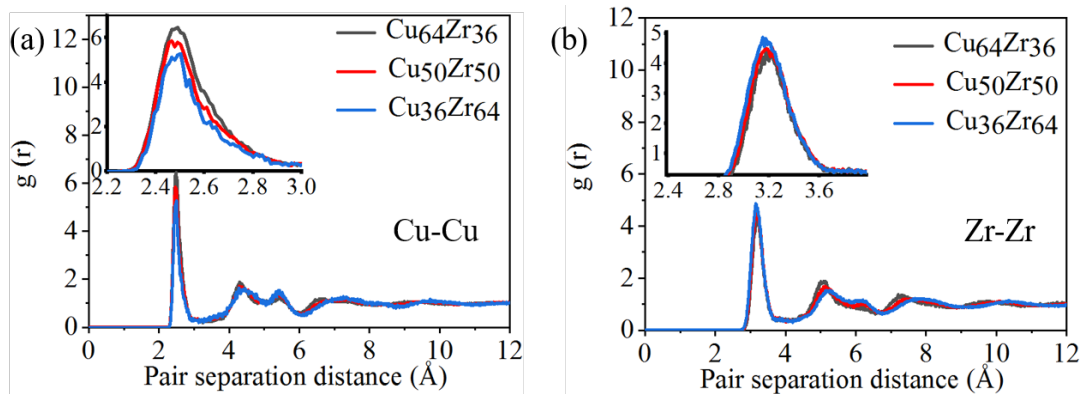


Figure 3.14: Cu-Cu (a) and Zr-Zr (b) partial radial distribution function (PRDF) for three compositions of binary Zr-Cu MGs quenched at 0.1 K at a quenching rate of 10^{11} K/s. The insets in the Figures show a magnification of the first peaks.

in Section 3.1, the peak at 2.5 Å is attributed to Cu-Cu pair, the right subpeak (at 3.2 Å) to the Zr-Zr pair, and the main peak (at 2.8 Å) is attributed to the Zr-Cu pair. This explains the fact that the amplitude of the left subpeak increases with the increase of the Cu ratio, while the amplitude of the right subpeak increases with the increase of the Zr ratio, This analysis is confirmed by the plot of the partial Cu-Cu and Zr-Zr RDF (cf. Figure 3.14 (a) and (b)). Figure 3.15 focuses on the second peak. This one is shifted towards larger distance when the Zr content increases, which is expected because of the larger atomic radius of Zr. In addition, we observe a splitting of the second peak for all the three compositions. This splitting can be related to the connection of icosahedra resulting into

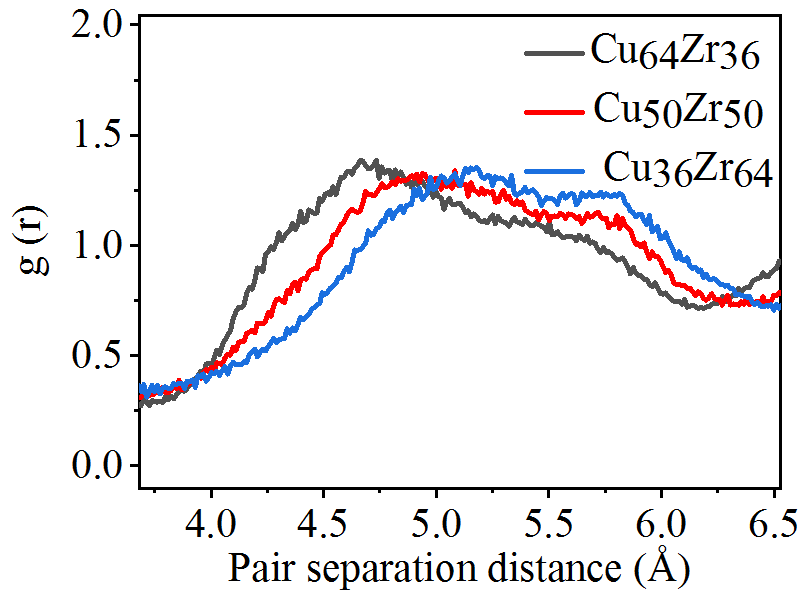


Figure 3.15: The insets in the figures show a magnification of the first peaks. Magnification of the second peaks of the total RDF curves shown in Figure 3.13 (a).

two different characteristic interatomic distances typical of medium-range order (MRO), as suggested by a previous study [Liang et al., 2014].

After the comparison of microstructure, we study the influence of the composition on the mechanical properties of the MGs by applying to them the same quasi-static shear deformation, as shown in Figure 3.16. The shear modulus, yield stress, yield strain and flow stress are reported in Figure 3.17. From Figure 3.17 (a), (b), and (d), we can conclude that the shear modulus and yield stress increase with the Cu ratio (in spite of a large error bar). The yield strain of $Cu_{64}Zr_{36}$, $Cu_{50}Zr_{50}$, and $Cu_{36}Zr_{64}$ is 12.4 %, 10.6 % and 10.7 %, respectively. These results are in agreement with the simulation work of by Cheng et al [Cheng et al., 2008a], which also showed that the resistance to flow increases with the Cu ratio. Indeed, our results also suggest a slight increase of the flow stress with the Cu content. After normalizing the stress by the shear modulus (cf. Figure 3.18), it can be seen that the difference between the stress-strain curves of these three compositions is slight and that the yield stress is nearly proportional to the shear modulus, again in agreement with Cheng et al [Cheng et al., 2008a].

In order to compare the distribution of shear transformations (STs) of three compositions, we plot the map of atomic shear strain. The strains selected are the yield strains of the

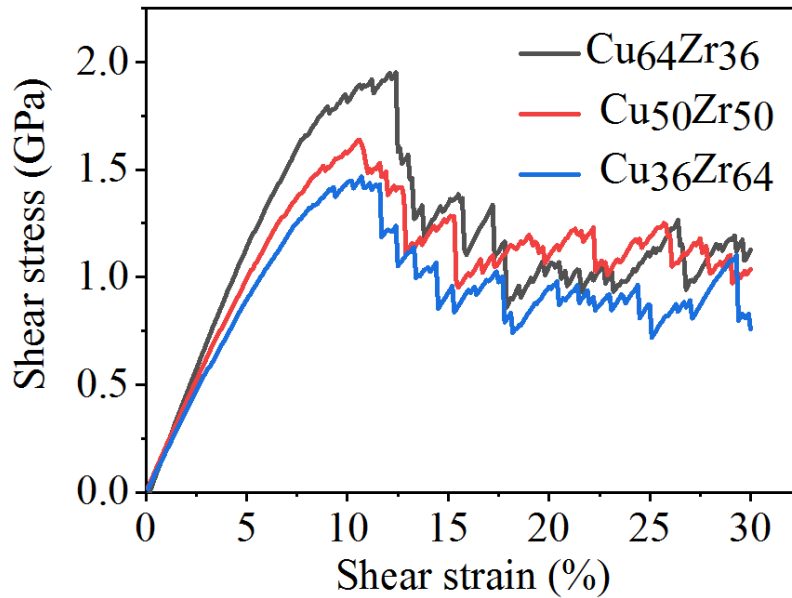


Figure 3.16: Shear stress-strain curves of three compositions quenched at 0.1 K after quasi-static deformation at a quenching rate of 10^{11} K/s.

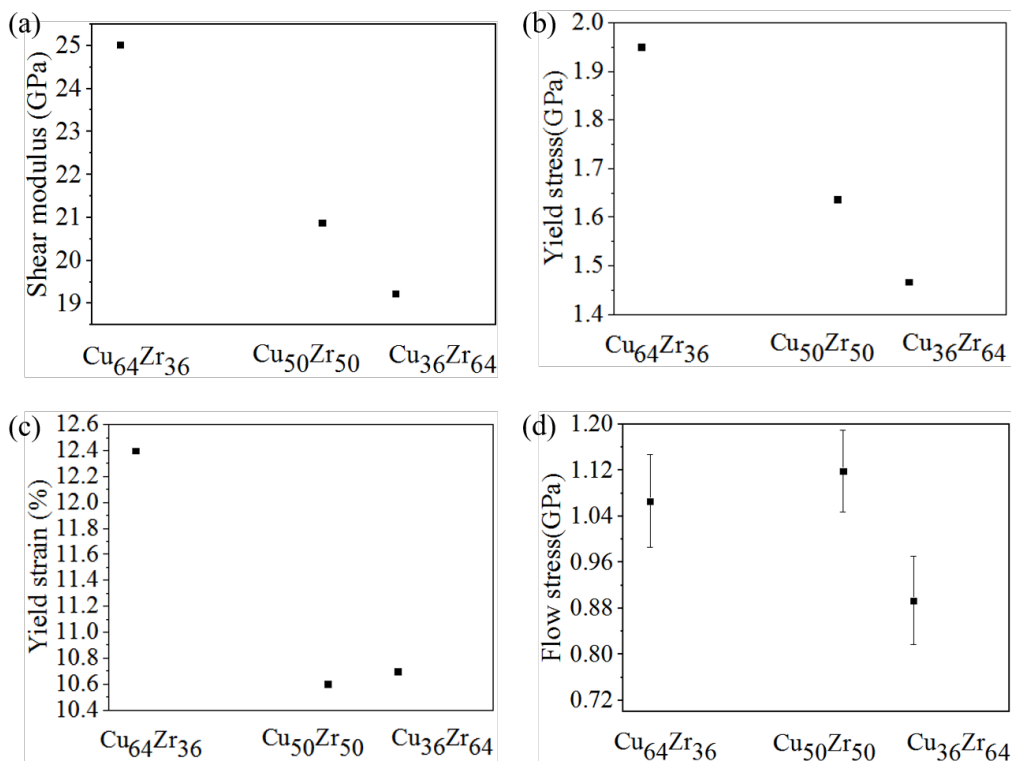


Figure 3.17: Shear modulus (a), yield stress (b), yield strain (c) and flow stress (d) of three compositions quenched at 0.1 K at a quenching rate of 10^{11} K/s.

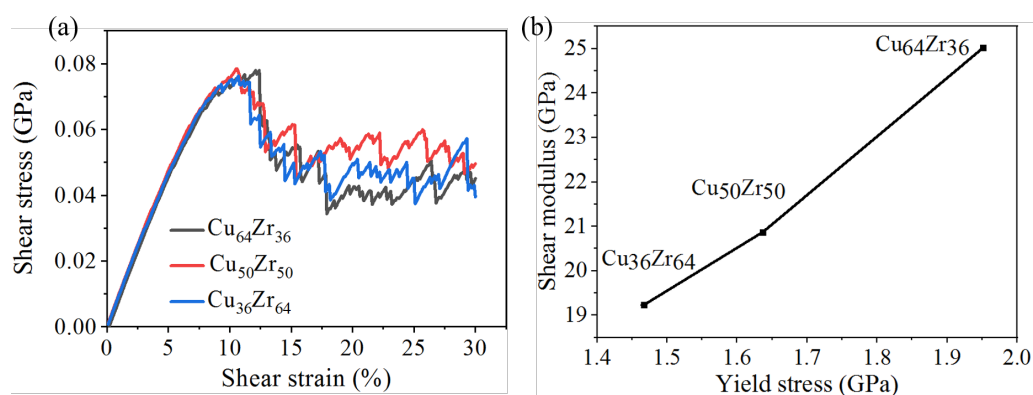


Figure 3.18: Normalized shear stress-strain curves by the shear modulus (a) and shear modulus vs. yield stress (b) of three compositions quenched at 0.1 K at a quenching rate of 10^{11} K/s.

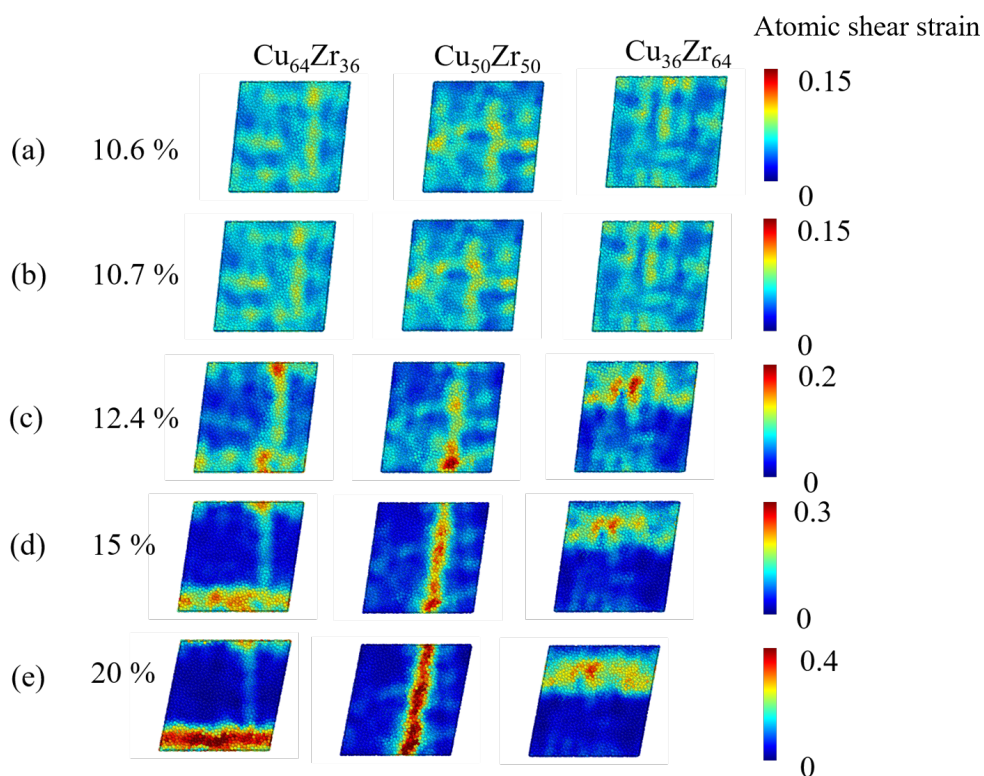


Figure 3.19: Map of atomic shear strain for the three compositions at strain 10.6 % (a), 10.7 % (b), 12.4 % (c), 15 % (d), and 20 % (e) at 0.1 K for a quenching rate of 10^{11} K/s.

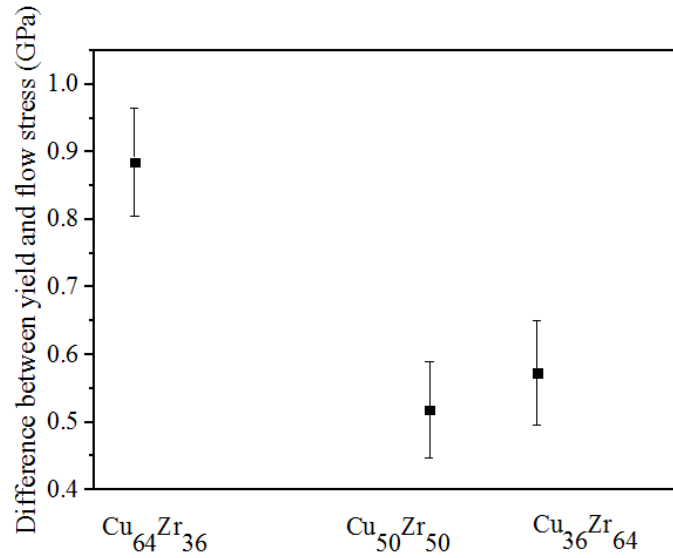


Figure 3.20: Comparison of difference between yield and flow stress of three compositions.

three compositions, a strain after the stress drops and a strain during the flow stress region, as shown in Figure 3.19. The difference at smaller strains is slight, while after the stress drops, STs are more localized for $\text{Cu}_{64}\text{Zr}_{36}$. In fact, we observe the formation of SBs for all the compositions, but the SB is much less pronounced for $\text{Cu}_{36}\text{Zr}_{64}$. This observation is supported by the computation of the difference between the yield and flow stresses, which indicates the propensity to strain localization. As shown in Figure 3.20, this quantity is larger for $\text{Cu}_{64}\text{Zr}_{36}$ in agreement with more localized STs after the stress drop.

Additionally, it is found that the initial fraction of $\langle 0,0,12,0 \rangle$ icosahedra (full icosahedra, FI) is higher for the MG with a higher Cu fraction, as shown in Figure 3.21. The reason is that most FI are Cu-centered clusters. As shown in Figure 3.21 (a), e.g., for $\text{Cu}_{64}\text{Zr}_{36}$, the fraction of FI is around 12.5 %. As shown in Figure 3.22 (a), among these FI, the fraction of Cu-centered icosahedra is 12.4 %, and that of Zr-centered icosahedra is nearly zero indicating that the smaller size atom tends to be the central atom of the icosahedra structure [Liang et al., 2014, Miracle et al., 2003]. In addition, the fraction of FI decreases with strain, especially during the stress drop on the stress-strain curves. We calculated the decrease of FI, $\Delta FI = \frac{FI_{\text{initial}} - FI_{\text{final}}}{FI_{\text{initial}}}$, reported in Table 3.2. ΔFI is smaller for $\text{Cu}_{36}\text{Zr}_{64}$, which corresponds to a smaller drop on the stress-strain curve and less localized deformation.

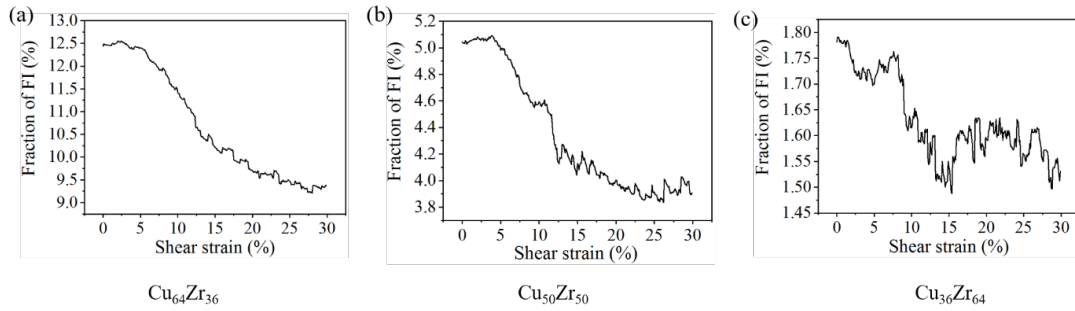


Figure 3.21: Comparison of fraction of FI with shear strain for the three compositions.

Table 3.2: Relative decrease of FI after a quasi-static shear deformation (up to flow) for the three compositions.

Composition	$\text{Cu}_{64}\text{Zr}_{36}$	$\text{Cu}_{50}\text{Zr}_{50}$	$\text{Cu}_{36}\text{Zr}_{64}$
ΔFI (%)	20.07	23.84	15.79

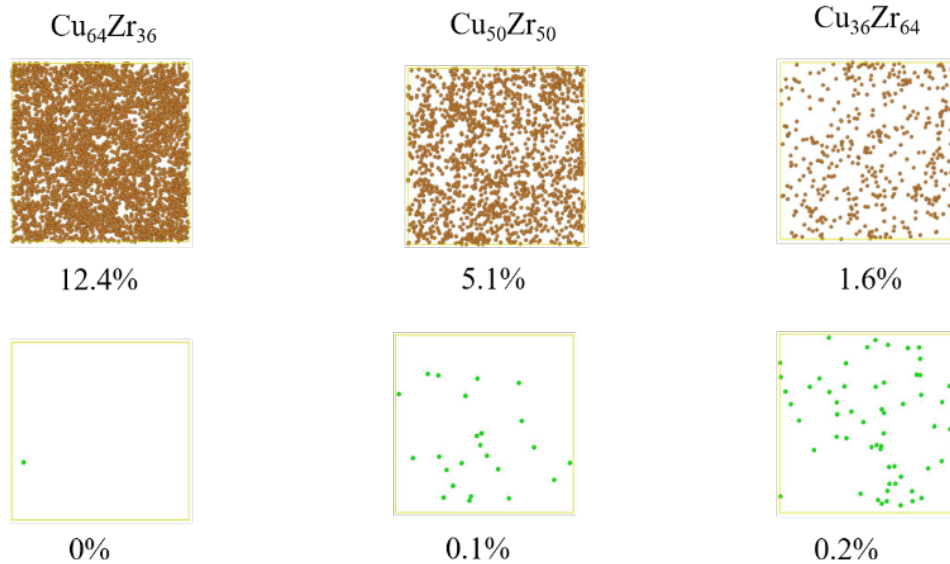


Figure 3.22: Map of central atoms of FI for the three compositions (brown balls are Cu atoms, and green balls are Zr atoms).

3.4 Effect of strain rate

The effect of strain rate on the mechanical properties of MGs has been widely studied [Mukai et al., 2002, Zhang et al., 2007, Ma et al., 2009, Li et al., 2017]. Different effects of strain rate on the mechanical behavior were observed, depending on the material investigated, on the strain rate range and on the temperature. The deformations are implemented at 0.1 K, far from the glass transition temperature. On the same $\text{Cu}_{64}\text{Zr}_{36}$ MG system, we apply dynamic shear deformation (cf. Chapter 2) with different strain rates, 10^7 s^{-1} , 10^8 s^{-1} , and 10^9 s^{-1} , to study the effect of strain rate on the mechanical properties of MGs. All of these systems possess the same initial microstructure and they have been obtained with a quenching rate of 10^{11} K/s . Figure 3.23 presents the obtained stress-strain curves and Figure 3.24 the deduced shear moduli, and yield and flow stresses. They show that the influence of the strain rate on these three parameters is roughly insignificant. The distributions of atomic shear strain of the $\text{Cu}_{64}\text{Zr}_{36}$ MG systems at different strain rates

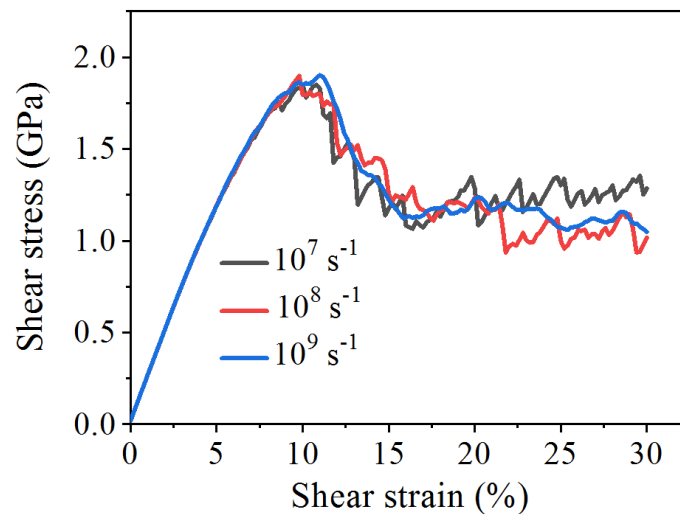


Figure 3.23: *Shear stress-strain curves with different strain rates for of $\text{Cu}_{64}\text{Zr}_{36}$ MG prepared with a 10^{11} K/s quenching rate at 0.1 K.*

and at 10 %, 12.5 %, 15 %, and 20 % strain are presented in Figure 3.25. Indeed, the maps do not evidence pronounced differences in the local strain distribution. These results are consistent with the simulation work of Sepulveda-Macias et al. [Sepulveda-Macias et al., 2018], which also show that at very low temperatures, the effect of strain rate on

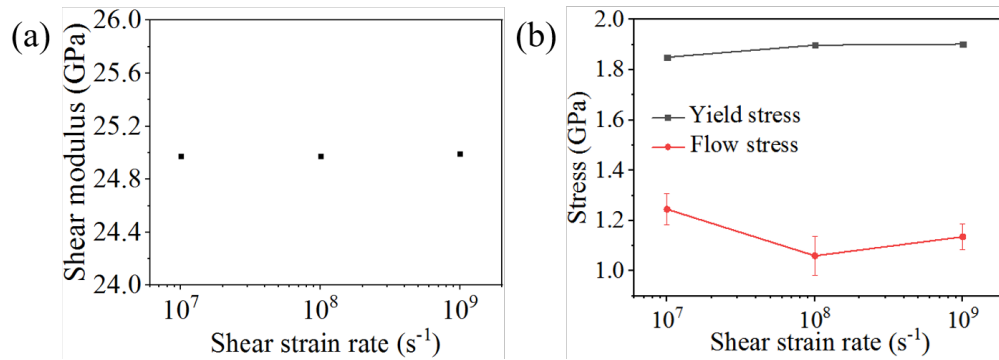


Figure 3.24: Shear modulus (a) and yield and flow stress (b) as a function of the different strain rates for $\text{Cu}_{64}\text{Zr}_{36}$ MG quenched at 0.1 K, at a quenching rate of 10^{11} K/s.

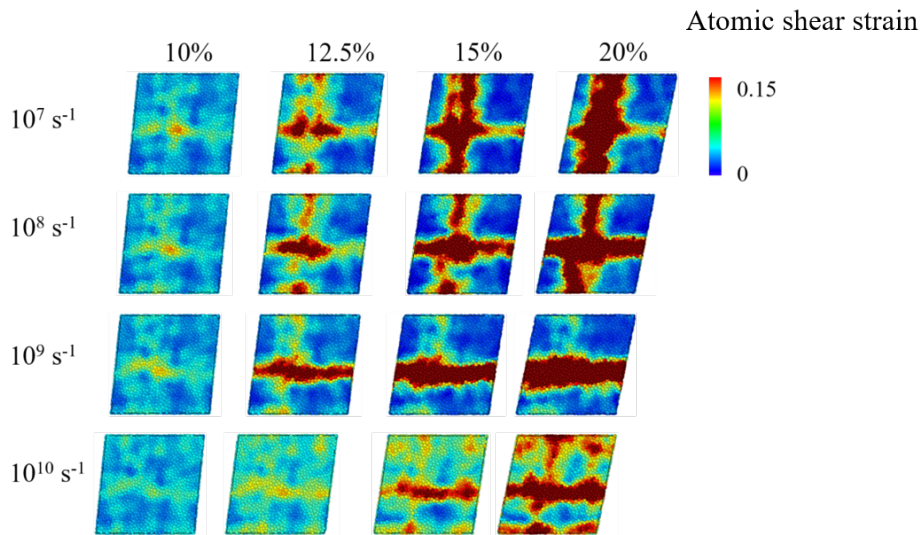


Figure 3.25: Distribution of atomic shear strain of $\text{Cu}_{64}\text{Zr}_{36}$ MGs with different strain rates, at strain 10 %, 12.5 %, 15 %, and 20 %, at 0.1 K.

the mechanical properties of MGs is small (although the shear modulus and yield stress are slightly increased when the strain rate of MGs is largely increased). It also showed that the effect of strain rate on MGs becomes more pronounced when the temperature is increased. Therefore, we also studied the stress-strain curves of $\text{Cu}_{64}\text{Zr}_{36}$ MG at 50 K and 200 K after deformation at different strain rates (to do so, $\text{Cu}_{64}\text{Zr}_{36}$ MG was quenched from the liquid state with a quenching rate of 10^{11} K/s down to the temperature of the shear test, i.e. 50 K or 200 K).

Results are shown in Figure 3.26. Indeed, the influence of the strain rate on the yield stress slightly increases when the temperature increases. The yield strain is relatively

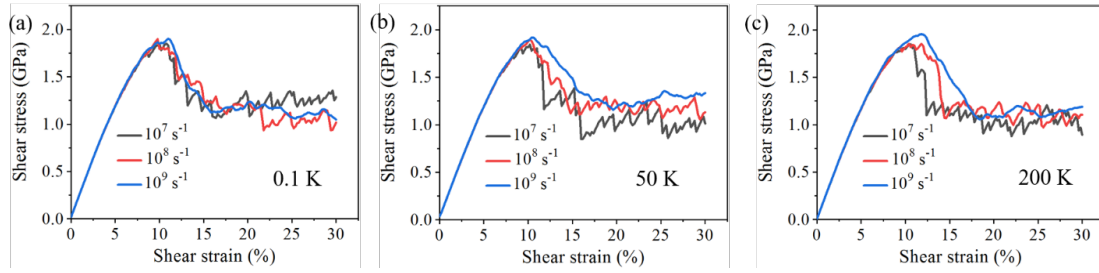


Figure 3.26: Comparison of stress-strain curves of $Cu_{64}Zr_{36}$ MGs sheared with different strain rates, at three different temperatures: (a) 0.1 K, (b) 50 K, (c) 200 K.

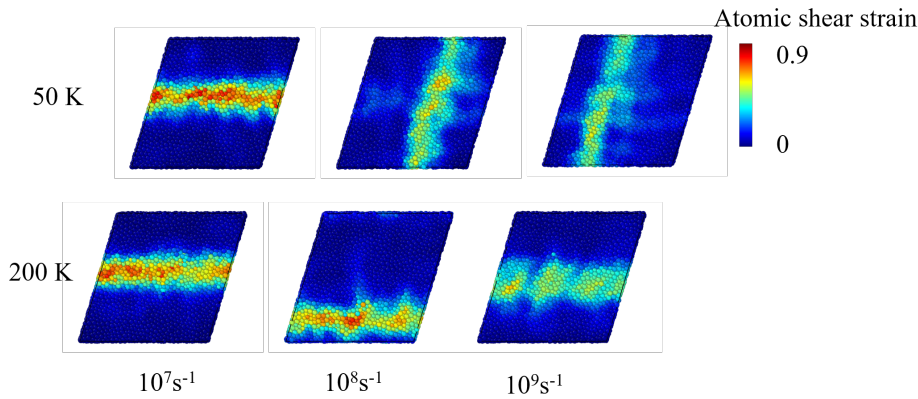


Figure 3.27: Map of atomic shear strain of $Cu_{64}Zr_{36}$ MG at strain 30 % with strain rate of $10^7 s^{-1}$, $10^8 s^{-1}$ and $10^9 s^{-1}$ when the temperature is 50 K and 200 K.

larger at higher strain rate. We have plotted in Figure 3.27, the atomic shear strain maps of $Cu_{64}Zr_{36}$ MG when deformed at 30 % strain, at different strain rates for temperatures 50 K and 200 K. It is clear that at higher temperatures, the STs of $Cu_{64}Zr_{36}$ MG are more homogeneous when the strain rate is higher, in agreement with the conclusion of Sepulveda-Macias and Albe et al [Sepulveda-Macias et al., 2018, Albe et al., 2013]. In conclusion, no significant effect of the strain rate has been found at very low temperatures. This could also be due to the high strain rate used in MD. Similar conclusions were obtained in previous studies [Zhong et al., 2016, Egami et al., 2013]. Preliminary results suggest that for temperatures closer to T_g , the influence of the strain rate on the mechanical properties is more significant [Fu et al., 2007].

3.5 Effect of temperature

We have more deeply studied the influence of temperature. $\text{Cu}_{64}\text{Zr}_{36}$ MG was quenched from the liquid state with a quenching rate of 10^{11} K/s down to 0.1 K, 50 K, 200 K, or 500 K, and then sheared. Figure 3.28 to Figure 3.31 show a higher amplitude of the first peak and of the second peak of the total and partial radial distribution function (RDF) when the MG is quenched at a lower temperature [Wen et al., 2021], indicating a higher local density.

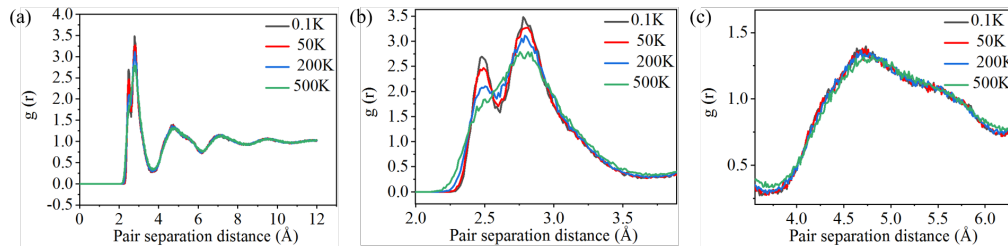


Figure 3.28: The total RDF of $\text{Cu}_{64}\text{Zr}_{36}$ MG at different temperatures for quenching rate 10^{11} K/s (a), magnified first peak (b) and magnified second peak (c).

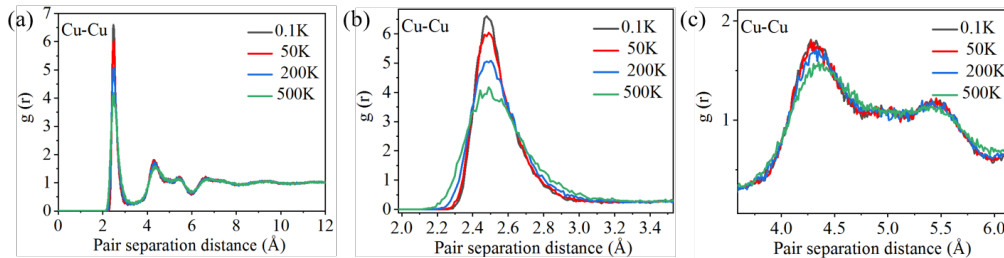


Figure 3.29: The Cu-Cu PRDF of $\text{Cu}_{64}\text{Zr}_{36}$ MG at different temperatures for quenching rate 10^{11} K/s (a), magnified first peak (b) and magnified second peak (c).

Stress-strain curves obtained at strain rate 10^8 s^{-1} and different temperatures are shown in Figure 3.32. We have compared two types of deformation: shear and tensile (Figure 3.32 (a) and 3.32 (b) respectively). Deduced shear modulus and Young's modulus are plotted in Figure 3.33. They both strongly decrease with the increase in temperature. In addition the yield stress, yield strain and flow stress decrease with the temperature, as classically observed in previous experimental or simulation study [Wang et al., 2015, Sepulveda-Macias et al., 2018].

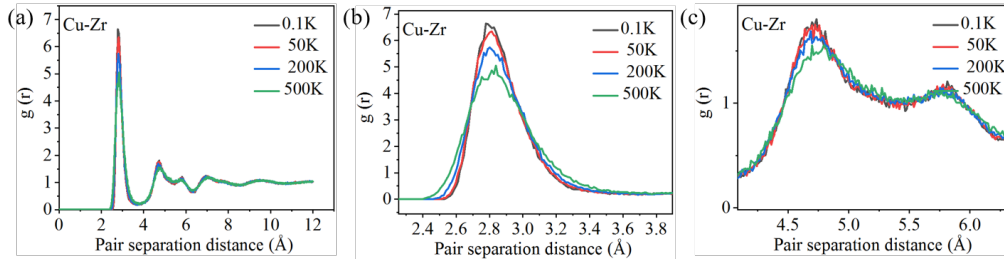


Figure 3.30: The Cu-Zr PRDF of $\text{Cu}_{64}\text{Zr}_{36}$ MG at different temperatures for quenching rate 10^{11} K/s (a), magnified first peak (b) and magnified second peak (c).

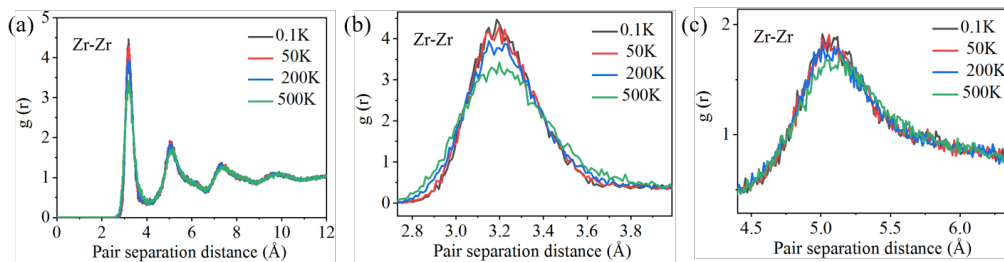


Figure 3.31: The Zr-Zr PRDF of $\text{Cu}_{64}\text{Zr}_{36}$ MG at different temperatures for quenching rate 10^{11} K/s (a), magnified first peak (b) and magnified second peak (c).

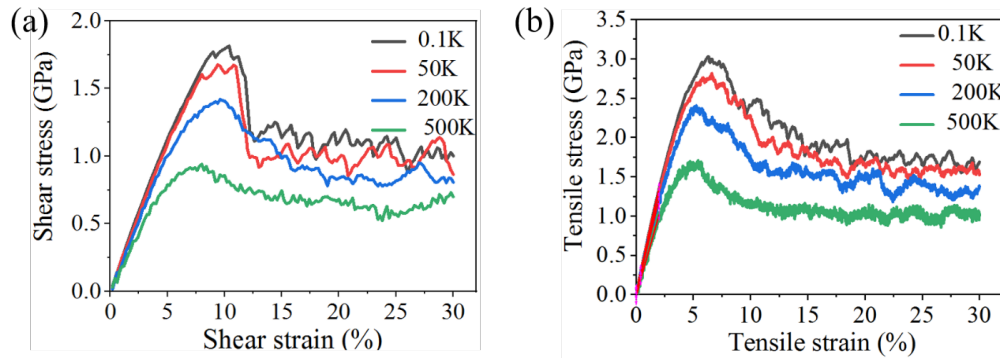


Figure 3.32: Shear stress-strain curves (a) and tensile stress-strain curves (b) of $\text{Cu}_{64}\text{Zr}_{36}$ MG at different temperatures and strain rate 10^8 s $^{-1}$.

We have plotted the distribution of atomic shear strain at 12 % strain (after the yield peak) in Figure 3.34. It shows that higher temperature leads to more homogeneous deformation, in agreement with the experimental results [Yu et al., 2011]. Figure 3.35 presents the evolution of the FI fraction as a function of the shear strain, for test at different temperatures. The initial value of the FI fraction decreases with the increase in the temperature, in a non linear way (the decrease accelerates). The final FI fraction, after shearing also

decreases, though less strongly. Thus the decrease is sharper with the smallest temperature. This is consistent with a less homogeneous deformation, as shown by the map of atomic shear strain in Figure 3.34.

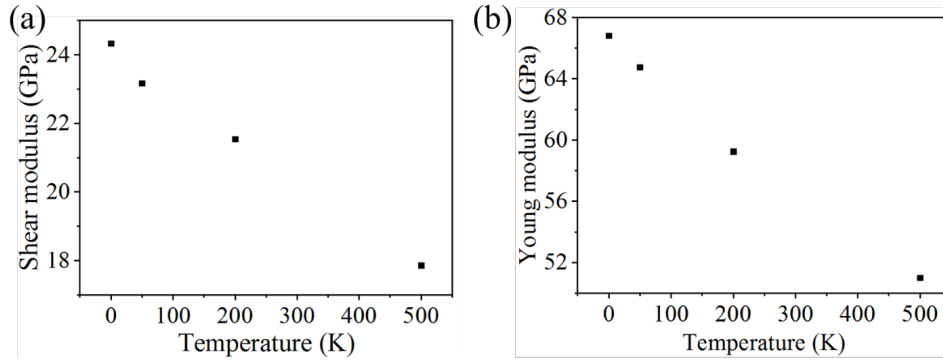


Figure 3.33: Shear modulus (a) and Young's modulus (b) of $\text{Cu}_{64}\text{Zr}_{36}$ MG deduced from shear tests and tensile tests at different temperatures and strain rate 10^8 s^{-1} .

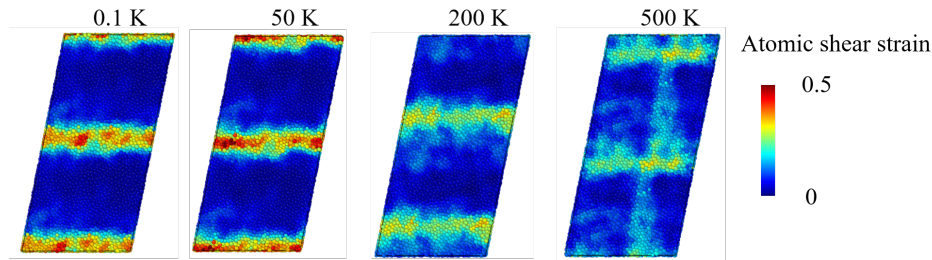


Figure 3.34: Distribution of atomic shear strain at 20 % strain at different temperatures and strain rate 10^8 s^{-1} (scale doubled in the y -direction to better visualize).

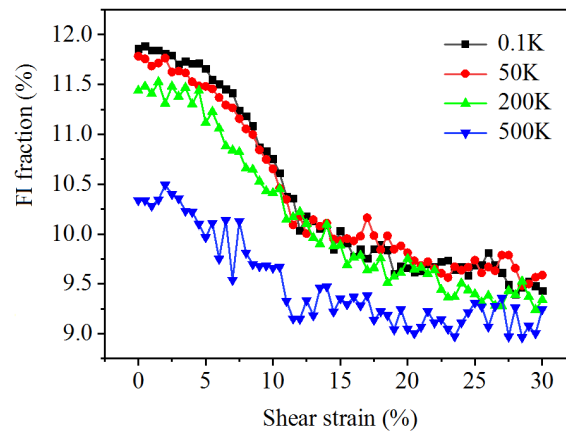


Figure 3.35: Fraction of FI of $\text{Cu}_{64}\text{Zr}_{36}$ MG quenched at different temperatures and sheared at the same temperature with a 10^8 s^{-1} shear strain rate.

3.6 Discussion and conclusion

By studying the effects of quenching rate, compositions, strain rate and temperature on the mechanical properties of Cu-Zr MGs, we obtain the following conclusions.

The glass transition temperature of MGs depends on the quenching rate, and for higher quenching rate, higher T_g is obtained. However, the quenching rate has a slight effect on the nearest-neighbor distance of the atoms. Regarding its effect on the mechanical properties of MGs, we find that the shear modulus and yield stress decrease with increasing quenching rate and the plastic deformation is less localized. With lower quenching rates, more full icosahedra (FI) are formed, which is consistent with less free volume, and more FI are destroyed during the deformation.

Regarding the composition effect, T_g increases with the increase in Cu ratio in Cu-Zr MGs. In addition, since the central atoms of FI are mostly Cu atoms, when the Cu ratio increases, fraction of FI in the Cu-Zr MG increases substantially, and thus STs are more localized at the same strain.

Concerning the strain rate effect, it is not significant at very low temperature we studied, and needs temperature close to the glass transition to be significant. In that case, plastic deformation is found more uniform for MGs with higher strain rates.

Regarding the temperature influence, the atomic packing density of the MGs is higher and the SRO is more pronounced when temperature is decreased. When deformed, MGs have higher shear and Young's moduli and higher yield stresses at lower temperature, which is correlated to a larger fraction of FI and more localized plastic deformation.

In conclusion, a higher quenching rate, lower Cu ratio, and higher temperature all result in a more uniform deformation of Cu-Zr MGs. This is also the case for higher strain rates.

Chapter 4

Analysis of the plastic events at the origin of the macroscopic plasticity

Contents

4.1	Introduction	82
4.2	Effect of quenching rates and compositions on plastic events	82
4.2.1	Effect of quenching rates on plastic events	82
4.2.2	Influence of the metallic glass composition	89
4.3	Prospect for tensile tests	94
4.4	Discussion and conclusion	99

4.1 Introduction

Chapter 3 described the effects of quenching rate, composition, strain rate and temperature on the mechanical properties of metallic glasses (MGs), through the analysis of stress-strain curves, atomic shear strain, etc. In order to understand the effect of these factors on the observed macroscopic plasticity, in this chapter, we characterize and discuss in detail the plasticity of the system by identifying the plastic events occurring at a given strain, in terms of number, plastic intensity and size. From this parametric study we can propose a strategy how to improve the ductility of MGs.

4.2 Effect of quenching rates and compositions on plastic events

This section takes focuses on the results of Section 3.1 and 3.2.

4.2.1 Effect of quenching rates on plastic events

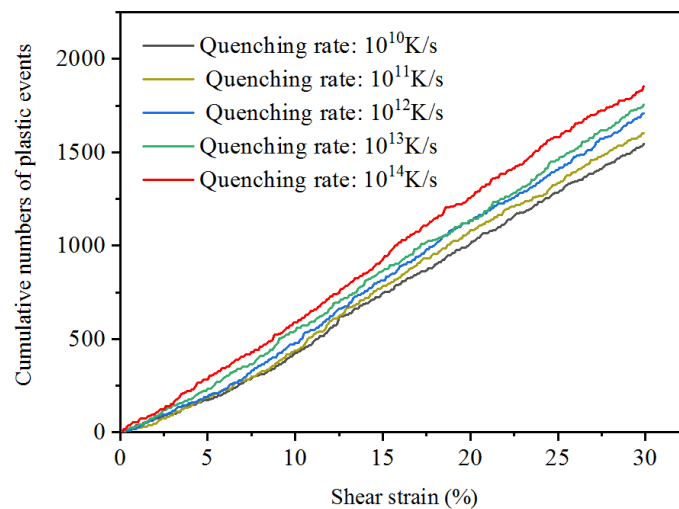


Figure 4.1: Cumulative numbers of plastic events with strain for $Cu_{64}Zr_{36}$ MG with different quenching rates.

As described in Section 3.1, $Cu_{64}Zr_{36}$ MG is quenched from liquid state to 0.1 K with different quenching rates from 10^{10} K/s to 10^{14} K/s, and then experiences quasi-static shear deformation to 30 % strain. The variation of the cumulative number and plastic

intensity (calculation detailed in Section 2.4.1) of plastic events with strain are shown in Figure 4.1 and 4.2.

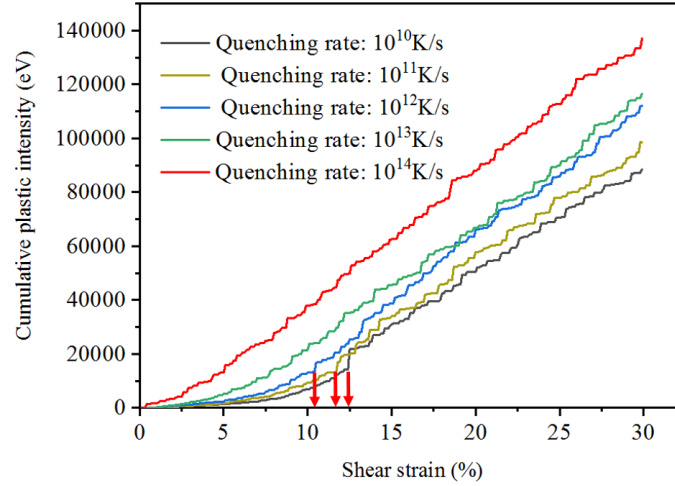


Figure 4.2: Cumulative plastic intensity of plastic events for different quenching rates.

From Figure 4.2, it is clear that there are three small jumps in the curves for the three quenching rates from 10^{10} K/s to 10^{12} K/s. The locations of these three small jumps, which indicate a sudden release of elastic energy, correspond to that of the yielding points in their stress-strain curves (orange ellipses in Figure 4.3). That means that there is a pronounced increase in the plastic intensity of the plastic events when the yielding stress is reached. At higher shear strains, in the flow stress region of the stress-strain curve, the increase in the cumulative plastic intensity is linear (cf. Figure 4.2).

To go further, the number, the plastic intensity and the average size of the plastic events of $Cu_{64}Zr_{36}$ MG with different quenching rates, are plotted in Figure 4.4 to 4.6. It can be observed that we can detect plastic events with appreciable sizes even at the beginning of the deformation since we use a quasi-static deformation procedure. In the quasi-static approach, we cannot track the time evolution of plastic events. The curves are scattered, indicating a large variation from one strain step to another. However, in spite of this, a curve trend can be guessed for all the data. To make the comparison evident, we smoothed the curves with Savitzky-Golay (SG) filter method (described in the appendix) and selected two quenching rates, 10^{10} K/s (the lowest one) and 10^{14} K/s (the highest one).

4.2. EFFECT OF QUENCHING RATES AND COMPOSITIONS ON PLASTIC EVENTS

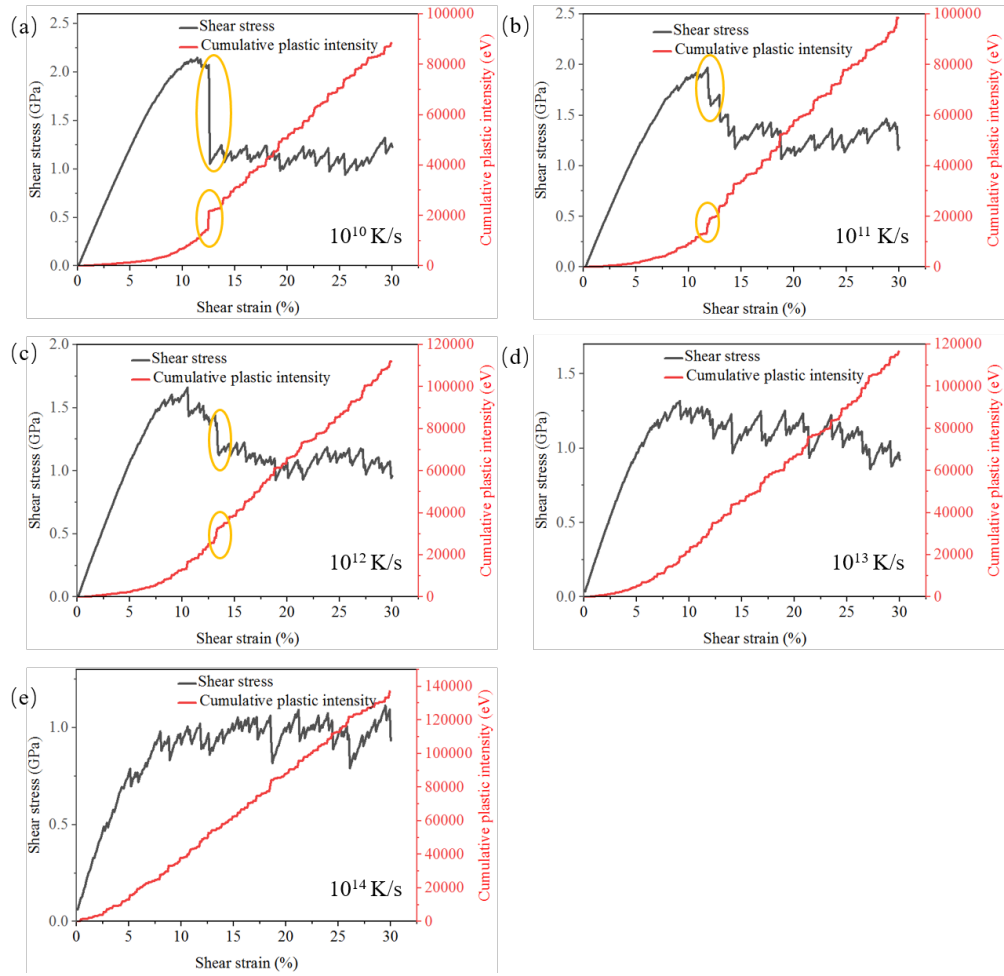


Figure 4.3: Shear stress and cumulative plastic intensity of plastic events for different quenching rates.

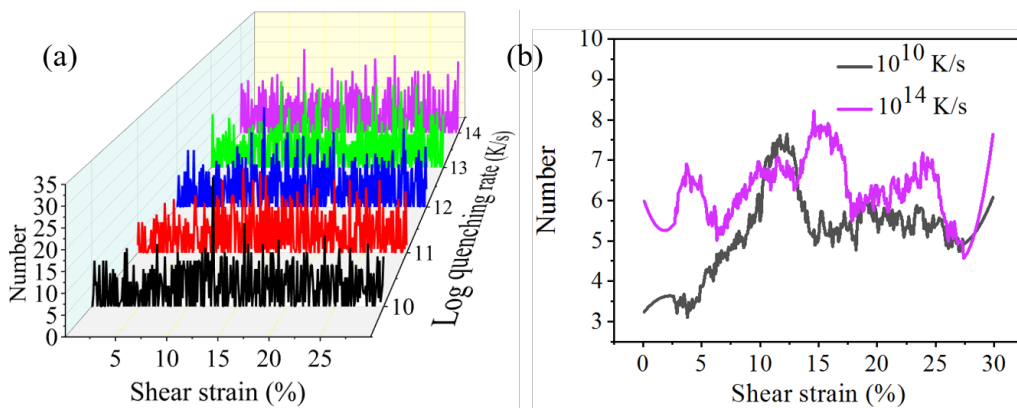


Figure 4.4: Numbers of plastic events as a function of the shear strain, for $\text{Cu}_{64}\text{Zr}_{36}$ MG, for different quenching rates (a) and comparison between quenching rates 10^{10} K/s and 10^{14} K/s after smoothing with SG filter method (b).

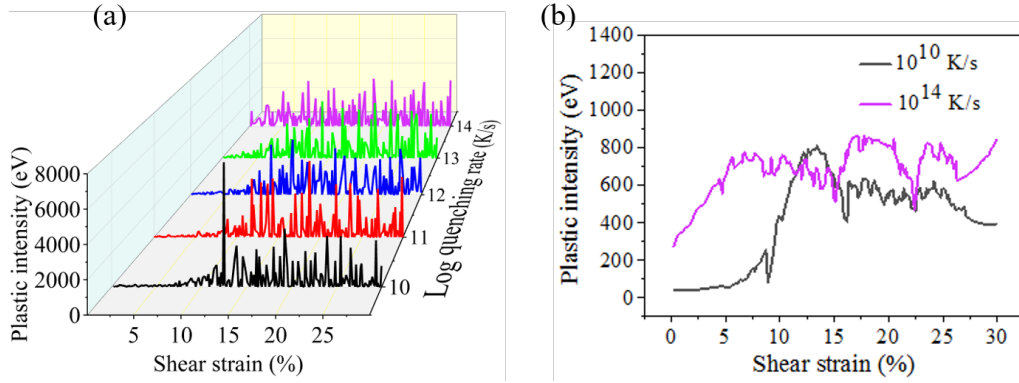


Figure 4.5: Plastic intensity of plastic events for the different quenching rates (a) and comparison between quenching rates 10^{10} K/s and 10^{14} K/s after smoothing with SG filter method (b).

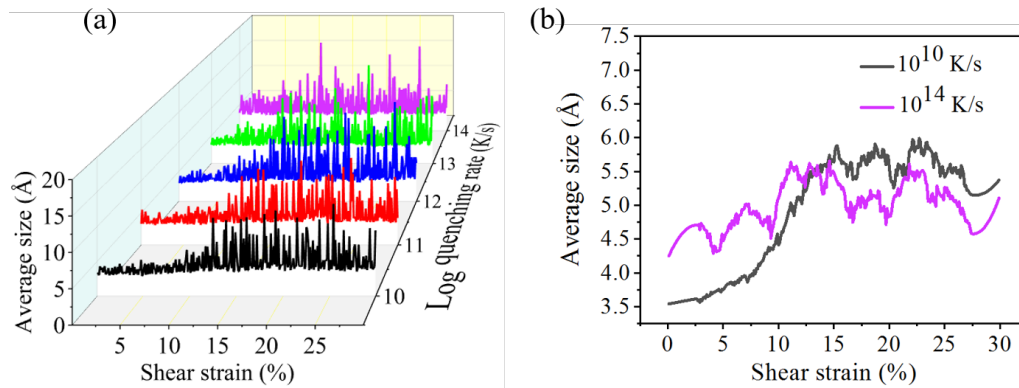


Figure 4.6: Comparison of the average size of plastic events with strain for different quenching rates (a) and comparison between quenching rates 10^{10} K/s and 10^{14} K/s after smoothing with SG filter method (b).

4.2. EFFECT OF QUENCHING RATES AND COMPOSITIONS ON PLASTIC EVENTS

Even in the elastic region, plastic events can be observed, however their number, intensity and average size are small, especially for the lowest quenching rate. Said differently, more numerous and larger plastic events with more plastic intensity are activated at the beginning of the deformation with the highest quenching rate. With the shear strain increasing, all of the parameters increase up to the yield point, more rapidly for the slowest quenching rate. At higher strain, number, size and plastic intensity, still scattered, seem to stabilize around a value which is roughly the same for all the quenching rates, except maybe for the size parameter: this one is slightly larger for the slowest quenching rate. This may be related to the easier formation of shear bands for this system (Figure 3.8).

Then we have calculated the orientation of the plastic events, defined as $\varphi_{xy,max}$. It is deduced from the components of the strain tensor of the equivalent Eshelby's inclusion in the shear plane xOy, following the expression:

$$\tan(2\varphi_{xy,max}) = \frac{\varepsilon_{yy}^T - \varepsilon_{xx}^T}{2\varepsilon_{xy}^T} \quad (4.1)$$

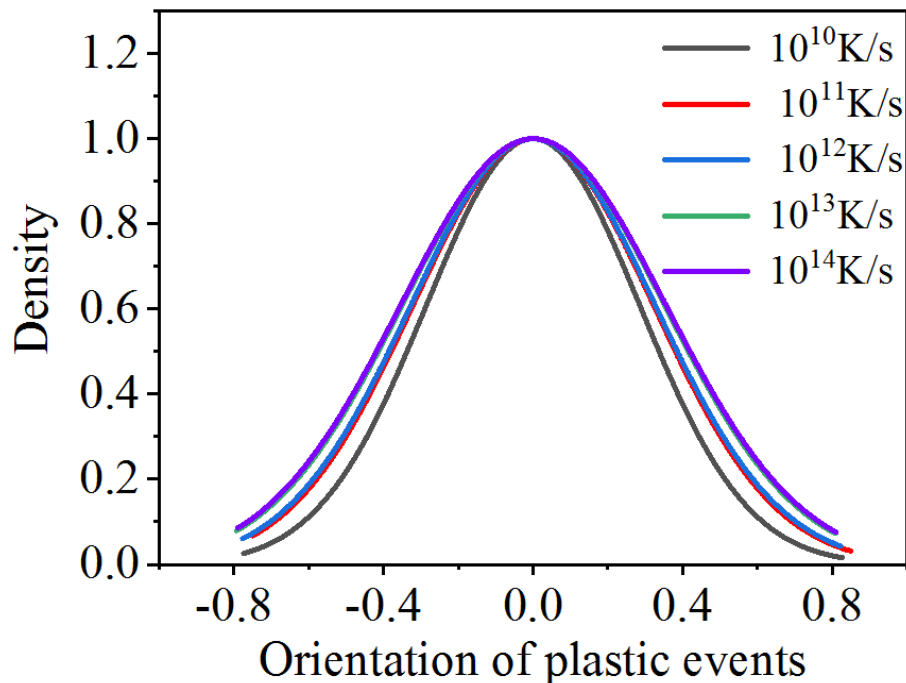


Figure 4.7: Distribution of orientation of all the plastic events occurring during a shear test of $\text{Cu}_{64}\text{Zr}_{36}$ MG quenched at different quenching rates.

Table 4.1: *Sigma value of the distribution of orientation of shear transformation with different quenching rates.*

Quenching rate (K/s)	10^{10}	10^{11}	10^{12}	10^{13}	10^{14}
Sigma	0.286265	0.322852	0.327813	0.352292	0.356218

As expected, the distribution of $\varphi_{xy,max}$ is symmetric, as shown in Figure 4.7, with a maximum at 0, which corresponds to the shearing direction. It can be fitted by a Gaussian law, plotted in Figure 4.7. The sigma values used for fitting are reported in Table 4.1. They increase as the quenching rate increases, indicating that for high quenching rates, the plastic event directions are more diverse. This may be related to plastic events more uniformly distributed. To check this assumption, Figure 4.8 reports the comparison between the orientation distributions of plastic events which occur before, and after a shear band (SB) formation for the lowest quenching rate. The very small difference between the two curves actually suggests that the plastic events orientation distribution cannot be easily correlated to SB formation. Further work would be necessary to clarify this point.

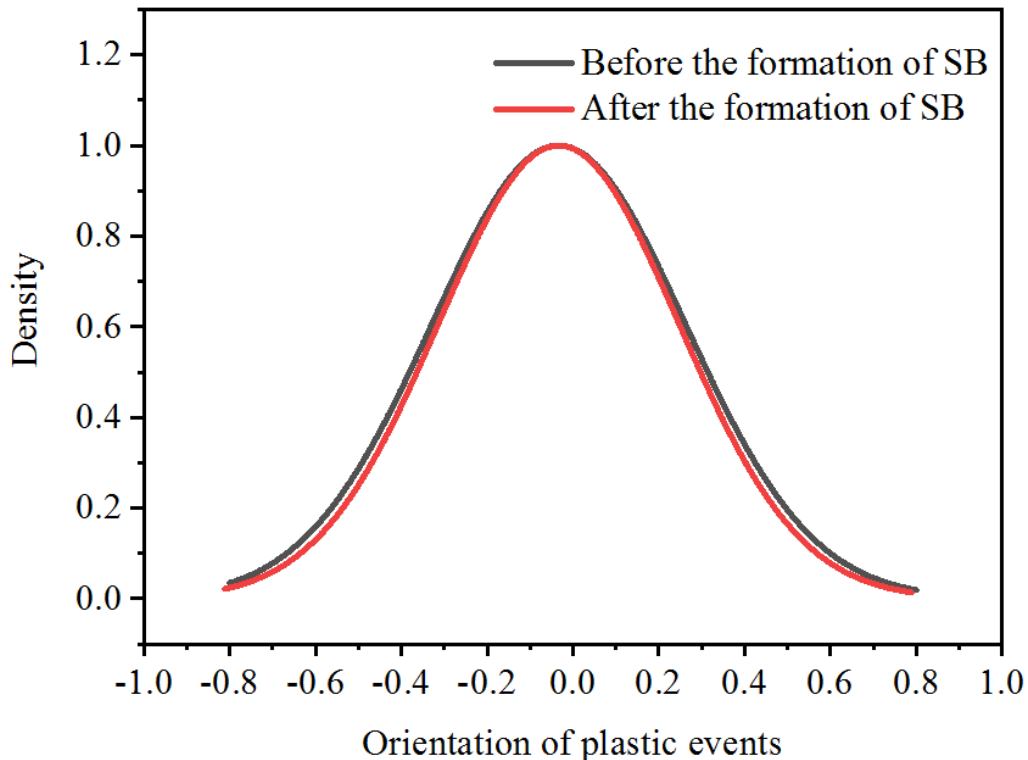


Figure 4.8: *Comparing the distribution of orientation of plastic events for $\text{Cu}_{64}\text{Zr}_{36}$ MG with quenching rate 10^{10} K/s before and after the formation of SB.*

4.2. EFFECT OF QUENCHING RATES AND COMPOSITIONS ON PLASTIC EVENTS

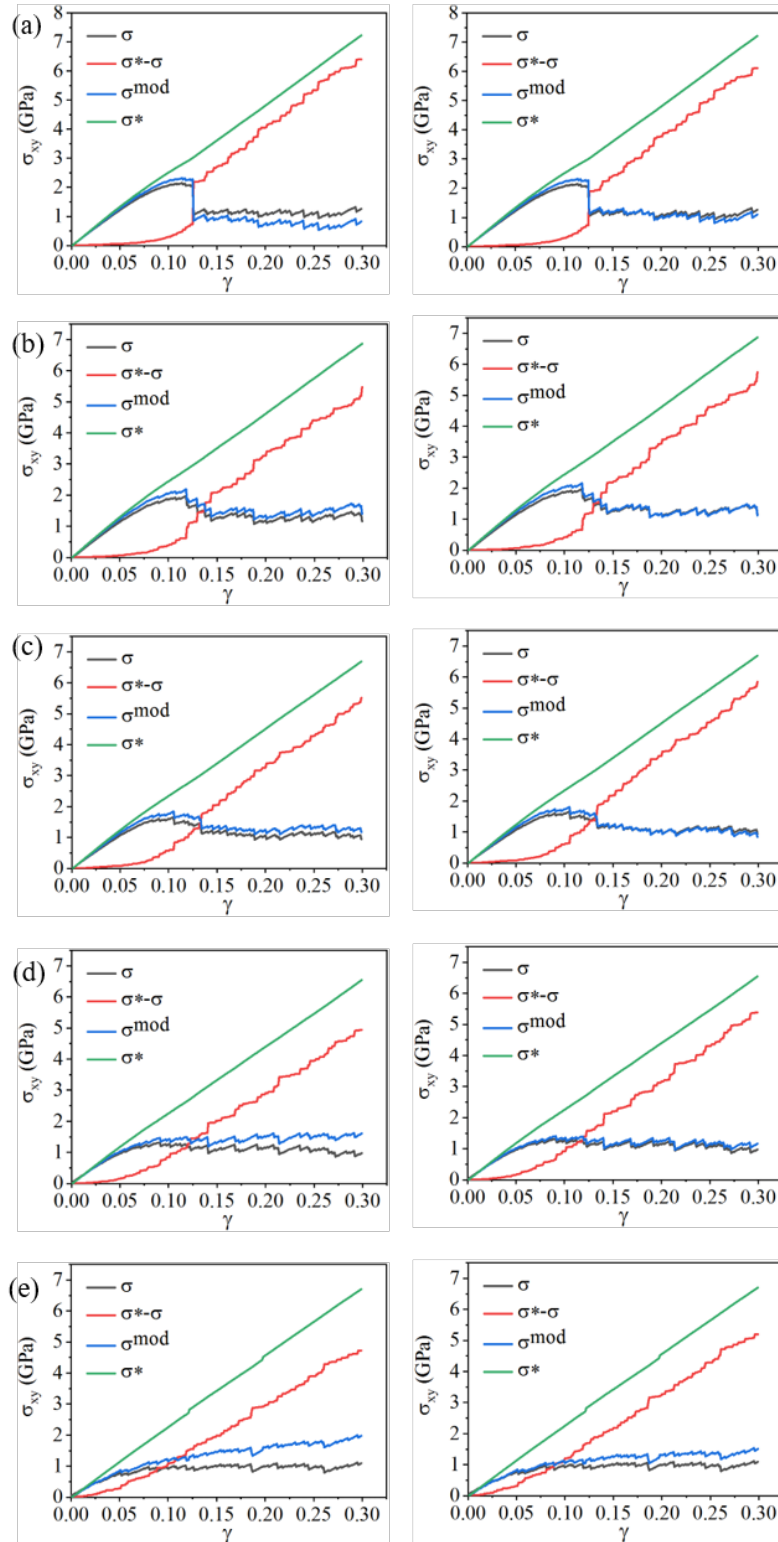


Figure 4.9: Fitting stress-strain curves and curves after correction with factor α of $\text{Cu}_{64}\text{Zr}_{36}$ MGs with different quenching rates (10^{10} K/s (a), 10^{11} K/s (b), 10^{12} K/s (c), 10^{13} K/s (d), and 10^{14} K/s (e), respectively; left is the original curves and right is after correction by a factor $\alpha=1.01$ for 10^{10} K/s, $\alpha=1.03$ for 10^{11} K/s, $\alpha=1.03$ for 10^{12} K/s, $\alpha=1.09$ for 10^{13} K/s and $\alpha=1.1$ for 10^{14} K/s).

Using the procedure based on the Eshelby's inclusions theory (described in Chapter 2), we have fitted the stress-strain curves, as shown in Figure 4.9. The fitting curve can perfectly reproduce the shape (fluctuations) of the stress-strain curve obtained from the MD simulation. For all quenching rates but the smallest one (10^{10} K/s), the fitting curve (blue curve) is slightly above the MD stress-strain curve (black curve), and the discrepancy slowly increases with the strain. We speculate that it is due to the removal of the smallest plastic events in the procedure of selection of the relevant plastic events, thus underestimating the plastic stress. Moreover, due to the occurrence of many events for each configuration, the quality of the displacement's fitting decreases since the Eshelby's inclusions can no longer be considered as single isolated events. Conversely, for the slowest rate, the fitting curve overestimates the stress before the yield point, and underestimates it after the stress drop. In this case we see that the stress drop at 12.3 % strain is overestimated by the fitting curve of the model. This can be due to the use of the minimum image convention, illustrated in Chapter 2. In fact, when the SB forms, many events participate in the atomic displacements, but only a limited fraction of them is taken into account in the minimum image convention due to the small size of the cell. These events induce large components of the Eshelby's strain tensor, thus leading to an overestimation of the plastic stress. In order to correct these discrepancies between the MD curves and the fitting stress-strain curves, we use a corrective factor α applied to the plastic stress, which ranges between 1.0 and 1.1 for the quenching rates different from 10^{10} K/s. This factor compensates the underestimation of the plastic stress and increases with the quenching rate, which is expected since more plastic events are present for higher quenching rates and thereby we neglect a larger number of plastic events. In this way we can obtain a very good overlap of the MD curve and the fitting curve, except for the highest quenching rate. For the smallest quenching rate, 10^{10} K/s we first apply a corrective factor of 0.7 on the stress drop at 12.3 % and then we apply a factor $\alpha=1.01$ to the whole plastic stress.

4.2.2 Influence of the metallic glass composition

The cumulative number and the cumulative plastic intensity of plastic events with shear strain for three different MG compositions are reported in Figure 4.10. Both are smaller

4.2. EFFECT OF QUENCHING RATES AND COMPOSITIONS ON PLASTIC EVENTS

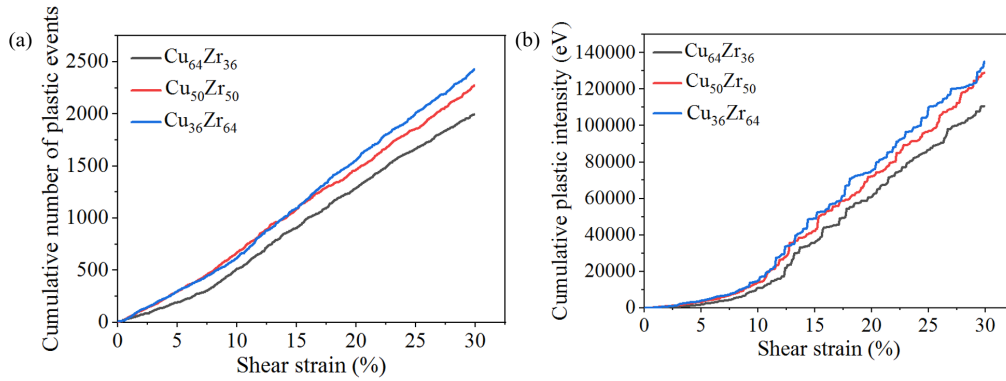


Figure 4.10: Cumulative number (a) and plastic intensity (b) of plastic events as a function of the shear strain for the three compositions.

for the $\text{Cu}_{64}\text{Zr}_{36}$ MG, i.e., with higher Cu ratio. This is expected since such composition leads to a higher shear modulus (Figure 3.17 (a)). The jump on the cumulative plastic intensity curve of the $\text{Cu}_{64}\text{Zr}_{36}$ seems to correspond to the stress drop on the stress-strain curve (Figure 4.11).

The average size, the average number and the average plastic intensity, as a function of the shear strain are reported in Figure 4.12 to 4.14. The former increases with shear strain up to the yield point and then fluctuates (with a larger amplitude) around a stabilized value. There are no significant differences between the different formulations, except maybe larger fluctuations with the composition with less Cu. Regarding the curves about the number of plastic events, larger fluctuations are visible above the yield point for this same composition. Conversely, below the yield points the number of plastic events decreases with the increase in the Cu content in the composition. The curves of the intensity of the plastic events of the three compositions roughly superimpose before the yield point. They show large fluctuations above the yield point, which seem also to increase with the decrease of Cu in the composition.

To sum up, with the decrease of the Cu content, more plastic events occur below the yield point (their intensity and their size are similar for all the Cu content), and above the yield point, the plastic intensity and the average size seems to fluctuate more. As we have seen in the previous Section 4.1.1, larger and more numerous plastic events, as for instance in the case of high quenching rates, seem to be correlated to less pronounced strain localization. In fact, by inspecting Figure 3.18 (d)-(e), we see that the same trend is

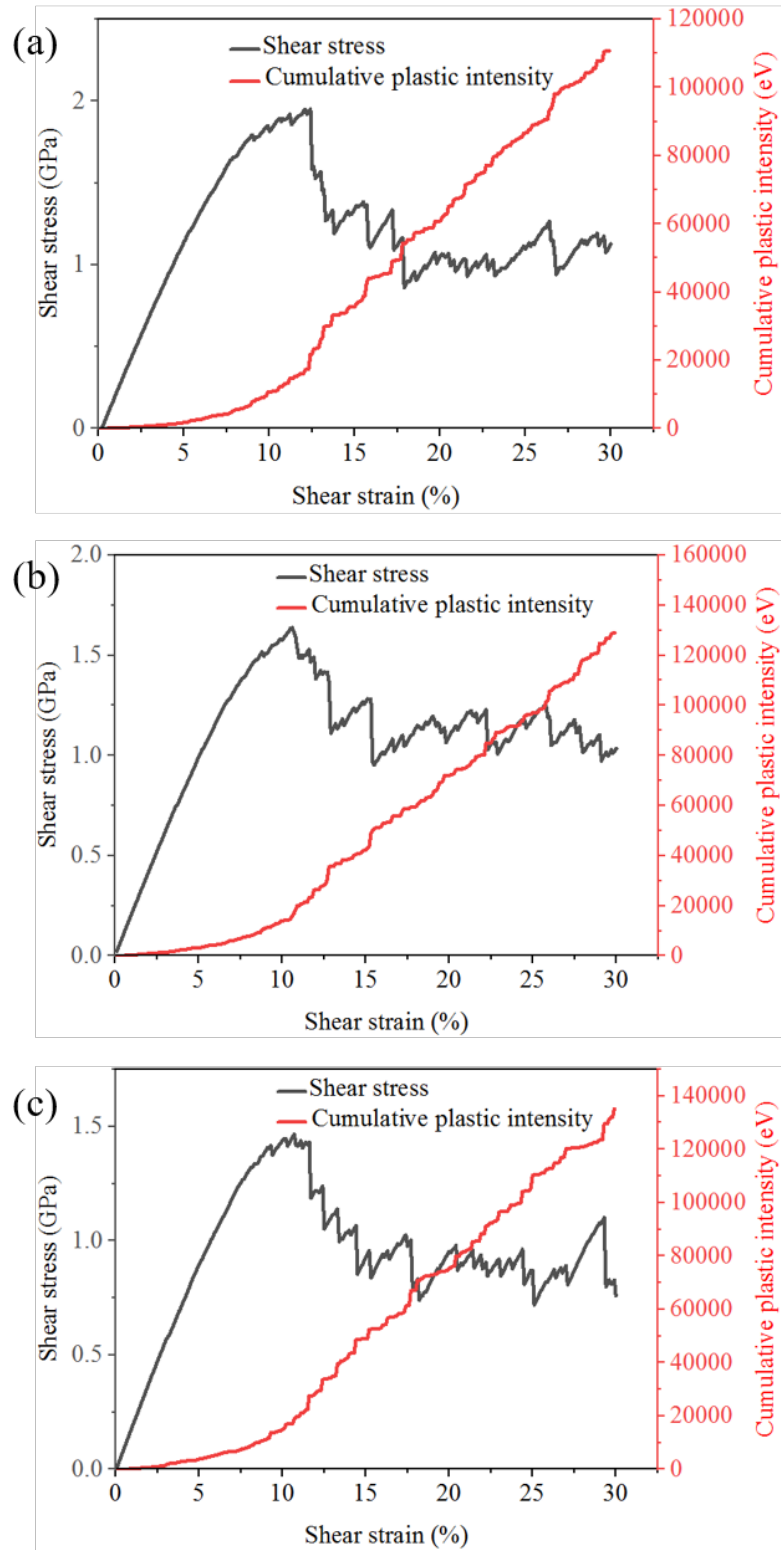


Figure 4.11: Shear stress and cumulative plastic intensity as a function of the shear strain for the three compositions, $Cu_{64}Zr_{36}$ (a), $Cu_{50}Zr_{50}$ (b), and $Cu_{36}Zr_{64}$ (c).

4.2. EFFECT OF QUENCHING RATES AND COMPOSITIONS ON PLASTIC EVENTS

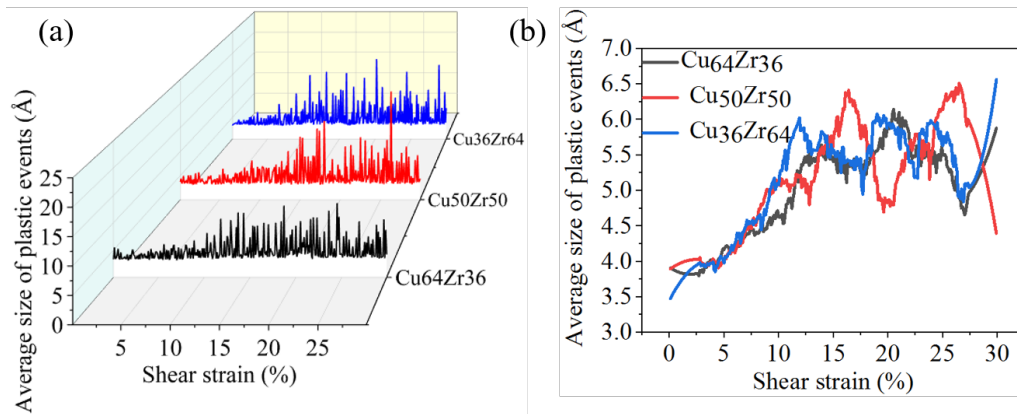


Figure 4.12: Average size of plastic events as a function of the shear strain for the three compositions (a) and the curves after smoothed with SG filter method (b).

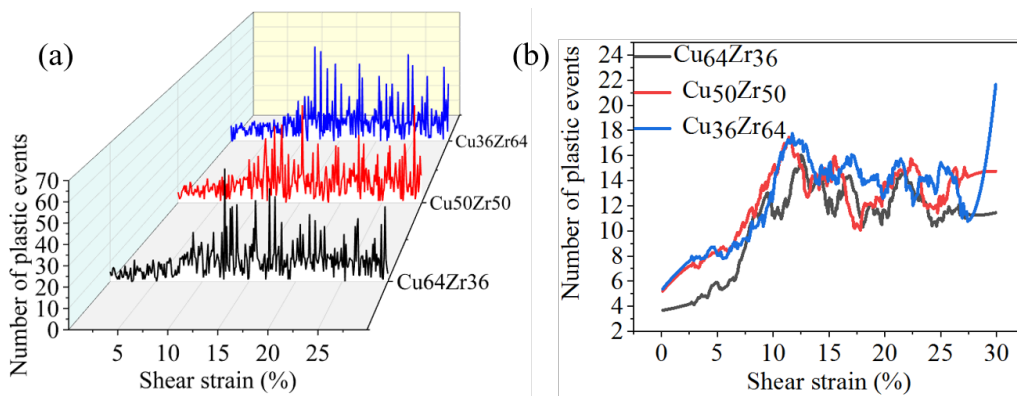


Figure 4.13: Number of plastic events as a function of the shear strain for the three compositions (original curves (a) and smoothed one with SG filter method (b)).

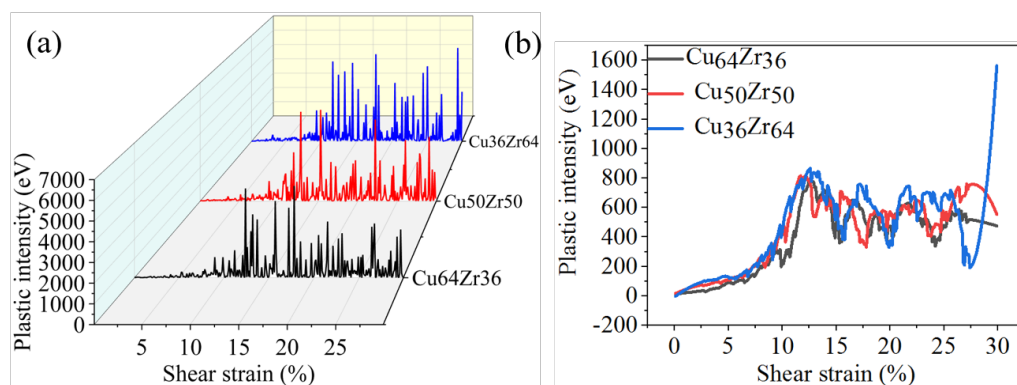


Figure 4.14: Plastic intensity of the plastic events with a function of the shear strain for the three compositions (original curves (a) and smoothed one with SG filter method (b)).

followed when decreasing the Cu content, since the composition with less Cu displays a more uniform atomic strain distribution.

Additionally, we have compared the distribution of the orientation of the plastic events. The width of the distribution plotted in Figure 4.15 is slightly larger for the lowest Cu content, suggesting again more variability of the plastic events for this composition.

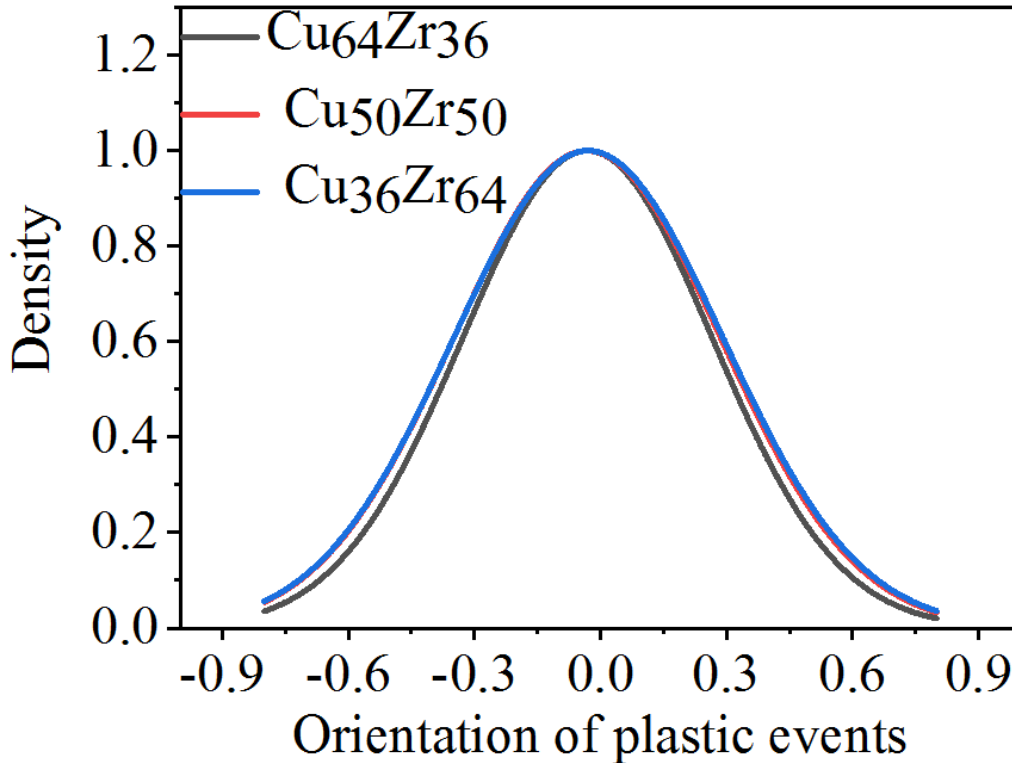


Figure 4.15: *Distribution of the orientation of the plastic events of MGs with three different compositions.*

Table 4.2: *Sigma values of the distribution of the orientation of the plastic events for the three compositions.*

Composition	$Cu_{64}Zr_{36}$	$Cu_{50}Zr_{50}$	$Cu_{36}Zr_{64}$
Sigma	0.297643	0.318623	0.321432

Finally, we have tried to reconstruct the MD stress-strain curves of the different compositions with the Eshelby's inclusion model. Figure 4.16 (a)-(c) show the original fitting curves. The fitting quality decreases with the Cu content. As already explained in Section 4.1.1, this might come depend on the use of the minimum image convention. To

account for the underestimation of the stress we apply a corrective factor α to the plastic stress, to reduce the stress drop and improve the fitting of the stress-strain curves in Figure 4.16 (d)-(f): with $\alpha=0.93$ on plastic stress from 12.5 % to 17.8 % for $Cu_{64}Zr_{36}$, $\alpha=0.97$ for $Cu_{50}Zr_{50}$ and $\alpha=0.88$ for $Cu_{36}Zr_{64}$, the fitting is very satisfactory for all the compositions.

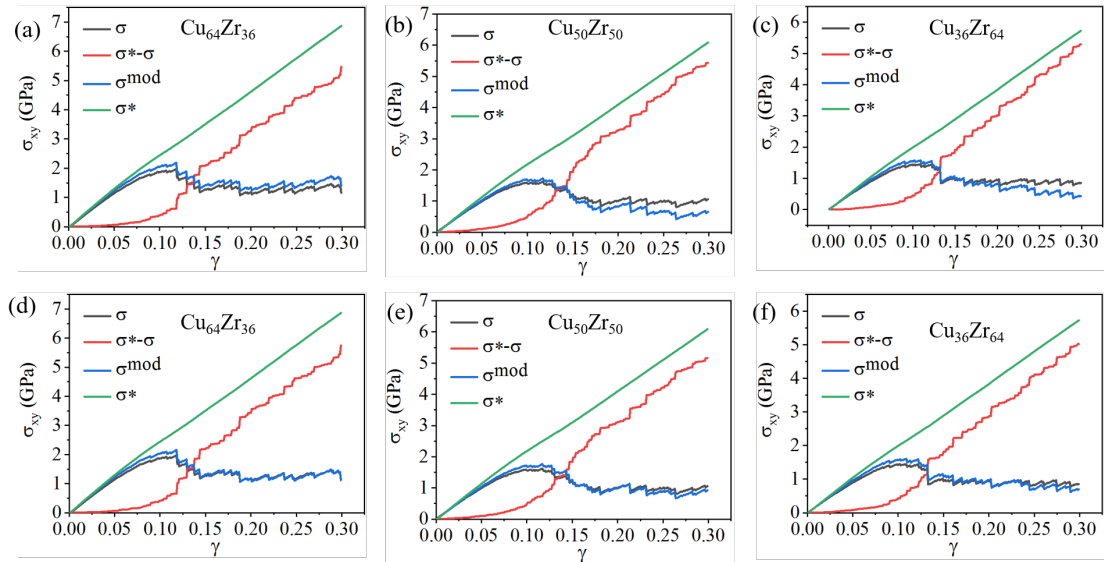


Figure 4.16: The fitting stress-strain curves of three compositions after quenched with quenching rate 10^{11} K/s before correction ((a), (b) and (c)) and after correction ((d), (e) and (f)).

4.3 Prospect for tensile tests

In order to evaluate if a change in the soliciation type strongly modifies the previous conclusion, we also investigate the tensile properties of $Cu_{64}Zr_{36}$ MG after different quenching rates. In this case, in order to avoid finite size effects, we take a simulation box twice larger in the X direction than the box used for shear since the plastic events tend to be stretched in the direction of the applied tensile strain, as schematically illustrated in Figure 4.17. The total number of atoms in this case is 64000. The dimensions of the box are 160 Å in the x-direction and 80 Å in the y- and z-directions. The numerical sample is cooled down to 0.1 K from the liquid state through the same different quenching rates previously explored, 10^{10} K/s to 10^{14} K/s and relaxed at 0.1 K for 2 ns. The deformation is performed in the X direction by steps of 0.05 %. The dimensions on the Y and Z directions are adjusted to keep the global volume of the box constant. After each strain step,

the potential energy of the system is minimized by FIRE minimize style (see Chapter 2). The obtained tensile stress-strain curves are shown in Figure 4.18. The Young's modulus, yield stress and yield strain extracted from the stress-strain curves are reported in Figure 4.19.

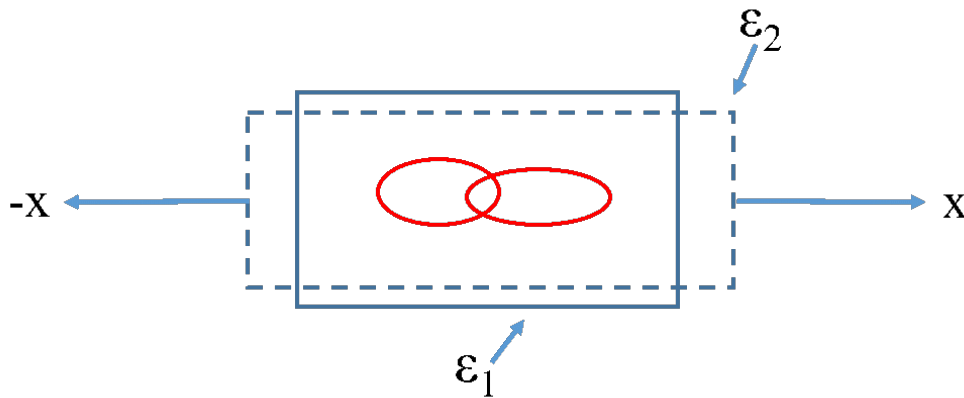


Figure 4.17: The schematic of plastic events during tensile deformation. Red ellipses represent the plastic events. Blue square represents the deformed MG system.

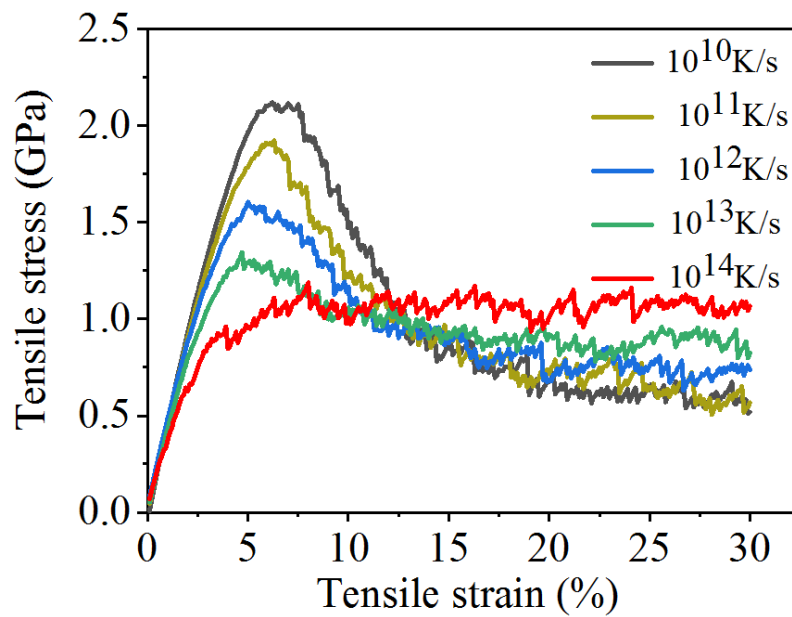


Figure 4.18: Tensile stress-strain curves of $\text{Cu}_{64}\text{Zr}_{36}$ MG with different quenching rates.

As expected, in agreement with our previous results from shear test, and with previous work [Mayr, 2005, Xiao et al., 2010], the Young's modulus and yielding stress increases with the decrease of the quenching rate, i.e., for more relaxed material.

As seen in Figure 4.20, at the same tensile strain, the cumulative number of plastic events and the cumulative plastic intensity are larger for MG with higher quenching rates. However, we do not observe small jumps on the cumulative plastic intensity curves like those for shear deformation. This is consistent with the absence of a large stress drop (such as the one observed in shear).

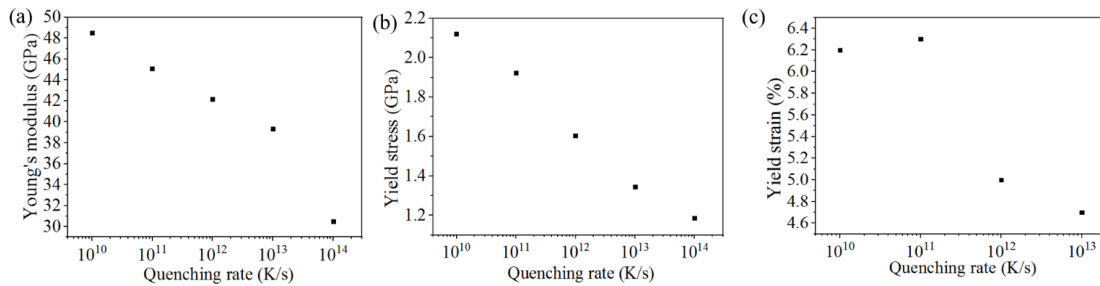


Figure 4.19: Young's modulus (a), yield stress (b) and yield strain (c) of $\text{Cu}_{64}\text{Zr}_{36}$ MG for different quenching rates deduced from the tensile stress-strain curve.

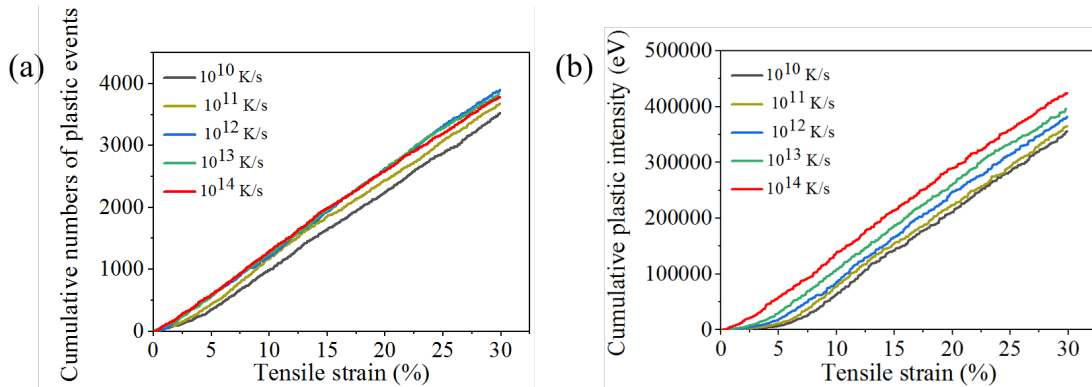


Figure 4.20: Cumulative number (a) and cumulative plastic intensity (b) of plastic events of $\text{Cu}_{64}\text{Zr}_{36}$ MG after tensile deformation with different quenching rates.

The number, plastic intensity and average size of plastic events of $\text{Cu}_{64}\text{Zr}_{36}$ MG with different quenching rates with tensile strain are shown in Figure 4.21 to Figure 4.23. The conclusions are very similar to the one made for shear test. Below the yield point, the number, size and intensity of the plastic events increase more rapidly for the smallest

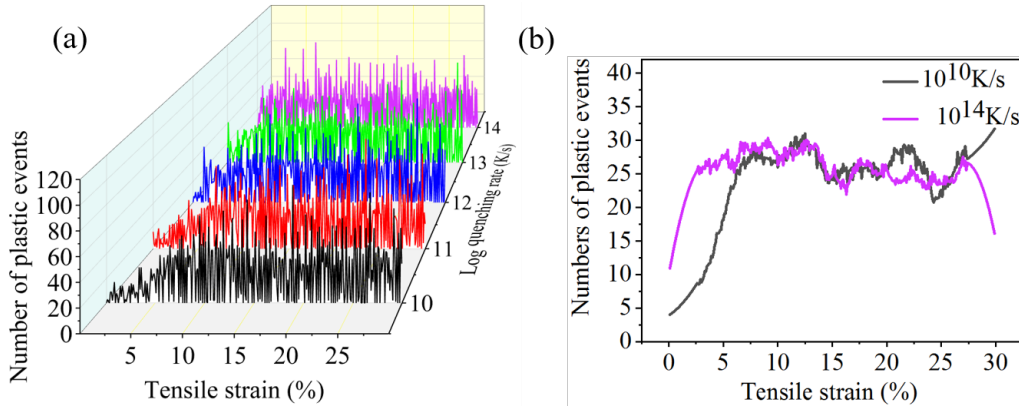


Figure 4.21: Number of plastic events as a function of the tensile strain for $\text{Cu}_{64}\text{Zr}_{36}$ MG quenched at different quenching rates (a) and smoothed curve for quenching rate 10^{10} K/s and 10^{14} K/s (b).

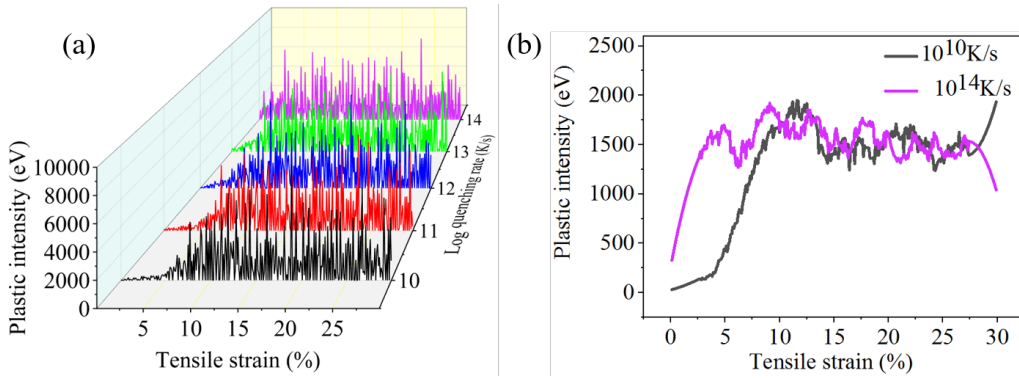


Figure 4.22: Plastic intensity of plastic events as a function of the tensile strain for $\text{Cu}_{64}\text{Zr}_{36}$ MG quenched at different quenching rates (a), smoothed curve for quenching rate 10^{10} K/s and 10^{14} K/s (b).

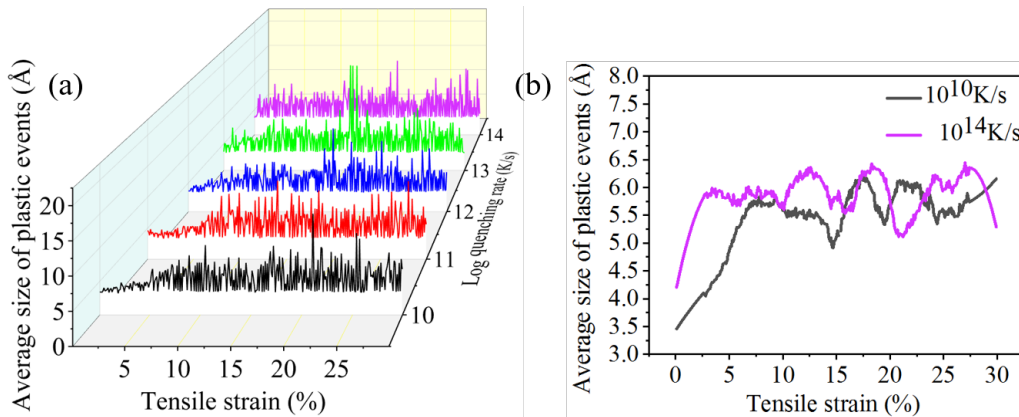


Figure 4.23: Average size of plastic events as a function of the tensile strain for $\text{Cu}_{64}\text{Zr}_{36}$ MG quenched at different quenching rates (a) and smoothed curves for 10^{10} K/s and 10^{14} K/s (b).

quenching rates, and therefore reach more rapidly a stabilised value which is roughly the same for the three quenching rates above the yield point. The data are also more scattered for the fastest quenching rate. Correspondingly, MGs for higher quenching rate have a more uniform deformation during tensile deformation, as shown in Figure 4.24.

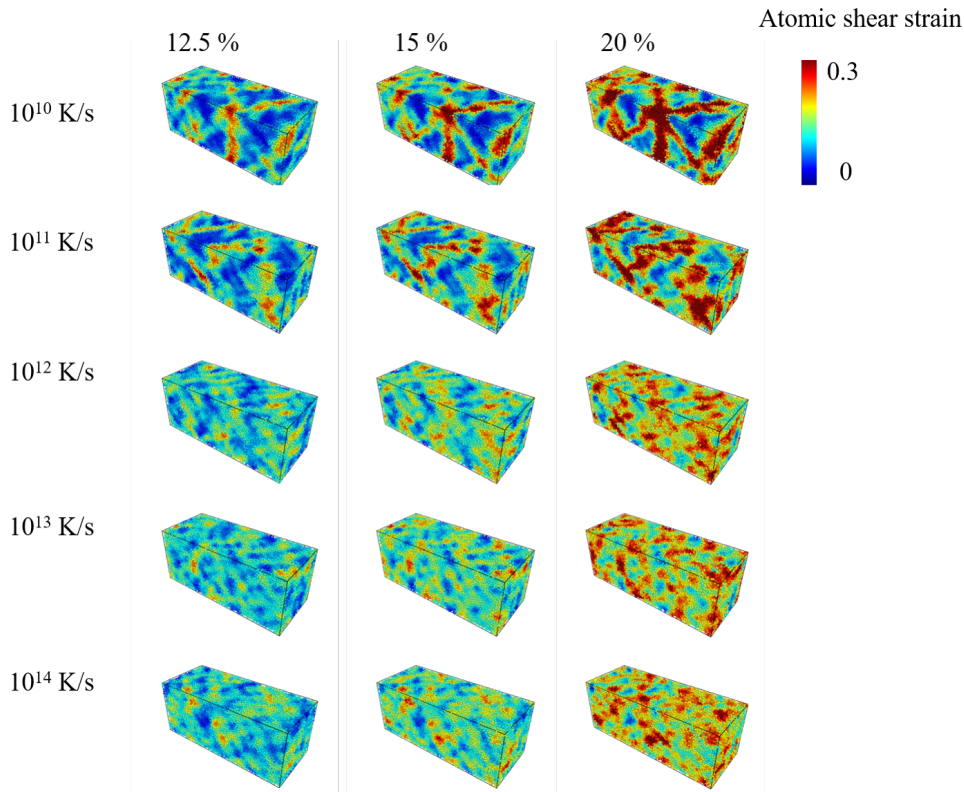


Figure 4.24: Map of the atomic shear strain for tensile strain 12.5 %, 15 % and 20 % for $\text{Cu}_{64}\text{Zr}_{36}$ MG quenched at different quenching rates.

The Eshelby's inclusion model that we have used for shear cannot be directly applied to tensile deformation in its present form, thus we do not show the fitting of the stress-strain curves in the tensile case. In fact, we find that the plastic stress is abnormally underestimated, yielding a bad fit especially at high strains. This issue seems to be related to the high number of large events formed at each configuration that cause a bad quality displacement's fitting. A possible solution to get rid of this problem would be to change the displacement's fitting routine by fitting the displacement field due to each inclusion one at a time and not as an ensemble for a given configuration. This strategy will be certainly explored in a future work.

4.4 Discussion and conclusion

Through the study of effect of the quenching rate and composition on the plasticity of Cu-Zr MGs at the microscopic scale and the comparison of the mechanical properties, the following conclusions are obtained. Before the yield point, more and larger plastic events with higher plastic intensity are observed for Cu-Zr MGs with higher quenching rate and less Cu ratio, which are beneficial to better plasticity. At the yield point, plastic intensity increases more sharply for systems at lower quenching rate and with more Cu content, which is consistent with a stronger localization, while the increase of plastic intensity, number and size of the plastic events is smoother when increasing the quenching rate and/or decreasing the Cu content, leading to more uniform plastic deformation at the macroscopic scale. The orientation of the plastic events is more scattered for high quenching rates, suggesting a more homogeneous distribution of the plastic events, while the formation of the shear band does not seem to produce a noticeable effect on the orientation.

Chapter 5

Effect of thermal cycling on metallic glasses

Contents

5.1	Introduction	102
5.2	Thermal cycling treatment	102
5.3	Effect of thermal cycling on metallic glasses with different initial quenching rates	103
5.4	Effect of thermal cycling for different metallic glass composition	111
5.5	Discussion and conclusion	117

5.1 Introduction

In this chapter, we investigate the effect of thermal cycling on the global plastic behavior of Cu-Zr metallic glasses (MGs) prepared with different quenching rates. Additionally, the effect of thermal cycling on their plastic events is analyzed at the microscopic scale, in terms of number, size, plastic intensity and orientation.

5.2 Thermal cycling treatment

Thermal cycling has been introduced in Chapter 1 as an effective thermal treatment method to improve the plasticity of metallic glasses (MGs). Moreover, there have been many studies on the effects of different parameters of thermal cycling on the properties of MGs, including experimental and simulation methods [Ketov et al., 2015, Song et al., 2018, Grell et al., 2018, Priezjev, 2019, Shang et al., 2021, Shang et al., 2018]. Thermal cycling does not affect the glass forming ability (GFA) of MGs compared to other methods of improving plasticity, such as composition modification [Guo et al., 2018]. In contrast to shot peening, it does not alter the surface of the MG [Concuestell et al., 2009, Nieh et al., 2012], and it is easy to be applicable across the whole MG sample.

Figure 5.1 shows the variation of temperature with time during one thermal cycle we chose to apply to our MGs. The initial quenching rate down to 0.1 K of the simulated MG is varied from 10^{10} K/s to 10^{14} K/s. After this quenching, the system is heated up to 400 K and then cooled down to 0.1 K for 100 times. The heating and cooling rate are the same, $1.6 \cdot 10^{14}$ K/s, which corresponds to a nearly instantaneous process [Shang et al., 2021]. During this process, the pressure remains constant. The upper temperature, 400 K is almost half of the glass transition temperature, which is below the temperatures normally associated with α and β thermal relaxations. The upper temperature, 400 K is maintained for 200 ps, and the lower temperature, 0.1 K is maintained for 20 ps. We checked that this choice of the annealing times favors the rejuvenation of the MG.

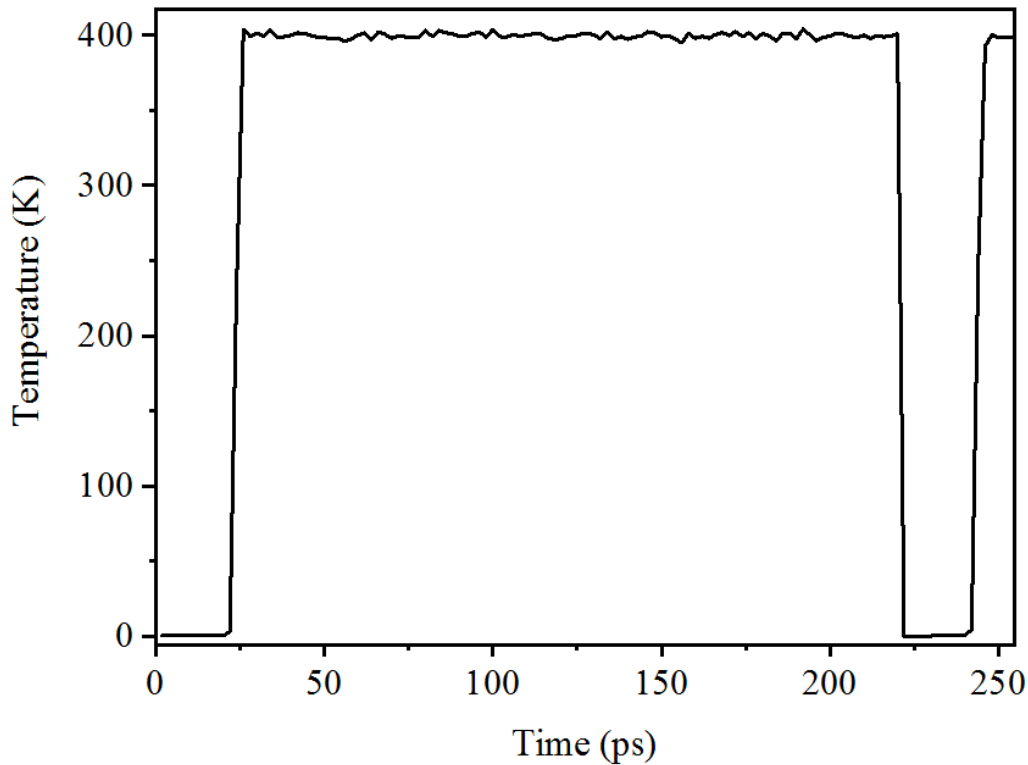


Figure 5.1: *Temperature as a function of time over one cycle.*

5.3 Effect of thermal cycling on metallic glasses with different initial quenching rates

Figure 5.2 shows the variation of the potential energy (PE) with the number of cycles, $Cu_{64}Zr_{36}$ MGs prepared with different initial quenching rates. For the lowest initial quenching rates, such as 10^{10} K/s and 10^{11} K/s, the PE increases with the number of cycles, meaning that the sample undergoes some rejuvenation. For higher quenching rates, such as 10^{13} K/s and 10^{14} K/s, PE decreases with the number of cycles, meaning, conversely, that the sample ages. The PE variation is slight for the quenching rate of 10^{12} K/s, which can be defined as a critical quenching rate.

In terms of microstructure, we already know that the lower quenching rates, the more there are $\langle 0,0,12,0 \rangle$ (full icosahedra, FI) inside $Cu_{64}Zr_{36}$ MG. As shown in Figure 5.3, after thermal cycling, the FI fraction decreases for the quenching rates 10^{10} K/s and 10^{11} K/s, suggesting an easier plasticity for these systems, while for $Cu_{64}Zr_{36}$ MGs prepared

5.3. EFFECT OF THERMAL CYCLING ON METALLIC GLASSES WITH DIFFERENT INITIAL QUENCHING RATES

with the highest quenching rates (10^{13} K/s and 10^{14} K/s), the FI fraction (which is initially

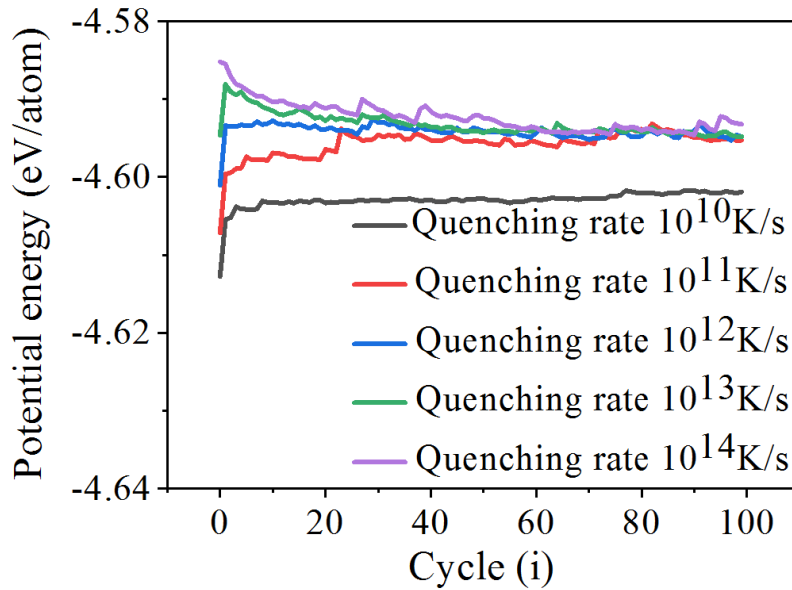


Figure 5.2: Potential energy (PE) as a function of the number of thermal cycles for $Cu_{64}Zr_{36}$ MGs with different quenching rates.

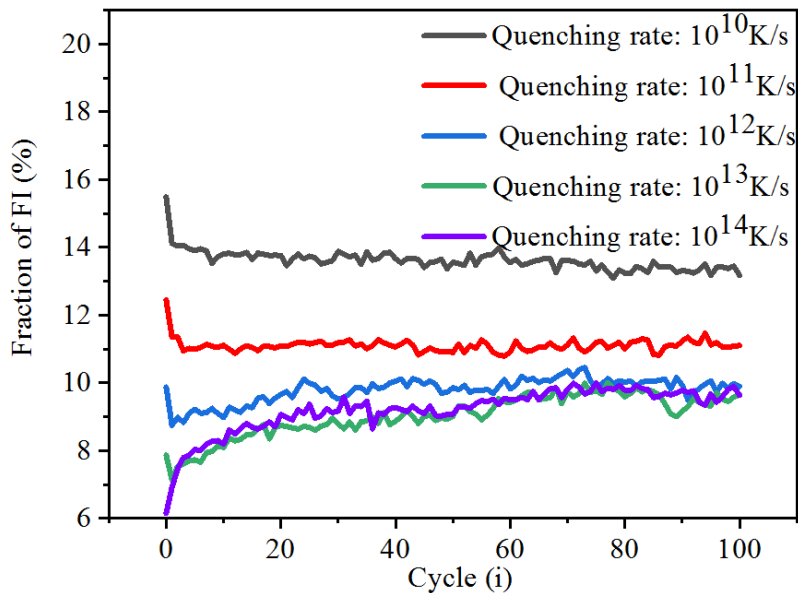


Figure 5.3: The variation of FI fraction as a function of the number of thermal cycling, for $Cu_{64}Zr_{36}$ MGs prepared with different quenching rates.

lower). For the “critical” quenching rate (10^{12} K/s), the FI fraction variation is very small. In order to understand the microscopic evolution of the system after the thermal treat-

ment we calculated the non-affine square displacement D_{min}^2 [Hufnagel, 2015] (the deviation with respect to local linear deformation) at different numbers of cycles, using the previous cycle as reference. Their 3D mapping is reported in Figure 5.4 for the different quenching rates. Only the atoms with $D_{min}^2 > 100\text{\AA}^2$ are visualized in the figure. Obviously, for $\text{Cu}_{64}\text{Zr}_{36}$ MGs with the highest quenching rates, more atoms undergo a large nonaffine square displacement after experiencing the first thermal cycle. This means that the mobility of atoms is initially easier, which is consistent with the high initial PE of this less-relaxed MG. For the more relaxed $\text{Cu}_{64}\text{Zr}_{36}$ MGs (i.e., prepared with the lowest quenching rates, 10^{10} K/s, 10^{11} K/s and 10^{12} K/s), the number of atoms showing large nonaffine square displacement increases when the number of cycles increases.

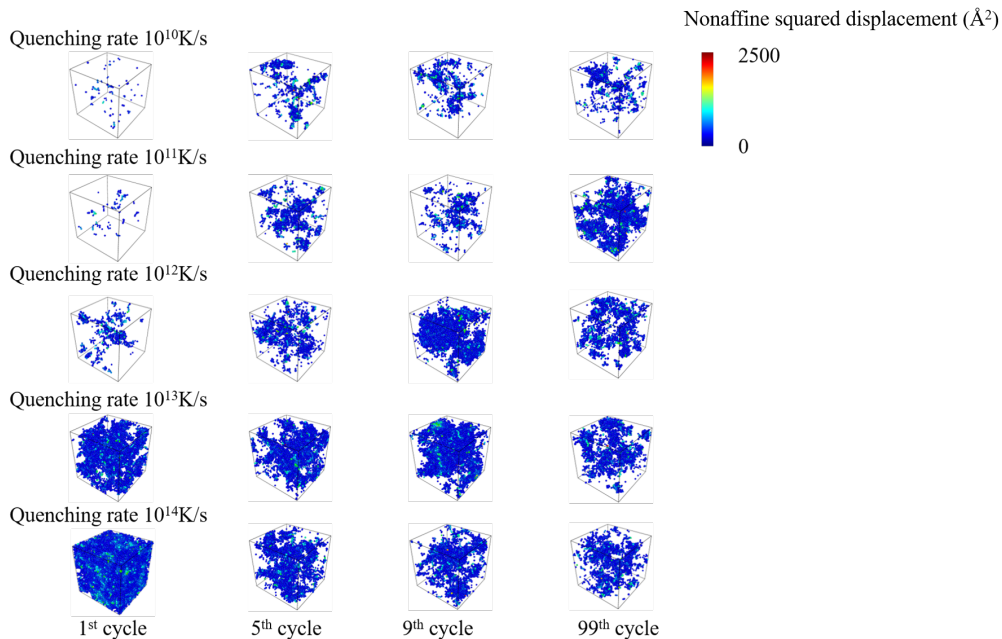


Figure 5.4: Map of the distribution of the non-affine square displacement ($D_{min}^2 > 100\text{\AA}^2$) at the 1st, 5th, 9th and 99th cycle, calculated with the previous cycle as reference, for $\text{Cu}_{64}\text{Zr}_{36}$ MGs prepared with different quenching rates.

Conversely, it decreases with the two highest quenching rates, i.e., the less-relaxed $\text{Cu}_{64}\text{Zr}_{36}$ MGs. Therefore, we can deduce that the change in energy state is caused by the accumulated nonaffine square displacement [Priezjev, 2019]. In fact, as we can see by comparing Figure 5.4 and 5.2, most of the variation of the nonaffine square displacement and of the PE occurs between the first cycle and the ninth cycle, while the PE stabilizes afterwards

5.3. EFFECT OF THERMAL CYCLING ON METALLIC GLASSES WITH DIFFERENT INITIAL QUENCHING RATES

together with a weaker evolution of the nonaffine displacements.

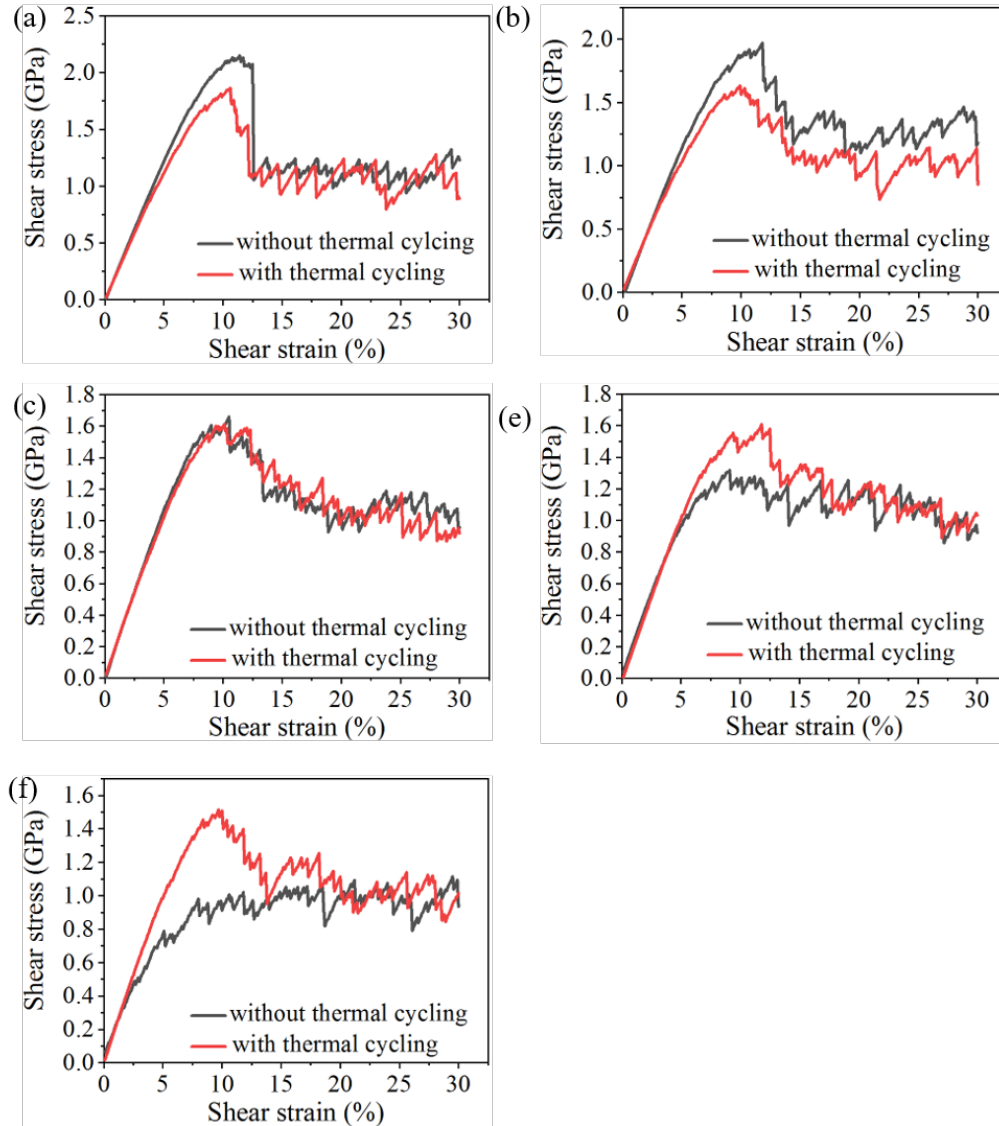


Figure 5.5: Stress-strain curves of $\text{Cu}_{64}\text{Zr}_{36}$ MG quenched at different quenching rates (10^{10} K/s (a), 10^{11} K/s (b), 10^{12} K/s (c), 10^{13} K/s (d) and 10^{14} K/s (e), respectively) and submitted or not to 100 thermal cycles.

We now focus our attention on the influence of the thermal cycling on the mechanical properties of the same samples. Figure 5.5 presents their stress strain curves during a quasi-static shear deformation at 0.1 K, when they have been submitted or not to the thermal treatment. The deduced shear modulus, yield stress and flow stress are reported in Figure 5.6. For the lowest quenching rates (10^{10} K/s- 10^{12} K/s) they are reduced by

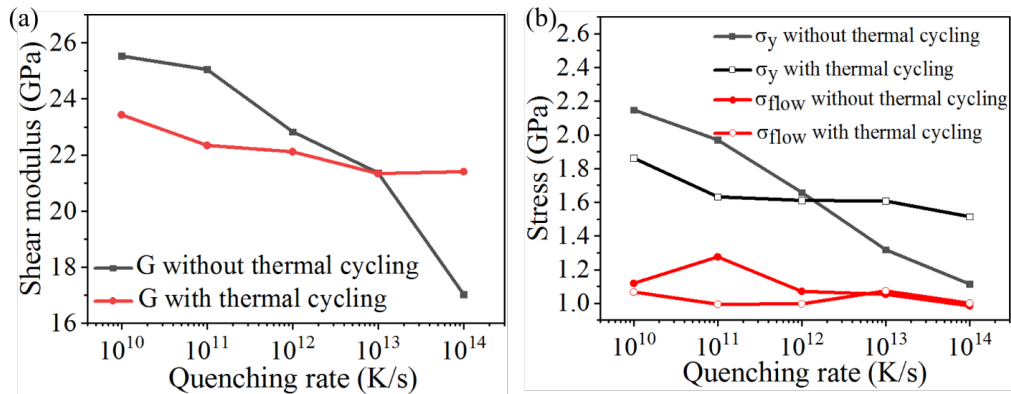


Figure 5.6: Shear modulus (a), yield stress and flow stress (b) of $Cu_{64}Zr_{36}$ MG quenched at different initial quenching rates with and without thermal cycling.

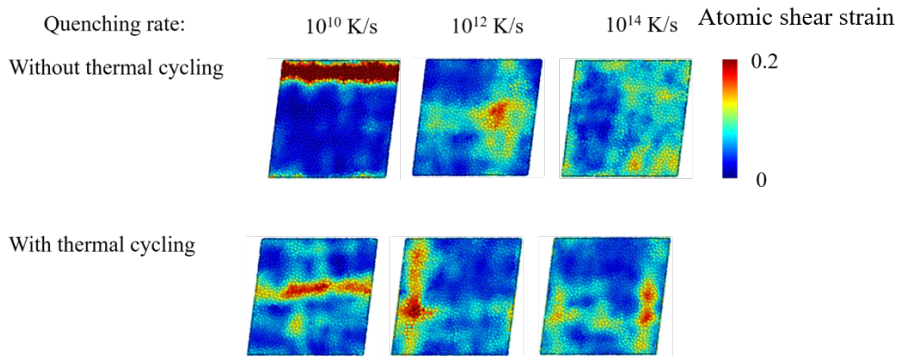


Figure 5.7: Comparison of atomic shear strain of $Cu_{64}Zr_{36}$ MG quenched at different initial quenching rates with and without thermal cycling, at strain 12.7 %.

the thermal cycling treatment and their decrease is larger when the quenching rate is lower. For the highest quenching rate (10^{13} K/s and 10^{14} K/s), thermal cycling leads to an increase in the shear modulus and yield stress, with a larger increase for higher quenching rate, while the flow stress does not vary significantly.

From Figure 5.7, where we compare the atomic shear strain, it can be found that thermal cycling decreases the localization of the shear transformations (STs) for well-relaxed MG and increases the localization of the STs for the less-relaxed $Cu_{64}Zr_{36}$ MG, while for $Cu_{64}Zr_{36}$ MG with a critical quenching rate (10^{12} K/s), the variation is not significant.

To go further, we can compare some parameters of the plastic events occurring in the less and most relaxed MGs (i.e. prepared with the quenching rate 10^{10} K/s and 10^{14} K/s) submitted or not to thermal cycling treatment.

5.3. EFFECT OF THERMAL CYCLING ON METALLIC GLASSES WITH DIFFERENT INITIAL QUENCHING RATES

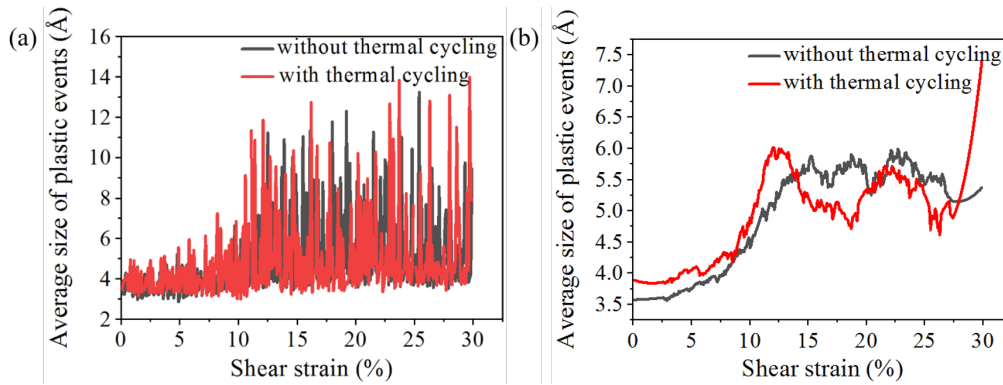


Figure 5.8: Comparison of average size of plastic events of $\text{Cu}_{64}\text{Zr}_{36}$ MG (initial quenching rate 10^{10} K/s) without and with thermal cycling (a) and smoothed curves (b).

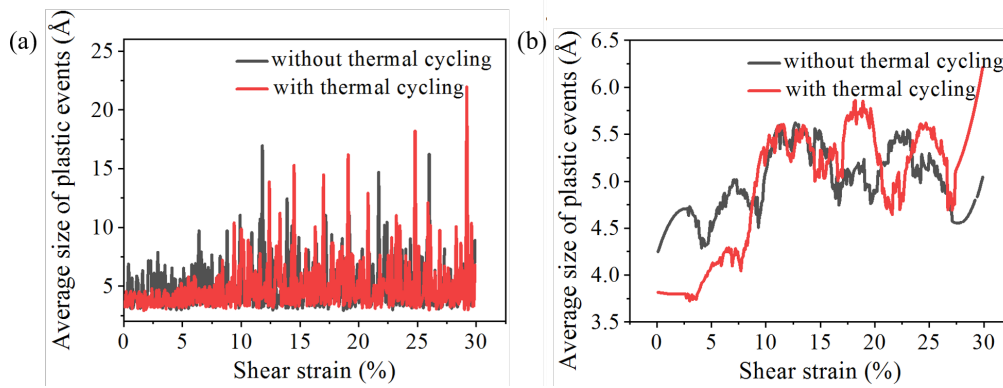


Figure 5.9: Comparison of average size of plastic events of $\text{Cu}_{64}\text{Zr}_{36}$ MG (initial quenching rate 10^{14} K/s) without and with thermal cycling (a) and smoothed curves (b).

Figure 5.8 and Figure 5.9 show the average size of the plastic events as a function of the shear strain. At small strains, for the system with quenching rate 10^{10} K/s, it is larger when the system has been submitted to thermal cycling, while for the system prepared with quenching rate 10^{14} K/s, the opposite is observed. After the yield strain, given the strong oscillations on the curves, the difference between them cannot be commented.

Figure 5.10 and Figure 5.11 show the number of the plastic events as a function of the shear strain for $\text{Cu}_{64}\text{Zr}_{36}$ MG initially prepared with quenching rates of 10^{10} K/s and 10^{14} K/s, and submitted or not to thermal cycling. For quenching rate 10^{10} K/s, the curves are roughly the same except (in average) a slight increase of the number of plastic events with thermal treatment whereas for quenching rate 10^{14} K/s, we can clearly see that at small strains (below the yield strain), less plastic events occur in the $\text{Cu}_{64}\text{Zr}_{36}$ MG

submitted to thermal cycling treatment.

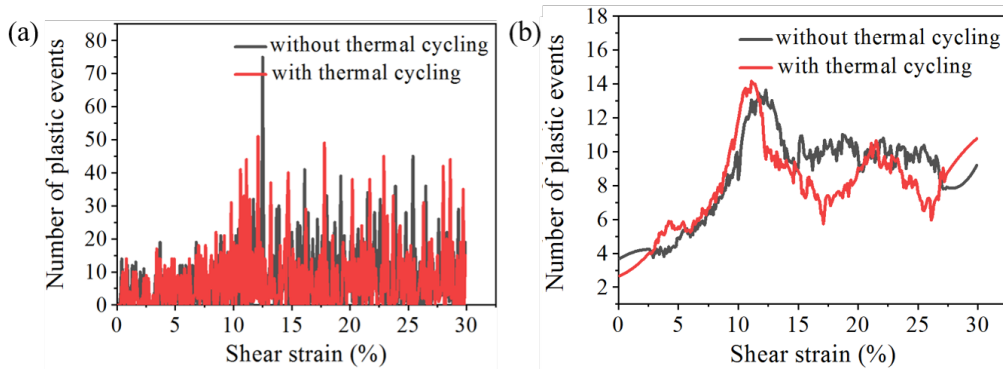


Figure 5.10: Number of plastic events of $\text{Cu}_{64}\text{Zr}_{36}$ MG (initial quenching rate 10^{10} K/s) without and with thermal cycling (a) and smoothed curves (b).

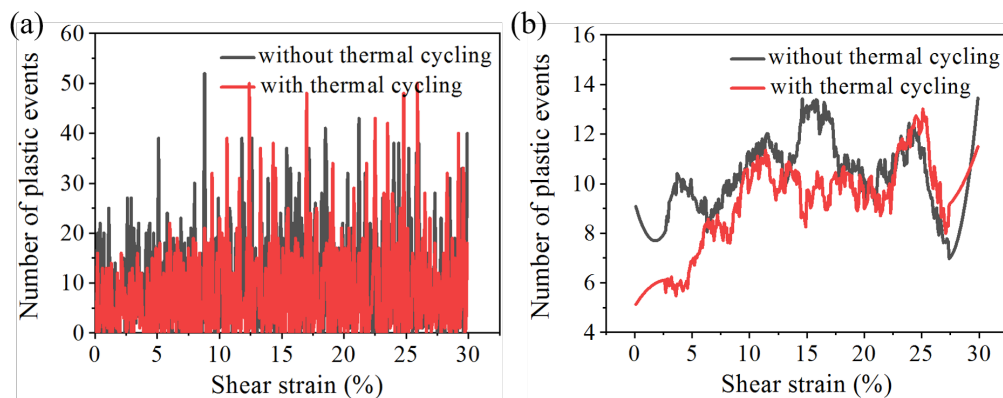


Figure 5.11: Number of plastic events of $\text{Cu}_{64}\text{Zr}_{36}$ MG (initial quenching rate 10^{14} K/s) without and with thermal cycling (a) and smoothed curves (b).

Figure 5.12 and Figure 5.13 show the plastic intensity of the plastic events as a function of the shear strain for $\text{Cu}_{64}\text{Zr}_{36}$ MG with initial quenching rates of 10^{10} K/s and 10^{14} K/s without and with thermal cycling. For the quenching rate of 10^{10} K/s, curves are very similar at small strains (below the yield strain), whereas the plastic intensity is smaller after thermal cycling for sample prepared with the quenching rate of 10^{14} K/s.

5.3. EFFECT OF THERMAL CYCLING ON METALLIC GLASSES WITH DIFFERENT INITIAL QUENCHING RATES

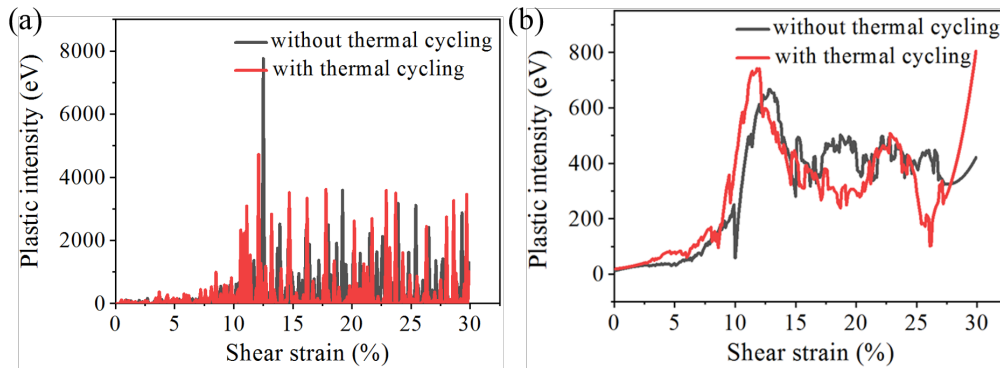


Figure 5.12: Plastic intensity of plastic events of $\text{Cu}_{64}\text{Zr}_{36}$ MG (initial quenching rate 10^{10} K/s) without and with thermal cycling (a) and smoothed curves (b).

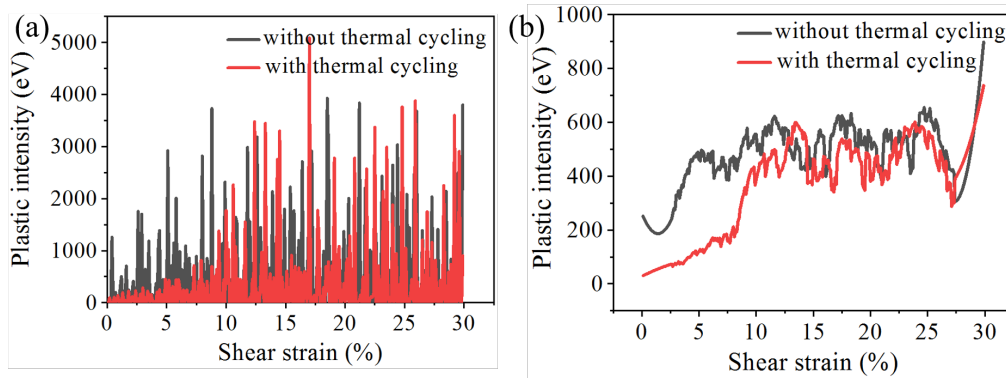


Figure 5.13: Plastic intensity of plastic events of $\text{Cu}_{64}\text{Zr}_{36}$ MG (initial quenching rate 10^{14} K/s) without and with thermal cycling (a) and smoothed curves (b).

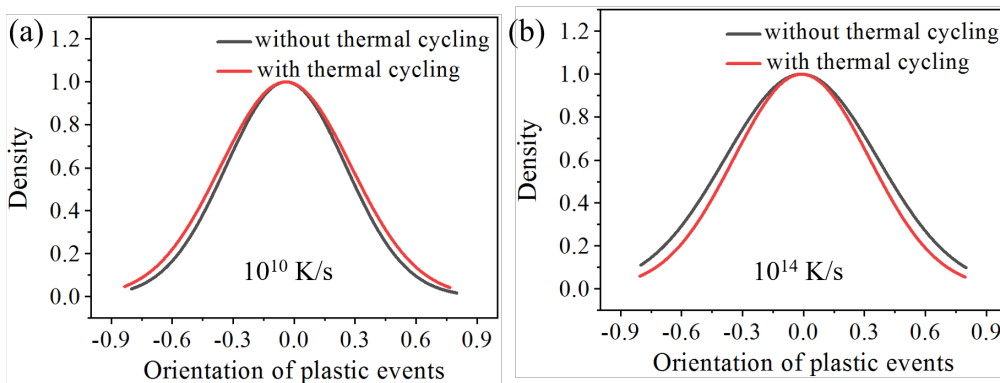


Figure 5.14: Distribution of orientation of plastic events of $\text{Cu}_{64}\text{Zr}_{36}$ MG without and with thermal cycling for a quenching rate of 10^{10} K/s (a) and a quenching rate of 10^{14} K/s (b).

Figure 5.14 shows a comparison of the orientation distribution of the plastic events for

the same systems. After the thermal cycling treatment, the width of the orientation distribution curve is broader for the $Cu_{64}Zr_{36}$ MG quenched at 10^{10} K/s, while it is narrower for $Cu_{64}Zr_{36}$ MG quenched at 10^{14} K/s. To summarize these findings, thermal cycling has a rejuvenation effect for the lowest quenching rates (10^{10} K/s and 10^{11} K/s) and an aging effect for the highest ones (10^{13} K/s and 10^{14} K/s). The rejuvenation effect seen in the most relaxed system results in plastic events slightly more numerous, with a larger average size (especially at small strains), a slightly more uniform distribution of their orientation. These are all beneficial to a more uniform deformation of MGs, as shown by the atomic shear strain distribution in Figure 5.7. Conversely, the aging effect of thermal cycling seen in the less relaxed system leads to smaller average size, smaller number, smaller plastic intensity and slightly less uniform orientation distribution of plastic events, consistent with a more localized deformation at the macroscopic scale.

5.4 Effect of thermal cycling for different metallic glass composition

The quenching rate is a key parameter in thermal cycling treatment. However, there is a lack of research on the effect of cryothermal cycling on the mechanical properties of MGs with different compositions and its analysis at the microscopic scale. In this section, the quenching rate is fixed at 10^{11} K/s, and the effects of thermal cycling on the mechanical properties of Cu-Zr MGs with different compositions, $Cu_{64}Zr_{36}$, $Cu_{50}Zr_{50}$ and $Cu_{36}Zr_{64}$, are compared firstly and then analyzed at the microscopic scale.

The variation of the potential energy (PE), δE is defined as $\delta E = E(i) - E(0)$, the difference between the current potential energy and the initial one. δE as a function of the number of thermal cycles is shown in Figure 5.15. For the three compositions, the PE increases after thermal cycling, indicating significant of a rejuvenation effect. The increase is larger for $Cu_{36}Zr_{64}$ than for the other two, which show a very similar curve. The rejuvenation effect of the thermal cycling is therefore more important for the $Cu_{36}Zr_{64}$, which contains less Cu. Additionally, we visualize in 3D the atoms with non-affine square displacement larger than 100 \AA^2 for the three compositions, submitted to different numbers of thermal cycling (Figure 5.16). This mapping shows that the increase in the number of

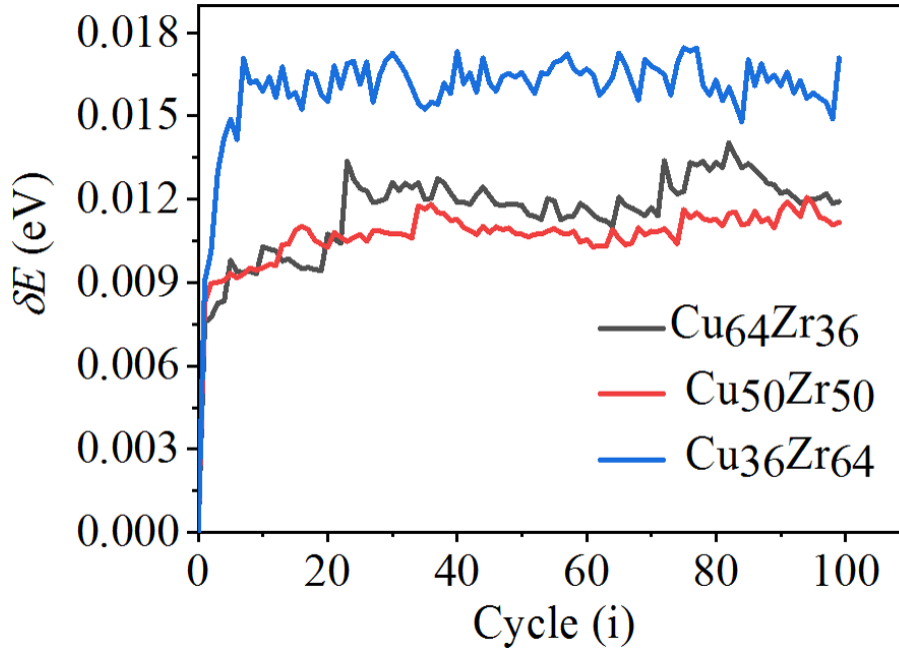


Figure 5.15: Variation of PE for the three compositions as a function of the number of thermal cycles.

atoms $D_{min}^2 > 100\text{\AA}^2$ with the number of cycles is much higher for $\text{Cu}_{36}\text{Zr}_{64}$, compared to $\text{Cu}_{64}\text{Zr}_{36}$ and $\text{Cu}_{50}\text{Zr}_{50}$. In other words, the atomic mobility is more significantly improved with the $\text{Cu}_{36}\text{Zr}_{64}$ system, which contain less Cu.

The stress-strain curves obtained from quasi-static shear deformation at 0.1 K with samples previously submitted or not to a complete thermal cycling (100 cycles) are shown in Figure 5.17. Furthermore, the deduced shear modulus, yielding stress and flow stress are reported in Figure 5.18. All of them decrease after thermal cycling except for the flow stress for which the decreasing trend is not obvious (partly due to the large uncertainty for its value). Thus, thermal cycling of the different Cu-Zr MGs compositions is responsible for a softening effect that is helpful for their plastic deformation.

Table 5.1: Yield and flow stress, in quasi static shear test at 0.1 K, for the three compositions submitted or not to thermal cycling.

Composition		$\text{Cu}_{64}\text{Zr}_{36}$	$\text{Cu}_{50}\text{Zr}_{50}$	$\text{Cu}_{36}\text{Zr}_{64}$
$\Delta\tau(\text{GPa})$	Without thermal cycling	0.88497	0.51827	0.57255
	With thermal cycling	0.61871	0.47711	0.26941

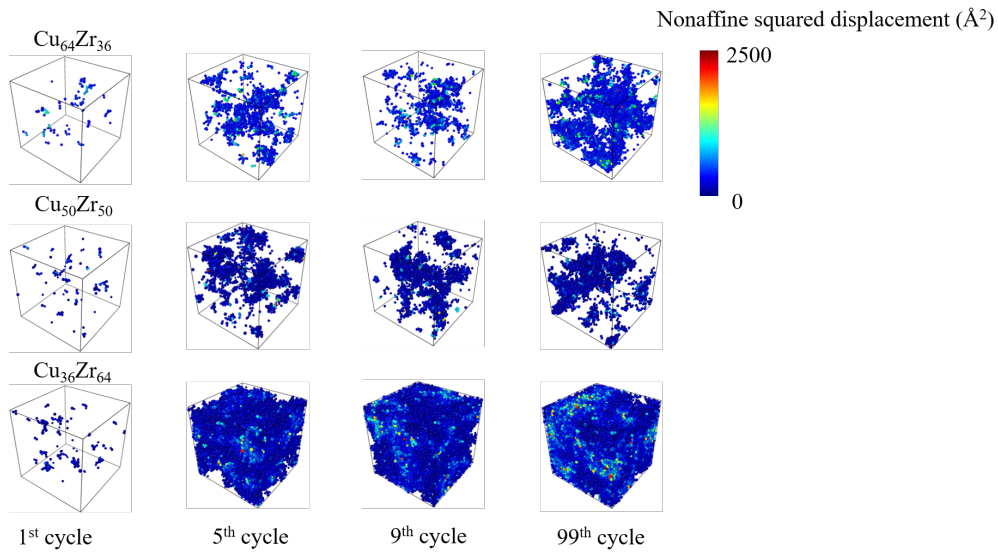


Figure 5.16: Map of the distribution of the non-affine square displacement ($D_{min}^2 > 100\text{\AA}^2$) at the 1st, 5th, 9th and 99th cycle, which the previous cycle is the reference for the three studied compositions.

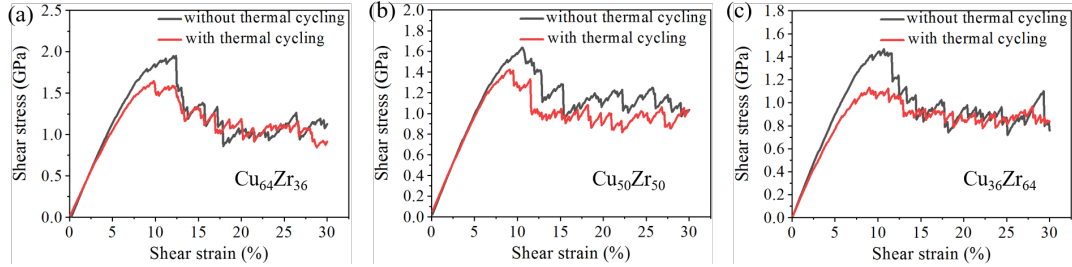


Figure 5.17: Stress-strain curves in quasi static shear for the three compositions previously submitted or not to the complete thermal cycling.

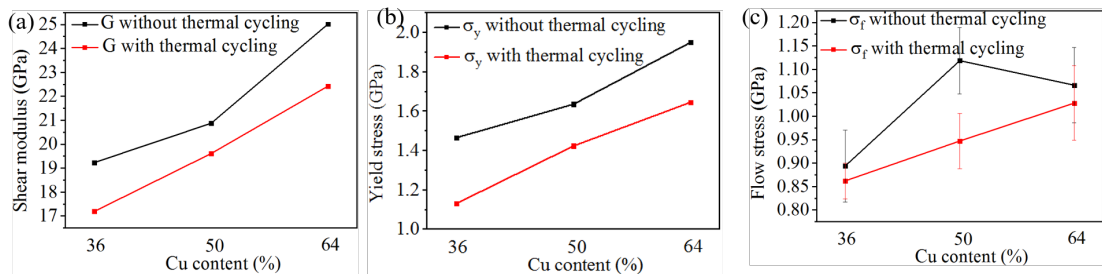


Figure 5.18: Shear modulus G (a), yield stress σ_y (b) and flow stress σ_f (c) deduced from Figure 5.17.

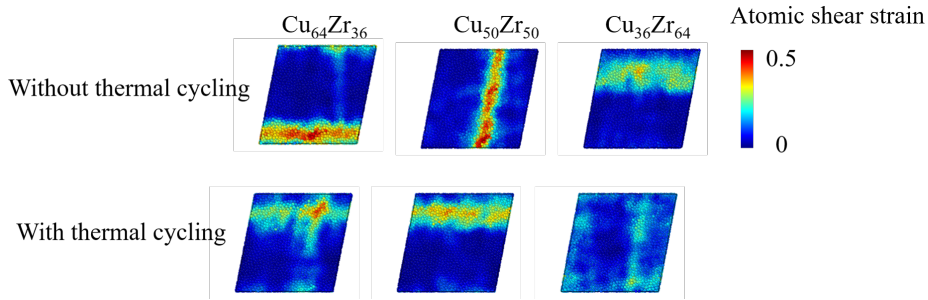


Figure 5.19: Map of the atomic shear strain in the three compositions previously submitted or not to thermal cycling, at 20 % shear strain.

Moreover, we compared the effect of thermal cycling on the difference between yield and flow stresses, $\Delta\tau = \sigma_y - \sigma_f$. As reported in Table 5.1, after thermal cycling, the stress drops compositions are smaller for the three tested composition. This corresponds to less localization of the STZs [Feng et al., 2015], as shown in Figure 5.19. We also compared the relative decrease in the shear modulus (γ_G), in the yielding strain (γ_{σ_y}) and in the difference between yielding and flow stress ($\gamma_{\Delta\tau}$) for the three compositions after thermal cycling. As seen in Table 5.2 all are larger for $Cu_{36}Zr_{64}$, which further confirms that the rejuvenation effect of thermal cycling is more important for this MG.

Table 5.2: Relative decrease in shear modulus, yield stress and in the difference between yield and flow stress for the three compositions after thermal cycling.

Composition	$Cu_{64}Zr_{36}$	$Cu_{50}Zr_{50}$	$Cu_{36}Zr_{64}$
γ_G (%)	10.36	6.05	10.60
γ_{σ_y} (%)	15.61	12.98	22.84
$\gamma_{\Delta\tau}$ (%)	30.09	7.94	52.95

Figure 5.20 and 5.21 present the cumulative number and cumulative plastic intensity of plastic events occurring during shear strain, as a function of the shear strain for the three compositions, before and after thermal cycling. It shows that thermal cycling treatment promotes more plastic events for $Cu_{64}Zr_{36}$ and maybe (it is a very slight effect) for $Cu_{36}Zr_{64}$. Conversely, for $Cu_{50}Zr_{50}$, cumulative number of plastic events is decreased after thermal cycling.

The number and plastic intensity of plastic events at each strain for the three compositions before and after thermal cycling are presented in Figure 5.22 and 5.23. The curves are smoothed for an easier comparison. In the small strain region (shown by an or-

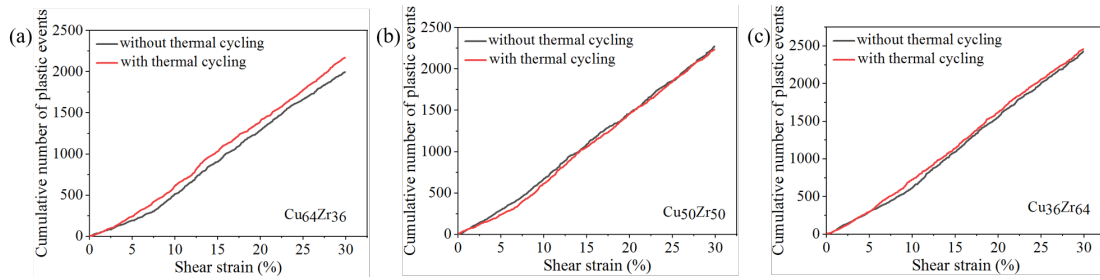


Figure 5.20: Cumulative number of plastic events for each compositions submitted or not thermal cycling.

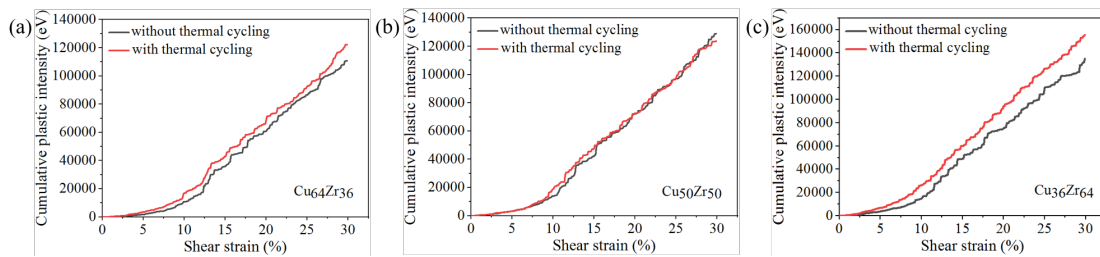


Figure 5.21: Cumulative plastic intensity for each composition submitted or not to thermal cycling.

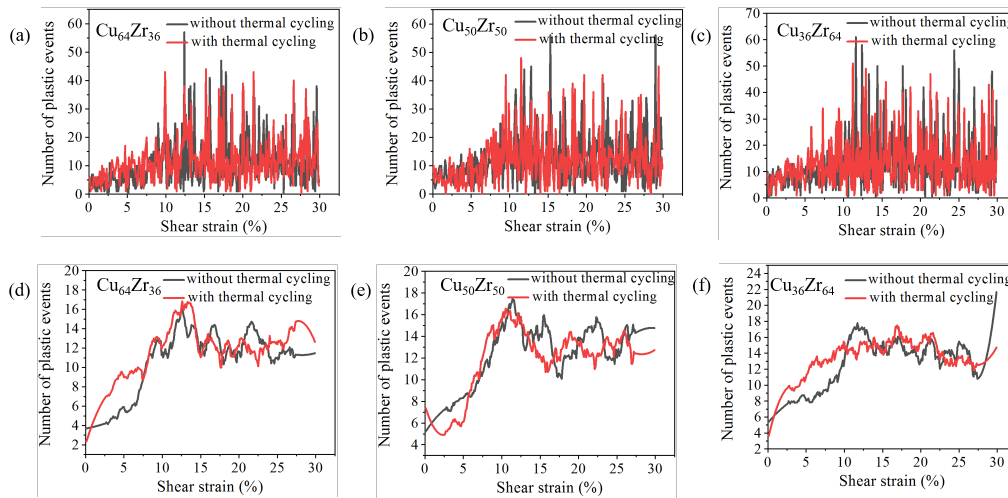


Figure 5.22: Number of plastic events as a function of the shear strain, for each compositions submitted or not to thermal cycling (original curves (a)-(c) and smoothed curves (d)-(f)).

ange circle), i.e. before yielding, the number of plastic events increase for $Cu_{64}Zr_{36}$ and $Cu_{36}Zr_{64}$ MG after thermal cycling, more for the latter. Whereas, for $Cu_{50}Zr_{50}$, they decrease.

The orientation distributions (more exactly their gaussian fit) of the plastic events oc-

5.4. EFFECT OF THERMAL CYCLING FOR DIFFERENT METALLIC GLASS COMPOSITION

curing over the whole shear test (strain up to 30 %) are reported for each composition (submitted or not to thermal treatment) on Figure 5.24 and the width of these distribution are reported in Table 5.3. The effect of thermal cycling on these distributions is very weak. The one for $Cu_{36}Zr_{64}$ is very slightly more uniform after thermal cycling, maybe consistent with the less localized distribution of the plastic events after thermal cycling for this system.

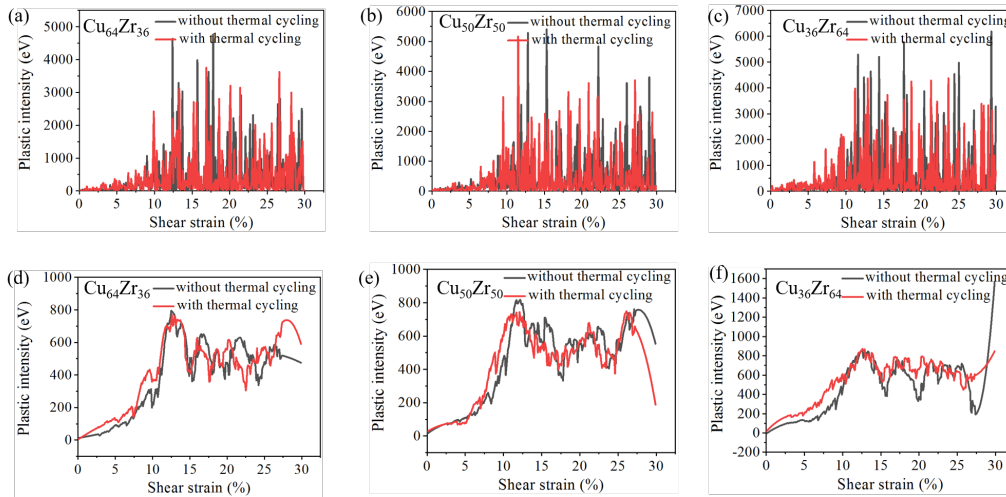


Figure 5.23: Plastic intensity of plastic events as a function of the shear strain for each composition before and after thermal cycling (original curves (a)-(c) and smoothed ones (d)-(f)).

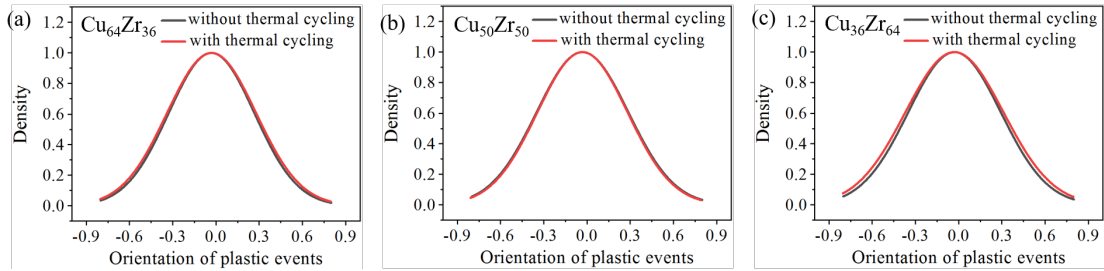


Figure 5.24: Orientation distribution (gaussian fit) of the plastics events occurring over the whole shearing test for each composition before and after thermal cycling.

Table 5.3: Width of the orientation distribution of the plastic events and relative variation deduced from Figure 5.24.

Composition	$Cu_{64}Zr_{36}$	$Cu_{50}Zr_{50}$	$Cu_{36}Zr_{64}$
Width without thermal cycling	0.2976	0.3186	0.3214
Width with thermal cycling	0.3095	0.3130	0.3405
Increased percentage (%)	4.00	-1.76	5.94

5.5 Discussion and conclusion

In this chapter, we analyze the effect of thermal cycling treatment on different compositions of Cu-Zr metallic glasses (MGs) or on one composition initially prepared with different quenching rates. Thermal cycling increases the potential energy (PE) and atomic mobility of $Cu_{64}Zr_{36}$ MG prepared with quenching rates of 10^{10} K/s and 10^{11} K/s and do the opposite for quenching rates of 10^{13} K/s and 10^{14} K/s. For $Cu_{64}Zr_{36}$ MG quenched at 10^{12} K/s, the difference is slight, and the thermal cycling has almost no consequences. Thus, we can conclude that the thermal treatment studied has a rejuvenation effect on the most relaxed $Cu_{64}Zr_{36}$ MGs and an aging effect on the less-relaxed ones. During quasi-static shear deformation, this results in a decrease in the shear modulus, yielding stress and stress drop for the most relaxed MGs, and the opposite for the less relaxed materials. For the lowest quenching rate 10^{10} K/s (for which the rejuvenation effect is the largest) the average size, number and plastic intensity of the plastic events occurring during shear (up to the yield strain) increase after thermal cycling, and they are more uniform. Thus, thermal cycling improves the deformation homogeneity. On the opposite, for the largest quenching rate (for which the aging effect is the largest) , the opposite is observed, and as a result the deformation is more localized. Regarding the effect of thermal cycling on different compositions of initially quenched at 10^{11} K/s, we found that the increase of PE due to the thermal cycling is larger for the composition with the largest Cu content. Moreover, after thermal cycling, the atomic mobility of $Cu_{36}Zr_{64}$, i.e., the sample with the lowest Cu content, increases significantly and the shear modulus, yield stress and stress drop calculated in quasi static shear test decrease the most. At last, thermal cycling increases the number and intensity of the plastic events occurring during shear for both compositions $Cu_{64}Zr_{36}$ and $Cu_{36}Zr_{64}$, whereas it decreases them for $Cu_{50}Zr_{50}$.

Conclusions and Perspectives

Conclusion

In this thesis, we investigated the factors affecting the plasticity of Cu-Zr binary metallic glasses (MGs) through molecular dynamics (MD) simulations, explored the parameters which can improve the plasticity of MGs, and analyzed their effect at the microscopic scale to establish the link between microscopic plasticity and mechanical properties of MGs.

By studying the effects of quenching rate, compositions, strain rate, and temperature on the plasticity of MGs, we obtained the following conclusions: In terms of microstructure, higher quenching rates, less Cu content in Cu-Zr binary MGs and higher temperatures can reduce the atomic packing density and the initial fraction of $\langle 0,0,12,0 \rangle$ icosahedra (full-icosahedra, FI) of MGs. Concerning mechanical properties, Cu-Zr binary MGs with higher quenching rate, less Cu content, and higher temperature leads to relatively smaller shear modulus, yield stress, and stress drop after quasi-static shear deformation. Furthermore, their FI drops are less pronounced during the deformation. By comparing the local atomic shear strain maps, their deformation is less localized. Hence, a higher quenching rate, less Cu content, and higher temperature are beneficial for the plasticity of MGs. The strain rate effect on the microstructure and mechanical properties of MGs is slight at low temperatures, while its effect on the mechanical properties of MGs is more pronounced at temperatures close to the glass transition temperature (T_g). At higher strain rates, the deformation of MGs is slightly less localized.

We also analyzed the effects of quenching rate and composition on the number, intensity, and average size of plastic events for Cu-Zr binary MGs at the microscopic scale and ob-

tained the following conclusions:

More and larger plastic events with higher plastic intensity are activated before the yield point for MGs prepared with higher quenching rates. This also leads to smaller shear moduli. When the yield point is reached, there is a significant increase in the plastic intensity of plastic events for MGs prepared with a low quenching rate, while for higher quenching rates, the increase is less pronounced, corresponding to less localized deformation. In addition, the plastic events are distributed more uniformly for MGs with higher quenching rates.

Moreover, with the decrease of the Cu content, more plastic events occur below the yield point (their intensity and their size are similar for all the Cu content), and above the yield point, the plastic intensity and the average size seems to fluctuate more.

We also investigated the effect of thermal cycling below T_g on MGs prepared with different quenching rates and compositions, in particular we analyzed the plastic events occurring during their deformation.

Thermal cycling has a rejuvenation effect for MGs with low quenching rates, and when the quenching rate is lower, the rejuvenation effect is more significant. This rejuvenation causes an increase in the number, plastic intensity, and average size of plastic events. Conversely, for MGs prepared with higher quenching rates, there is an aging effect, and this one is more pronounced when the quenching rate is higher. Indeed, in this case, the number, average size and plastic intensity of the plastic events decrease.

Finally, the rejuvenation effect obtained for systems prepared with low quenching rate is more important for the lowest Cu content.

In terms of the relationship between the characteristics of microscopic plastic events and macroscopic plasticity, we can also conclude that when the number, plastic intensity, and average size of plastic events are larger and their distribution is more uniform, MGs experience less localization and more uniform plastic deformation at the macroscopic scale.

Perspectives

Our analysis of microscale plastic events is currently available only for quasi-static shear and tensile deformation. We have attempted a reconstruction of the stress-strain curve

Conclusions and Perspectives

for quasi-static tensile deformation using Eshelby's inclusion model. However, this reconstruction is not correct. All the atomic displacements of plastic events being fitted simultaneously at each strain step a large number of plastic events with very high plastic intensity are detected during tensile deformation, resulting in the interaction of plastic events and a poor quality of the atomic displacement fitting. We will try to optimize the fitting of the stress-strain curve by adjusting the relevant fitting parameters.

In addition, we have not yet analyzed the plastic events of MGs after dynamic deformation. This would enable a better understanding of the influence of the strain rate. Moreover, by dynamically deforming the system in the forward and in the backward directions it will be possible to separate the plastic component of the stress from the an elastic part (i.e., the reversible component of the stress) and estimate thus the contribution of these two components. Eventually, we could also compare our results on the characterization of the plastic events to analytical models of visco-elasto-plasticity in amorphous materials, such as the quasi-point defect model of Perez et al., and make some conclusions about the validity of this kind of modelling which is based on physical assumptions not easily ascertainable.

As for the cryogenic treatment to improve plasticity, it would be interesting to perform a more systematic study on the influence of the temperature and of the annealing time on the degree of rejuvenation of the system. Moreover, the link between the local thermal heterogeneities and the internal stresses causing irreversible local atomic rearrangements, and thus enhanced mobility, has to be further explored.

Author's publications

- 17th International Conference on Liquids and Amorphous Metals, 2019 (poster)
- A paper in preparation: M. Liang, T. Albaret, J. Morthomas, L. Chazeau, C. Fusco, Characterization of shear transformations and prediction of the mechanical behavior of a metallic glass by Eshelby's inclusion model. Physical Review E

Appendix

Appendix A

Smoothing method

Comparison of the effect of the different compositions or quenching rates on the evolution of the size, intensity and number of the plastic events with the strain is difficult due to large scattering of the data (as shown in Figure A.1). For this reason, we use a smoothing procedure. Origin software provides several methods to do it, including Savitzky-Golay filter method, adjacency averaging, percentile filtering, FFT filtering, LOWESS and LOESS smoothing methods, and binomial filter.

With the Savitzky-Golay (SG) filter method, each data point receives a new smoothed value after a local polynomial regression is conducted around it. Because it tends to preserve data properties like peak height and width that can be "washed out" by adjacency averaging, this approach is superior to adjacency averaging. Increasing the "window size" or the quantity of data points used in each local regression (using the "window points" option) will smooth out the results. The overall profile can still be preserved with Savitzky-Golay even for very large window sizes, where adjacency averaging may deviate too far from the input signal. Adjacency averaging, as the name suggests, effectively replaces each point in the data with the new average by averaging a user-specified number of data points around each point in the data. The 50 % percentile filtering (or median filtering) method might be most effective for signals with distributed grain noise when the noise displays local spikes. The median value of a group of nearby points is used instead of the signal value at each point in this method. The FFT filtering method can be applied if the signal contains high frequency noise. The genuine signal is left after the

filter eliminates all high frequency noise.

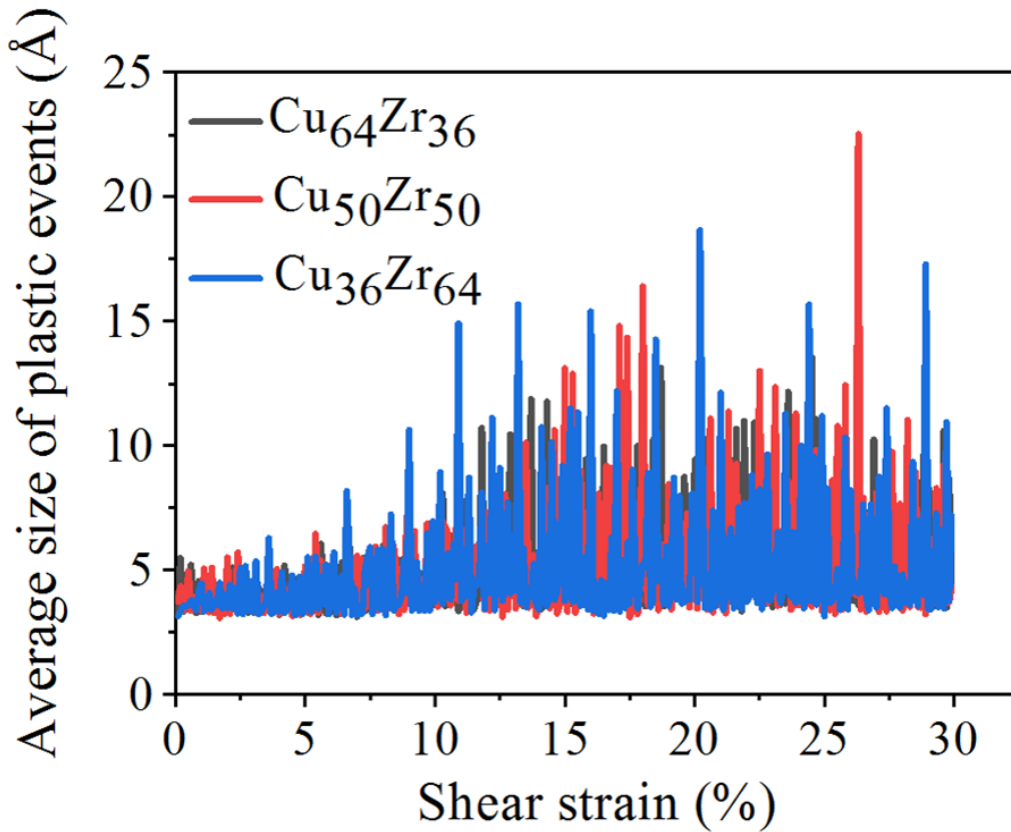


Figure A.1: Average size of plastic events as a function of shear strain for the three compositions with a quenching rate of 10^{11} K/s (initial data).

When there are a lot of data points present, the LOWESS and LOESS smoothing methods are highly helpful for directly detecting in noisy data. A weighted moving average filter with weights derived from binomial coefficients is known as a binomial filter, a low-pass filter that can eliminate high frequency noise.

In our case, we wanted to preserve more features of the data, so we choose the SG filter method. Then, we have tested different sets of points window, including 5, 10, 20 and 50. From Figure A.2, we can see that the smallest points window can retain more features of the original data, but the curve still has a lot of noise, which affects the comparison effect. To make the comparison more distinct, we therefore use the 50 window points, as shown in Figure A.3.

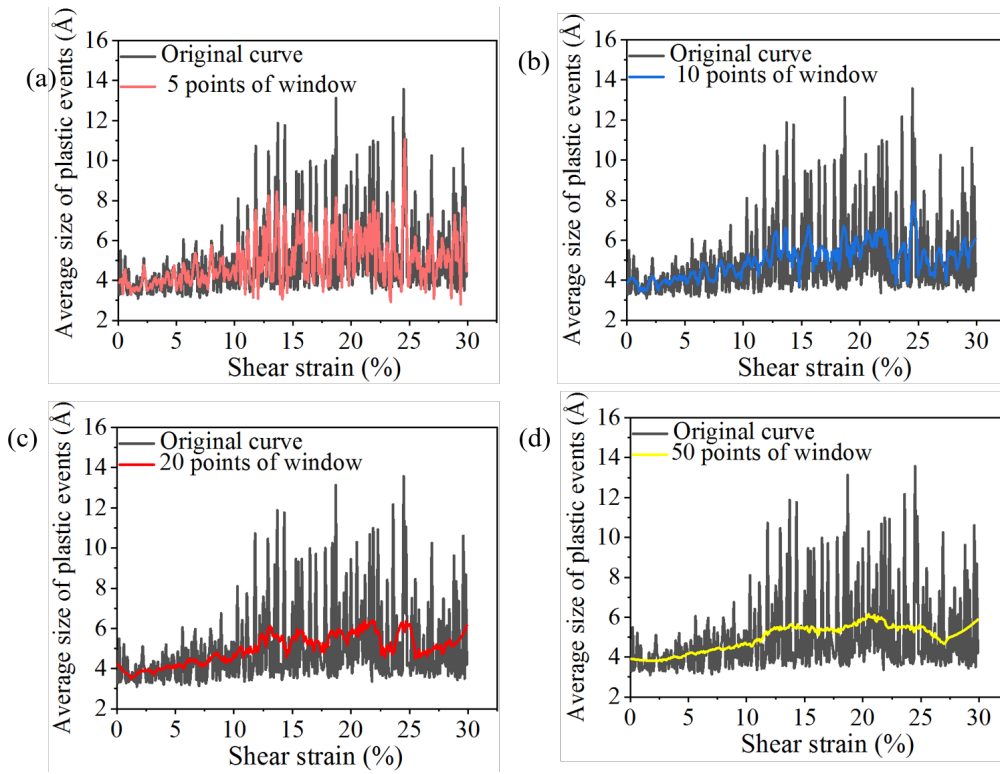


Figure A.2: Different points window of SG filter method when smoothing the curve of average size of plastic events with shear strain of $\text{Cu}_{64}\text{Zr}_{36}$ MG with a quenching rate of 10^{11} K/s.

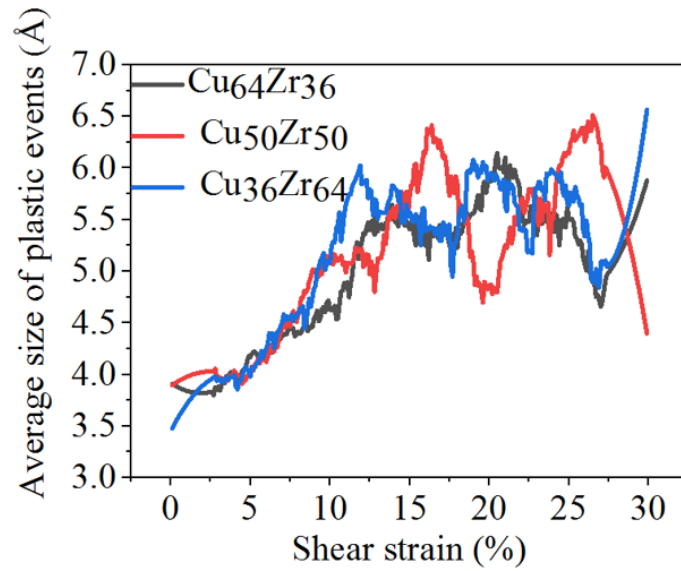


Figure A.3: Curves in Figure A.1 after smoothing with 50 points of window.

Bibliography

- [Albaret et al., 2016] Albaret, T., Tanguy, A., Boioli, F., and Rodney, D. (2016). Mapping between atomistic simulations and eshelby inclusions in the shear deformation of an amorphous silicon model. *Physical Review E*, 93(5):053002.
- [Albe et al., 2013] Albe, K., Ritter, Y., and Şopu, D. (2013). Enhancing the plasticity of metallic glasses: Shear band formation, nanocomposites and nanoglasses investigated by molecular dynamics simulations. *Mechanics of Materials*, 67:94–103.
- [Allen and Tildesley, 2017] Allen, M. P. and Tildesley, D. J. (2017). *Computer simulation of liquids*. Oxford university press.
- [Argon, 1979] Argon, A. (1979). Plastic deformation in metallic glasses. *Acta metallurgica*, 27(1):47–58.
- [Ashcroft and Mermin,] Ashcroft, N. and Mermin, N. Solid state physics, 1976. *Cornell University*.
- [Beeman, 1976] Beeman, D. (1976). Some multistep methods for use in molecular dynamics calculations. *Journal of computational physics*, 20(2):130–139.
- [Bei et al., 2006] Bei, H., Xie, S., and George, E. P. (2006). Softening caused by profuse shear banding in a bulk metallic glass. *Physical review letters*, 96(10):105503.
- [Berendsen et al., 1984] Berendsen, H. J., Postma, J. v., Van Gunsteren, W. F., DiNola, A., and Haak, J. R. (1984). Molecular dynamics with coupling to an external bath. *The Journal of chemical physics*, 81(8):3684–3690.

- [Bernal, 1960a] Bernal, J. (1960a). Geometry of the structure of monatomic liquids. *Nature*, 185(4706):68–70.
- [Bernal, 1960b] Bernal, J. D. (1960b). The structure of liquids. *Scientific American*, 203(2):124–137.
- [Bian et al., 2001] Bian, Z., Chen, G., He, G., and Hui, X. (2001). Microstructure and ductile–brittle transition of as-cast zr-based bulk glass alloys under compressive testing. *Materials Science and Engineering: A*, 316(1-2):135–144.
- [Bitzek et al., 2006] Bitzek, E., Koskinen, P., Gähler, F., Moseler, M., and Gumbsch, P. (2006). Structural relaxation made simple. *Physical review letters*, 97(17):170201.
- [Bower, 2009] Bower, A. F. (2009). *Applied mechanics of solids*. CRC press.
- [Bulatov and Argon, 1994] Bulatov, V. and Argon, A. (1994). A stochastic model for continuum elasto-plastic behavior. i. numerical approach and strain localization. *Modelling and Simulation in Materials Science and Engineering*, 2(2):167.
- [Cao et al., 2009] Cao, A., Cheng, Y., and Ma, E. (2009). Structural processes that initiate shear localization in metallic glass. *Acta Materialia*, 57(17):5146–5155.
- [Cargill III, 1975] Cargill III, G. (1975). Structure of metallic alloy glasses. *Solid state physics*, 30:227–320.
- [Chadha et al., 1981] Chadha, G., Cowlam, N., Davies, H., and Donald, I. (1981). A diffraction study of ni₈₂b₁₈ and ni₆₄b₃₆ metallic glasses. *Journal of Non-Crystalline Solids*, 44(2-3):265–276.
- [Challis and Sheard, 2003] Challis, L. and Sheard, F. (2003). The green of green functions. *Physics Today*, 56(12):41–46.
- [Chen et al., 2012] Chen, B., Li, Y., Yi, M., Li, R., Pang, S., Wang, H., and Zhang, T. (2012). Optimization of mechanical properties of bulk metallic glasses by residual stress adjustment using laser surface melting. *Scripta Materialia*, 66(12):1057–1060.

- [Chen et al., 2008] Chen, L., Fu, Z., Zhang, G., Hao, X., Jiang, Q., Wang, X., Cao, Q., Franz, H., Liu, Y., Xie, H., et al. (2008). New class of plastic bulk metallic glass. *Physical review letters*, 100(7):075501.
- [Chen, 2008] Chen, M. (2008). Mechanical behavior of metallic glasses: microscopic understanding of strength and ductility. *Annu. Rev. Mater. Res.*, 38:445–469.
- [Chen et al., 2020] Chen, S., Li, T., Chang, W., Yang, H., Zhang, J., Tang, H., Feng, S., Wu, F., and Wu, Y. (2020). On the formation of shear bands in a metallic glass under tailored complex stress fields. *Journal of Materials Science & Technology*, 53:112–117.
- [Chen et al., 2011] Chen, Y., Jiang, M., Wei, Y., and Dai, L. (2011). Failure criterion for metallic glasses. *Philosophical Magazine*, 91(36):4536–4554.
- [Cheng et al., 2009a] Cheng, Y., Cao, A., and Ma, E. (2009a). Correlation between the elastic modulus and the intrinsic plastic behavior of metallic glasses: The roles of atomic configuration and alloy composition. *Acta Materialia*, 57(11):3253–3267.
- [Cheng et al., 2008a] Cheng, Y., Cao, A. J., Sheng, H., and Ma, E. (2008a). Local order influences initiation of plastic flow in metallic glass: Effects of alloy composition and sample cooling history. *Acta Materialia*, 56(18):5263–5275.
- [Cheng and Ma, 2008] Cheng, Y. and Ma, E. (2008). Indicators of internal structural states for metallic glasses: Local order, free volume, and configurational potential energy. *Applied Physics Letters*, 93(5):051910.
- [Cheng and Ma, 2011] Cheng, Y. and Ma, E. (2011). Atomic-level structure and structure–property relationship in metallic glasses. *Progress in materials science*, 56(4):379–473.
- [Cheng et al., 2009b] Cheng, Y., Ma, E., and Sheng, H. (2009b). Atomic level structure in multicomponent bulk metallic glass. *Physical review letters*, 102(24):245501.
- [Cheng et al., 2008b] Cheng, Y., Sheng, H., and Ma, E. (2008b). Relationship between structure, dynamics, and mechanical properties in metallic glass-forming alloys. *Physical Review B*, 78(1):014207.

- [Cohen and Turnbull, 1959] Cohen, M. H. and Turnbull, D. (1959). Molecular transport in liquids and glasses. *The Journal of Chemical Physics*, 31(5):1164–1169.
- [Concustell et al., 2009] Concustell, A., Méar, F., Surinach, S., Baró, M., and Greer, A. (2009). Structural relaxation and rejuvenation in a metallic glass induced by shot-peening. *Philosophical Magazine Letters*, 89(12):831–840.
- [Conner et al., 2003] Conner, R., Johnson, W. L., Paton, N., and Nix, W. (2003). Shear bands and cracking of metallic glass plates in bending. *Journal of applied physics*, 94(2):904–911.
- [Dai et al., 2005] Dai, L., Yan, M., Liu, L., and Bai, Y. (2005). Adiabatic shear banding instability in bulk metallic glasses. *Applied Physics Letters*, 87(14):141916.
- [Dasgupta et al., 2012] Dasgupta, R., Hentschel, H. G. E., and Procaccia, I. (2012). Microscopic mechanism of shear bands in amorphous solids. *Physical review letters*, 109(25):255502.
- [Daw and Baskes, 1983] Daw, M. S. and Baskes, M. I. (1983). Semiempirical, quantum mechanical calculation of hydrogen embrittlement in metals. *Physical review letters*, 50(17):1285.
- [Daw and Baskes, 1984] Daw, M. S. and Baskes, M. I. (1984). Embedded-atom method: Derivation and application to impurities, surfaces, and other defects in metals. *Physical Review B*, 29(12):6443.
- [Daw et al., 1993] Daw, M. S., Foiles, S. M., and Baskes, M. I. (1993). The embedded-atom method: a review of theory and applications. *Materials Science Reports*, 9(7-8):251–310.
- [Debenedetti and Stillinger, 2001] Debenedetti, P. G. and Stillinger, F. H. (2001). Supercooled liquids and the glass transition. *Nature*, 410(6825):259–267.
- [Ding et al., 2014a] Ding, J., Cheng, Y.-Q., and Ma, E. (2014a). Full icosahedra dominate local order in cu₆₄zr₃₄ metallic glass and supercooled liquid. *Acta materialia*, 69:343–354.

- [Ding et al., 2014b] Ding, J., Patinet, S., Falk, M. L., Cheng, Y., and Ma, E. (2014b). Soft spots and their structural signature in a metallic glass. *Proceedings of the National Academy of Sciences*, 111(39):14052–14056.
- [Dutta et al., 2018] Dutta, T., Chauniyal, A., Singh, I., Narasimhan, R., Thamburaja, P., and Ramamurty, U. (2018). Plastic deformation and failure mechanisms in nano-scale notched metallic glass specimens under tensile loading. *Journal of the Mechanics and Physics of Solids*, 111:393–413.
- [Dziegielewski et al., 2020] Dziegielewski, P., Mathon, O., Kantor, I., Pascarelli, S., Shinmei, T., Irifune, T., and Antonowicz, J. (2020). High pressure atomic structure of zr-cu metallic glass via exafs spectroscopy and molecular dynamics simulations. *High Pressure Research*, 40(1):54–64.
- [Ediger et al., 1996] Ediger, M. D., Angell, C. A., and Nagel, S. R. (1996). Supercooled liquids and glasses. *The journal of physical chemistry*, 100(31):13200–13212.
- [Egami et al., 2013] Egami, T., Iwashita, T., and Dmowski, W. (2013). Mechanical properties of metallic glasses. *Metals*, 3(1):77–113.
- [Eidel et al., 2011] Eidel, B., Stukowski, A., and Schröder, J. (2011). Energy-minimization in atomic-to-continuum scale-bridging methods. *PAMM*, 11(1):509–510.
- [Eshelby, 1957] Eshelby, J. D. (1957). The determination of the elastic field of an ellipsoidal inclusion, and related problems. *Proceedings of the royal society of London. Series A. Mathematical and physical sciences*, 241(1226):376–396.
- [Falk and Langer, 1998] Falk, M. L. and Langer, J. S. (1998). Dynamics of viscoplastic deformation in amorphous solids. *Physical Review E*, 57(6):7192.
- [Feng et al., 2018] Feng, S., Chan, K., Zhao, L., Pan, S., Qi, L., Wang, L., and Liu, R. (2018). Rejuvenation by weakening the medium range order in zr46cu46al8 metallic glass with pressure preloading: A molecular dynamics simulation study. *Materials & Design*, 158:248–255.

- [Feng et al., 2020] Feng, S., Li, L., Chan, K., Zhao, L., Wang, L., and Liu, R. (2020). Enhancing strength and plasticity by pre-introduced indent-notches in zr36cu64 metallic glass: A molecular dynamics simulation study. *Journal of Materials Science & Technology*, 43:119–125.
- [Feng et al., 2015] Feng, S., Qi, L., Zhao, F., Pan, S., Li, G., Ma, M., and Liu, R. (2015). A molecular dynamics analysis of internal friction effects on the plasticity of zr65cu35 metallic glass. *Materials & Design*, 80:36–40.
- [Finney, 1970] Finney, J. (1970). Random packings and the structure of simple liquids. i. the geometry of random close packing. *Proceedings of the Royal Society of London. A. Mathematical and Physical Sciences*, 319(1539):479–493.
- [Finnis and Sinclair, 1984] Finnis, M. and Sinclair, J. (1984). A simple empirical n-body potential for transition metals. *Philosophical Magazine A*, 50(1):45–55.
- [Flores et al., 2002] Flores, K., Suh, D., Dauskardt, R., Asoka-Kumar, P., Sterne, P., and Howell, R. (2002). Characterization of free volume in a bulk metallic glass using positron annihilation spectroscopy. *Journal of materials research*, 17(5):1153–1161.
- [Foroughi et al., 2016] Foroughi, A., Tavakoli, R., and Aashuri, H. (2016). Molecular dynamics study of structural formation in cu50–zr50 bulk metallic glass. *Journal of Non-Crystalline Solids*, 432:334–341.
- [Frank, 1952] Frank, F. C. (1952). Supercooling of liquids. *Proceedings of the Royal Society of London. Series A. Mathematical and Physical Sciences*, 215(1120):43–46.
- [Fu et al., 2013] Fu, W., Sun, Y., and Zhang, W. (2013). The effect of cooling rate on microstructure and mechanical properties of zr-based bulk metallic glasses. *Advances in Materials Science and Engineering*, 2013.
- [Fu et al., 2007] Fu, X., Li, Y., and Schuh, C. (2007). Temperature, strain rate and reinforcement volume fraction dependence of plastic deformation in metallic glass matrix composites. *Acta materialia*, 55(9):3059–3071.

- [Fukunaga and Suzuki, 1980] Fukunaga, T. and Suzuki, K. (1980). An experimental derivation of partial structure functions of amorphous pd 80 si 20 alloy using combination of x-ray, electron and neutron diffraction experiments. *Science Reports of the Research Institutes, Tohoku University, Series A*, 28(2):208–217.
- [Fusco et al., 2010] Fusco, C., Albaret, T., and Tanguy, A. (2010). Role of local order in the small-scale plasticity of model amorphous materials. *Physical Review E*, 82(6):066116.
- [Fusco et al., 2014] Fusco, C., Albaret, T., and Tanguy, A. (2014). Rheological properties vs. local dynamics in model disordered materials at low temperature. *The European Physical Journal E*, 37(5):1–9.
- [Gaskell, 1978] Gaskell, P. (1978). A new structural model for transition metal–metalloid glasses. *Nature*, 276(5687):484–485.
- [Gaskell, 1979a] Gaskell, P. (1979a). A new structural model for amorphous transition metal silicides, borides, phosphides and carbides. *Journal of non-crystalline solids*, 32(1-3):207–224.
- [Gaskell, 1979b] Gaskell, P. (1979b). On the structure of simple inorganic amorphous solids. *Journal of Physics C: Solid State Physics*, 12(21):4337.
- [Gear, 1971] Gear, C. W. (1971). Numerical initial value problems in ordinary differential equations. *Prentice-Hall series in automatic computation*.
- [Goldenberg and Goldhirsch, 2004] Goldenberg, C. and Goldhirsch, I. (2004). Small and large scale granular statics. *Granular Matter*, 6(2):87–96.
- [Greer et al., 2013] Greer, A., Cheng, Y., and Ma, E. (2013). Shear bands in metallic glasses. *Materials Science and Engineering: R: Reports*, 74(4):71–132.
- [Greer, 1995] Greer, A. L. (1995). Metallic glasses. *Science*, 267(5206):1947–1953.
- [Grell et al., 2018] Grell, D., Dabrock, F., and Kerscher, E. (2018). Cyclic cryogenic pre-treatments influencing the mechanical properties of a bulk glassy zr-based alloy. *Fatigue & Fracture of Engineering Materials & Structures*, 41(6):1330–1343.

- [Gu et al., 2002] Gu, X., Livi, K. J., and Hufnagel, T. C. (2002). Structure of shear bands in zirconium-based metallic glasses observed by transmission electron microscopy. *MRS Online Proceedings Library*, 754(1):1–6.
- [Guo et al., 2007] Guo, H., Yan, P., Wang, Y., Tan, J., Zhang, Z., Sui, M., and Ma, E. (2007). Tensile ductility and necking of metallic glass. *Nature materials*, 6(10):735–739.
- [Guo et al., 2011] Guo, S., Chan, K. C., and Liu, L. (2011). Notch toughness of fe-based bulk metallic glass and composites. *Journal of alloys and compounds*, 509(39):9441–9446.
- [Guo et al., 2018] Guo, W., Yamada, R., and Saida, J. (2018). Rejuvenation and plasticization of metallic glass by deep cryogenic cycling treatment. *Intermetallics*, 93:141–147.
- [Harmon et al., 2007] Harmon, J. S., Demetriou, M. D., Johnson, W. L., and Samwer, K. (2007). Anelastic to plastic transition in metallic glass-forming liquids. *Physical Review Letters*, 99(13):135502.
- [He et al., 2003] He, G., Zhang, Z., Löser, W., Eckert, J., and Schultz, L. (2003). Effect of ta on glass formation, thermal stability and mechanical properties of a zr52. 25cu28. 5ni4. 75al9. 5ta5 bulk metallic glass. *Acta materialia*, 51(8):2383–2395.
- [Heerman, 1987] Heerman, D. (1987). Computer simulation methods in theoretical physics. *Applied Optics*, 26(10):1818.
- [Hockney, 1970] Hockney, R. W. (1970). The potential calculation and some applications. *Methods Comput. Phys.*, 9:136.
- [Hohenberg and Kohn, 1964] Hohenberg, P. and Kohn, W. (1964). Inhomogeneous electron gas. *Physical review*, 136(3B):B864.
- [Homer et al., 2010] Homer, E. R., Rodney, D., and Schuh, C. A. (2010). Kinetic monte carlo study of activated states and correlated shear-transformation-zone activity during the deformation of an amorphous metal. *Physical Review B*, 81(6):064204.
- [Hoover, 2012] Hoover, W. G. (2012). *Computational statistical mechanics*. Elsevier.

- [Huang et al., 2002] Huang, R., Suo, Z., Prevost, J., and Nix, W. (2002). Inhomogeneous deformation in metallic glasses. *Journal of the Mechanics and Physics of Solids*, 50(5):1011–1027.
- [Huang et al., 2014] Huang, Y., Fan, H., Wang, D., Sun, Y., Liu, F., Shen, J., Sun, J., and Mi, J. (2014). The effect of cooling rate on the wear performance of a zrcualag bulk metallic glass. *Materials & Design*, 58:284–289.
- [Hufnagel, 2015] Hufnagel, T. C. (2015). Metallic glasses: Cryogenic rejuvenation. *Nature Materials*, 14(9):867–868.
- [Inoue, 2000] Inoue, A. (2000). Stabilization of metallic supercooled liquid and bulk amorphous alloys. *Acta materialia*, 48(1):279–306.
- [Inoue and Shen, 2006] Inoue, A. and Shen, B. (2006). Formation and applications of bulk glassy alloys in late transition metal base system. In *AIP Conference Proceedings*, volume 832, pages 11–20. American Institute of Physics.
- [Jagla, 2007] Jagla, E. (2007). Strain localization driven by structural relaxation in sheared amorphous solids. *Physical Review E*, 76(4):046119.
- [Jiang et al., 2009] Jiang, F., Zhao, Y., Zhang, L., Pan, S., Zhou, Y., He, L., and Sun, J. (2009). Dependence of ductility on free volume in a cu-zr-based metallic glass. *Advanced Engineering Materials*, 11(3):177–181.
- [Jiang and Dai, 2009] Jiang, M. and Dai, L. (2009). On the origin of shear banding instability in metallic glasses. *Journal of the Mechanics and Physics of Solids*, 57(8):1267–1292.
- [Jiang and Dai, 2011] Jiang, M. and Dai, L. (2011). Shear-band toughness of bulk metallic glasses. *Acta Materialia*, 59(11):4525–4537.
- [Jiang et al., 2008] Jiang, M., Ling, Z., Meng, J., and Dai, L. (2008). Energy dissipation in fracture of bulk metallic glasses via inherent competition between local softening and quasi-cleavage. *Philosophical Magazine*, 88(3):407–426.

- [Jing et al., 1989] Jing, J., Krämer, A., Birringer, R., Gleiter, H., and Gonser, U. (1989). Modified atomic structure in a pd fe si nanoglass: A mössbauer study. *Journal of non-crystalline solids*, 113(2-3):167–170.
- [Johnson and Samwer, 2005] Johnson, W. and Samwer, K. (2005). A universal criterion for plastic yielding of metallic glasses with a $(T/T_g)^{2/3}$ temperature dependence. *Physical review letters*, 95(19):195501.
- [Johnson, 1999] Johnson, W. L. (1999). Bulk glass-forming metallic alloys: Science and technology. *MRS bulletin*, 24(10):42–56.
- [Ketov et al., 2015] Ketov, S., Sun, Y., Nachum, S., Lu, Z., Checchi, A., Beraldin, A., Bai, H., Wang, W., Louzguine-Luzgin, D., Carpenter, M., et al. (2015). Rejuvenation of metallic glasses by non-affine thermal strain. *Nature*, 524(7564):200–203.
- [Khonik et al., 2008] Khonik, S., Granato, A., Joncich, D., Pompe, A., and Khonik, V. (2008). Evidence of distributed interstitialcy-like relaxation of the shear modulus due to structural relaxation of metallic glasses. *Physical review letters*, 100(6):065501.
- [Kim et al., 2009] Kim, C. P., Suh, J.-Y., Wiest, A., Lind, M. L., Conner, R. D., and Johnson, W. L. (2009). Fracture toughness study of new zr-based be-bearing bulk metallic glasses. *Scripta materialia*, 60(2):80–83.
- [King et al., 2006] King, A., Steuwer, A., Woodward, C., and Withers, P. (2006). Effects of fatigue and fretting on residual stresses introduced by laser shock peening. *Materials Science and Engineering: A*, 435:12–18.
- [Kröner, 1990] Kröner, E. (1990). Modified green functions in the theory of heterogeneous and/or anisotropic linearly elastic media. In *Micromechanics and inhomogeneity*, pages 197–211. Springer.
- [Lamparter et al., 1982] Lamparter, P., Sperl, W., and Steeb, S. (1982). Atomic structure of amorphous metallic ni₈₁b₁₉. *Zeitschrift für Naturforschung A*, 37(11):1223–1234.
- [Leamy et al., 1972] Leamy, H., Wang, T., and Chen, H. (1972). Plastic flow and fracture of metallic glass. *Metallurgical and Materials Transactions B*, 3(3):699–708.

- [Lee et al., 2005] Lee, J.-C., Kim, Y.-C., Ahn, J.-P., and Kim, H. S. (2005). Enhanced plasticity in a bulk amorphous matrix composite: Macroscopic and microscopic viewpoint studies. *Acta materialia*, 53(1):129–139.
- [Lee et al., 2007] Lee, J.-C., Park, K.-W., Kim, K.-H., Fleury, E., Lee, B.-J., Wakeda, M., and Shibutani, Y. (2007). Origin of the plasticity in bulk amorphous alloys. *Journal of Materials Research*, 22(11):3087–3097.
- [Lee et al., 2011] Lee, M., Lee, C.-M., Lee, K.-R., Ma, E., and Lee, J.-C. (2011). Networked interpenetrating connections of icosahedra: Effects on shear transformations in metallic glass. *Acta Materialia*, 59(1):159–170.
- [Lewandowski* et al., 2005] Lewandowski*, J., Wang, W., and Greer, A. (2005). Intrinsic plasticity or brittleness of metallic glasses. *Philosophical Magazine Letters*, 85(2):77–87.
- [Li et al., 2012] Li, C., Kou, S., Zhao, Y., Liu, G., and Ding, Y. (2012). Effect of cooling rate on plastic deformation of zr-based bulk metallic glasses. *Progress in Natural Science: Materials International*, 22(1):21–25.
- [Li et al., 2014] Li, F., Liu, X., and Lu, Z. (2014). Atomic structural evolution during glass formation of a cu–zr binary metallic glass. *Computational materials science*, 85:147–153.
- [Li et al., 2002a] Li, J., Spaepen, F., and Hufnagel, T. (2002a). Nanometre-scale defects in shear bands in a metallic glass. *Philosophical Magazine A*, 82(13):2623–2630.
- [Li et al., 2002b] Li, J., Wang, Z. L., and Hufnagel, T. (2002b). Characterization of nanometer-scale defects in metallic glasses by quantitative high-resolution transmission electron microscopy. *Physical Review B*, 65(14):144201.
- [Li et al., 2021] Li, M., Guan, H., Yang, S., Ma, X., and Li, Q. (2021). Minor cr alloyed fe–co–ni–p–b high entropy bulk metallic glass with excellent mechanical properties. *Materials Science and Engineering: A*, 805:140542.
- [Li et al., 2017] Li, M., Jiang, M., Yang, S., Jiang, F., He, L., and Sun, J. (2017). Effect of strain rate on yielding strength of a zr-based bulk metallic glass. *Materials Science and Engineering: A*, 680:21–26.

- [Li et al., 2009] Li, M., Wang, C., Hao, S., Kramer, M., and Ho, K. (2009). Structural heterogeneity and medium-range order in $Zr_{100-x}Cu_x$ metallic glasses. *Physical Review B*, 80(18):184201.
- [Liang et al., 2014] Liang, Y.-C., Liu, R.-S., Mo, Y.-F., Liu, H.-R., Tian, Z.-A., Zhou, Q.-y., Zhang, H.-T., Zhou, L.-L., Hou, Z.-Y., and Peng, P. (2014). Influence of icosahedral order on the second peak splitting of pair distribution function for $Mg_{70}Zn_{30}$ metallic glass. *Journal of alloys and compounds*, 597:269–274.
- [Liu et al., 1998] Liu, C., Heatherly, L., Horton, J., Easton, D., Carmichael, C., Wright, J., Schneibel, J., Yoo, M., Chen, C., and Inoue, A. (1998). Test environments and mechanical properties of Zr-base bulk amorphous alloys. *Metallurgical and Materials Transactions A*, 29(7):1811–1820.
- [Liu et al., 2010] Liu, J., Cao, Q., Chen, L., Wang, X., and Jiang, J. (2010). Shear band evolution and hardness change in cold-rolled bulk metallic glasses. *Acta materialia*, 58(14):4827–4840.
- [Liu et al., 2005] Liu, L., Dai, L., Bai, Y., Wei, B., and Eckert, J. (2005). Behavior of multiple shear bands in Zr-based bulk metallic glass. *Materials Chemistry and Physics*, 93(1):174–177.
- [Liu et al., 2009] Liu, Y., Liu, C. T., Wang, W., Inoue, A., Sakurai, T., and Chen, M. (2009). Thermodynamic origins of shear band formation and the universal scaling law of metallic glass strength. *Physical review letters*, 103(6):065504.
- [Liu et al., 2007] Liu, Y. H., Wang, G., Wang, R. J., Zhao, D. Q., Pan, M. X., and Wang, W. H. (2007). Super plastic bulk metallic glasses at room temperature. *science*, 315(5817):1385–1388.
- [Luo et al., 2004] Luo, W., Sheng, H., Alamgir, F., Bai, J., He, J., and Ma, E. (2004). Icosahedral short-range order in amorphous alloys. *Physical Review Letters*, 92(14):145502.
- [Ma et al., 2009] Ma, W., Kou, H., Li, J., Chang, H., and Zhou, L. (2009). Effect of strain rate on compressive behavior of Ti-based bulk metallic glass at room temperature. *Journal of Alloys and Compounds*, 472(1-2):214–218.

- [Manning and Liu, 2011] Manning, M. L. and Liu, A. J. (2011). Vibrational modes identify soft spots in a sheared disordered packing. *Physical Review Letters*, 107(10):108302.
- [Marmottant and Graner, 2007] Marmottant, P. and Graner, F. (2007). An elastic, plastic, viscous model for slow shear of a liquid foam. *The European Physical Journal E*, 23(4):337–347.
- [Martens et al., 2011] Martens, K., Bocquet, L., and Barrat, J.-L. (2011). Connecting diffusion and dynamical heterogeneities in actively deformed amorphous systems. *Physical review letters*, 106(15):156001.
- [Mattern et al., 2008] Mattern, N., Schöps, A., Kühn, U., Acker, J., Khvostikova, O., and Eckert, J. (2008). Structural behavior of $\text{Cu}_{x}\text{Zr}_{100-x}$ metallic glass ($x=35-70$). *Journal of Non-Crystalline Solids*, 354(10-11):1054–1060.
- [Mayr, 2005] Mayr, S. (2005). Impact of ion irradiation on the thermal, structural, and mechanical properties of metallic glasses. *Physical Review B*, 71(14):144109.
- [Miracle, 2006] Miracle, D. (2006). The efficient cluster packing model—an atomic structural model for metallic glasses. *Acta materialia*, 54(16):4317–4336.
- [Miracle et al., 2003] Miracle, D., Sanders, W., and Senkov, O. (2003). The influence of efficient atomic packing on the constitution of metallic glasses. *Philosophical Magazine*, 83(20):2409–2428.
- [Mukai et al., 2002] Mukai, T., Nieh, T., Kawamura, Y., Inoue, A., and Higashi, K. (2002). Effect of strain rate on compressive behavior of a $\text{Pd}_{40}\text{Ni}_{40}\text{P}_{20}$ bulk metallic glass. *Intermetallics*, 10(11-12):1071–1077.
- [Mura, 2013] Mura, T. (2013). *Micromechanics of defects in solids*. Springer Science & Business Media.
- [Nelson and Spaepen, 1989] Nelson, D. R. and Spaepen, F. (1989). Polytetrahedral order in condensed matter. *Solid State Physics*, 42:1–90.
- [Nicolas et al., 2015] Nicolas, A., Puosi, F., Mizuno, H., and Barrat, J.-L. (2015). Elastic consequences of a single plastic event: towards a realistic account of structural disor-

- der and shear wave propagation in models of flowing amorphous solids. *Journal of the Mechanics and Physics of Solids*, 78:333–351.
- [Nieh et al., 2012] Nieh, T., Yang, Y., Lu, J., and Liu, C. T. (2012). Effect of surface modifications on shear banding and plasticity in metallic glasses: An overview. *Progress in Natural Science: Materials International*, 22(5):355–363.
- [Nosé, 1984] Nosé, S. (1984). A unified formulation of the constant temperature molecular dynamics methods. *The Journal of chemical physics*, 81(1):511–519.
- [Pampillo, 1975] Pampillo, C. A. (1975). Flow and fracture in amorphous alloys. *Journal of Materials Science*, 10(7):1194–1227.
- [Pan et al., 2011] Pan, J., Chen, Q., Liu, L., and Li, Y. (2011). Softening and dilatation in a single shear band. *Acta Materialia*, 59(13):5146–5158.
- [Pan et al., 2017] Pan, J., Wang, Y., and Li, Y. (2017). Ductile fracture in notched bulk metallic glasses. *Acta Materialia*, 136:126–133.
- [Park and Kim, 2010] Park, E. and Kim, D. (2010). Effect of manipulating atomic scale heterogeneity on plasticity in mg-based bulk metallic glasses. *Intermetallics*, 18(10):1867–1871.
- [Park et al., 2007] Park, K.-W., Jang, J.-i., Wakeda, M., Shibutani, Y., and Lee, J.-C. (2007). Atomic packing density and its influence on the properties of cu-zr amorphous alloys. *Scripta Materialia*, 57(9):805–808.
- [Parrinello and Rahman, 1981] Parrinello, M. and Rahman, A. (1981). Polymorphic transitions in single crystals: A new molecular dynamics method. *Journal of Applied physics*, 52(12):7182–7190.
- [Parrinello and Rahman, 1982] Parrinello, M. and Rahman, A. (1982). Strain fluctuations and elastic constants. *The Journal of Chemical Physics*, 76(5):2662–2666.
- [Picard et al., 2004] Picard, G., Ajdari, A., Lequeux, F., and Bocquet, L. (2004). Elastic consequences of a single plastic event: A step towards the microscopic modeling of the flow of yield stress fluids. *The European Physical Journal E*, 15(4):371–381.

- [Priezjev, 2019] Priezjev, N. V. (2019). The effect of cryogenic thermal cycling on aging, rejuvenation, and mechanical properties of metallic glasses. *Journal of Non-Crystalline Solids*, 503:131–138.
- [Qiao, 2013] Qiao, J. (2013). In-situ dendrite/metallic glass matrix composites: a review. *Journal of Materials Science & Technology*, 29(8):685–701.
- [Rahman, 1964] Rahman, A. (1964). Correlations in the motion of atoms in liquid argon. *Physical review*, 136(2A):A405.
- [Ritter, 2012] Ritter, Y. (2012). Molecular dynamics simulations of structure-property relationships in cu-zr metallic glasses.
- [Rodney and Schuh, 2009] Rodney, D. and Schuh, C. (2009). Distribution of thermally activated plastic events in a flowing glass. *Physical review letters*, 102(23):235503.
- [Rodney et al., 2011] Rodney, D., Tanguy, A., and Vandembroucq, D. (2011). Modeling the mechanics of amorphous solids at different length scale and time scale. *Modelling and Simulation in Materials Science and Engineering*, 19(8):083001.
- [Schuh et al., 2007] Schuh, C. A., Hufnagel, T. C., and Ramamurty, U. (2007). Mechanical behavior of amorphous alloys. *Acta Materialia*, 55(12):4067–4109.
- [Şengül and Çeltek, 2018] Şengül, S. and Çeltek, M. (2018). Pressure effects on the structural evolution of monatomic metallic liquid hafnium. *Bitlis Eren Üniversitesi Fen Bilimleri Dergisi*, 7(1):144–158.
- [Sepulveda-Macias et al., 2018] Sepulveda-Macias, M., Gutierrez, G., and Lund, F. (2018). Strain rate and temperature effect on zr50cu50 metallic glass under pure shear. In *Journal of Physics: Conference Series*, volume 1043, page 012040. IOP Publishing.
- [Sergueeva et al., 2005] Sergueeva, A., Mara, N., Kuntz, J., Lavernia, E., and Mukherjee*, A. (2005). Shear band formation and ductility in bulk metallic glass. *Philosophical Magazine*, 85(23):2671–2687.

- [Sha et al., 2011] Sha, Z., Zhang, Y., Feng, Y., and Li, Y. (2011). Molecular dynamics studies of short to medium range order in cu₆₄zr₃₆ metallic glass. *Journal of alloys and compounds*, 509(33):8319–8322.
- [Shang et al., 2018] Shang, B., Guan, P., and Barrat, J.-L. (2018). Role of thermal expansion heterogeneity in the cryogenic rejuvenation of metallic glasses. *Journal of Physics: Materials*, 1(1):015001.
- [Shang et al., 2021] Shang, B., Wang, W., Greer, A. L., and Guan, P. (2021). Atomistic modelling of thermal-cycling rejuvenation in metallic glasses. *Acta Materialia*, 213:116952.
- [Shen et al., 2007] Shen, J., Huang, Y., and Sun, J. (2007). Plasticity of a ticu-based bulk metallic glass: Effect of cooling rate. *Journal of Materials Research*, 22(11):3067–3074.
- [Sheng et al., 2006] Sheng, H., Luo, W., Alamgir, F., Bai, J., and Ma, E. (2006). Atomic packing and short-to-medium-range order in metallic glasses. *Nature*, 439(7075):419–425.
- [Shete et al., 2016] Shete, M. K., Singh, I., Narasimhan, R., and Ramamurty, U. (2016). Effect of strain hardening and volume fraction of crystalline phase on strength and ductility of bulk metallic glass composites. *Scripta Materialia*, 124:51–55.
- [Shimizu et al., 2006] Shimizu, F., Ogata, S., and Li, J. (2006). Yield point of metallic glass. *Acta materialia*, 54(16):4293–4298.
- [Shimizu et al., 2007] Shimizu, F., Ogata, S., and Li, J. (2007). Theory of shear banding in metallic glasses and molecular dynamics calculations. *Materials transactions*, pages 0710160231–0710160231.
- [Song et al., 2017] Song, H., Li, S., Zhang, Y., Deng, Q., Xu, T., and Li, Y. (2017). Atomic simulations of plastic deformation behavior of cu₅₀zr₅₀ metallic glass. *Journal of Non-Crystalline Solids*, 471:312–321.
- [Song et al., 2019] Song, H., Wang, M., An, M., and Li, Y. (2019). Enhancing the plasticity of noncrystalline cuzr multilayer: Insights from molecular dynamics simulations. *Journal of Non-Crystalline Solids*, 507:11–18.

- [Song et al., 2018] Song, W., Meng, X., Wu, Y., Cao, D., Wang, H., Liu, X., Wang, X., and Lu, Z. (2018). Improving plasticity of the zr46cu46al8 bulk metallic glass via thermal rejuvenation. *Science Bulletin*, 63(13):840–844.
- [Şopu et al., 2011] Şopu, D., Ritter, Y., Gleiter, H., and Albe, K. (2011). Deformation behavior of bulk and nanostructured metallic glasses studied via molecular dynamics simulations. *Physical Review B*, 83(10):100202.
- [Spaepen, 1977] Spaepen, F. (1977). A microscopic mechanism for steady state inhomogeneous flow in metallic glasses. *Acta metallurgica*, 25(4):407–415.
- [Spaepen and Turnbull, 1984] Spaepen, F. and Turnbull, D. (1984). Metallic glasses. *Annual Review of Physical Chemistry*, 35(1):241–263.
- [Steif et al., 1982] Steif, P., Spaepen, F., and Hutchinson, J. (1982). Strain localization in amorphous metals. *Acta Metallurgica*, 30(2):447–455.
- [Stepanov, 2013] Stepanov, I. (2013). *Modelling of Fluid Fragmentation by Molecular Dynamics*. PhD thesis, University of Sheffield.
- [Stillinger and Weber, 1985] Stillinger, F. H. and Weber, T. A. (1985). Computer simulation of local order in condensed phases of silicon. *Physical review B*, 31(8):5262.
- [Stott and Zaremba, 1980] Stott, M. and Zaremba, E. (1980). Quasiatoms: An approach to atoms in nonuniform electronic systems. *Physical Review B*, 22(4):1564.
- [Stukowski, 2009] Stukowski, A. (2009). Visualization and analysis of atomistic simulation data with ovito—the open visualization tool. *Modelling and simulation in materials science and engineering*, 18(1):015012.
- [Su and Anand, 2006] Su, C. and Anand, L. (2006). Plane strain indentation of a zr-based metallic glass: experiments and numerical simulation. *Acta materialia*, 54(1):179–189.
- [Sun and Shen, 2009] Sun, Y. and Shen, J. (2009). Icosahedral ordering in cu60zr40 metallic glass: Molecular dynamics simulations. *Journal of non-crystalline solids*, 355(31-33):1557–1560.

- [Swope et al., 1982] Swope, W. C., Andersen, H. C., Berens, P. H., and Wilson, K. R. (1982). A computer simulation method for the calculation of equilibrium constants for the formation of physical clusters of molecules: Application to small water clusters. *The Journal of chemical physics*, 76(1):637–649.
- [Talamali et al., 2011] Talamali, M., Petäjä, V., Vandembroucq, D., and Roux, S. (2011). Avalanches, precursors, and finite-size fluctuations in a mesoscopic model of amorphous plasticity. *Physical Review E*, 84(1):016115.
- [Tanguy et al., 2006] Tanguy, A., Leonforte, F., and Barrat, J.-L. (2006). Plastic response of a 2d lennard-jones amorphous solid: Detailed analysis of the local rearrangements at very slow strain rate. *The European Physical Journal E*, 20(3):355–364.
- [Telford, 2004] Telford, M. (2004). The case for bulk metallic glass. *Materials today*, 7(3):36–43.
- [Trexler and Thadhani, 2010] Trexler, M. M. and Thadhani, N. N. (2010). Mechanical properties of bulk metallic glasses. *Progress in Materials Science*, 55(8):759–839.
- [Velasco et al., 2017] Velasco, J. E., Concustell, A., Pineda, E., and Crespo, D. (2017). Plastic deformation induced anisotropy in metallic glasses: A molecular dynamics study. *Journal of Alloys and Compounds*, 707:102–107.
- [Verlet, 1967] Verlet, L. (1967). Computer" experiments" on classical fluids. i. thermodynamical properties of lennard-jones molecules. *Physical review*, 159(1):98.
- [Wakeda et al., 2015] Wakeda, M., Saida, J., Li, J., and Ogata, S. (2015). Controlled rejuvenation of amorphous metals with thermal processing. *Scientific reports*, 5(1):1–8.
- [Wang and Wong, 2012] Wang, C. and Wong, C. (2012). Structural properties of zrxcu90-xal10 metallic glasses investigated by molecular dynamics simulations. *Journal of alloys and compounds*, 510(1):107–113.
- [Wang et al., 2009] Wang, J., Hodgson, P. D., Zhang, J., Yan, W., and Yang, C. (2009). Effects of quenching rate on amorphous structures of cu46zr54 metallic glass. *Journal of materials processing technology*, 209(9):4601–4606.

- [Wang et al., 2011] Wang, L., Bei, H., Gao, Y., Lu, Z. P., and Nieh, T. (2011). Effect of residual stresses on the onset of yielding in a zr-based metallic glass. *Acta materialia*, 59(20):7627–7633.
- [Wang et al., 2004] Wang, W.-H., Dong, C., and Shek, C. (2004). Bulk metallic glasses. *Materials Science and Engineering: R: Reports*, 44(2-3):45–89.
- [Wang et al., 2015] Wang, Y., Hao, G., Zhang, Y., Qiao, J., and Lin, J. (2015). Effect of temperature on mechanical properties of ti-based metallic glass matrix composite. *Intermetallics*, 67:121–126.
- [Weihua, 2013] Weihua, W. (2013). The nature and characteristics of amorphous matter. *Progress in Physics*, 33(5):177–351.
- [Wen et al., 2021] Wen, P., Demaske, B., Spearot, D. E., Phillpot, S. R., and Tao, G. (2021). Effect of the initial temperature on the shock response of cu50zr50 bulk metallic glass by molecular dynamics simulation. *Journal of Applied Physics*, 129(16):165103.
- [Xiao et al., 2010] Xiao, Y., Wu, Y., Liu, Z., Wu, H., and Lü, Z. (2010). Effects of cooling rates on the mechanical properties of a ti-based bulk metallic glass. *Science China Physics, Mechanics and Astronomy*, 53(3):394–398.
- [Xing et al., 2001] Xing, L.-Q., Li, Y., Ramesh, K., Li, J., and Hufnagel, T. (2001). Enhanced plastic strain in zr-based bulk amorphous alloys. *Physical review B*, 64(18):180201.
- [Yan et al., 2007] Yan, M., Shen, J., Sun, J., and Zou, J. (2007). Cooling rate dependent as-cast microstructure and mechanical properties of zr-based metallic glasses. *Journal of materials science*, 42(12):4233–4239.
- [Yang et al., 2006a] Yang, B., Liu, C., Nieh, T., Morrison, M., Liaw, P., and Buchanan, R. (2006a). Localized heating and fracture criterion for bulk metallic glasses. *Journal of materials research*, 21(4):915–922.
- [Yang et al., 2006b] Yang, B., Liu, C. T., and Nieh, T. (2006b). Unified equation for the strength of bulk metallic glasses. *Applied Physics Letters*, 88(22):221911.

- [Yang et al., 2005] Yang, B., Morrison, M. L., Liaw, P. K., Buchanan, R. A., Wang, G., Liu, C. T., and Denda, M. (2005). Dynamic evolution of nanoscale shear bands in a bulk-metallic glass. *Applied Physics Letters*, 86(14):141904.
- [YL et al., 1992] YL, B., Dodd, B., et al. (1992). *Adiabatic shear localization: occurrence, theories, and applications*. Pergamon Press.
- [Yokoyama, 2003] Yokoyama, Y. (2003). Ductility improvement of zr-cu-ni-al glassy alloy. *Journal of Non-Crystalline Solids*, 316(1):104–113.
- [Yokoyama et al., 2002] Yokoyama, Y., Inoue, K., and Fukaura, K. (2002). Cold-rolled zr50cu30ni10al10 bulk amorphous alloys with tensile plastic elongation at room temperature. *Materials Transactions*, 43(12):3199–3205.
- [Yoo et al., 2009] Yoo, B.-G., Kim, Y.-J., Oh, J.-H., Ramamurty, U., and Jang, J.-i. (2009). On the hardness of shear bands in amorphous alloys. *Scripta Materialia*, 61(10):951–954.
- [Yu et al., 2011] Yu, P., Chan, K. C., Chen, W., and Xia, L. (2011). Low-temperature mechanical properties of ce68al10cu20co2 bulk metallic glass. *Philosophical Magazine Letters*, 91(1):70–77.
- [Yue et al., 2020] Yue, X., Brechtel, J., Wang, F., Chang, Z., Liaw, P. K., and Fan, C. (2020). Deformation behavior of annealed cu64zr36 metallic glass via molecular dynamics simulations. *Materials & Design*, 191:108660.
- [Yue et al., 2018] Yue, X., Liu, C., Pan, S., Inoue, A., Liaw, P., and Fan, C. (2018). Effect of cooling rate on structures and mechanical behavior of cu50zr50 metallic glass: a molecular-dynamics study. *Physica B: Condensed Matter*, 547:48–54.
- [Zemp et al., 2014] Zemp, J., Celino, M., Schönfeld, B., and Löffler, J. F. (2014). Icosahedral superclusters in cu 64 zr 36 metallic glass. *Physical Review B*, 90(14):144108.
- [Zhang et al., 2007] Zhang, J., Park, J. M., Kim, D. H., and Kim, H. S. (2007). Effect of strain rate on compressive behavior of ti45zr16ni9cu10be20 bulk metallic glass. *Materials Science and Engineering: A*, 449:290–294.

- [Zhang et al., 2003] Zhang, Z., Eckert, J., and Schultz, L. (2003). Difference in compressive and tensile fracture mechanisms of $\text{Zr}_{59}\text{Cu}_{20}\text{Al}_{10}\text{Ni}_8\text{Ti}_3$ bulk metallic glass. *Acta Materialia*, 51(4):1167–1179.
- [Zhao et al., 2010a] Zhao, J., Qu, R., Wu, F., Li, S., and Zhang, Z. (2010a). Deformation behavior and enhanced plasticity of Ti-based metallic glasses with notches. *Philosophical Magazine*, 90(29):3867–3877.
- [Zhao et al., 2010b] Zhao, J., Wu, F., Qu, R., Li, S., and Zhang, Z. (2010b). Plastic deformability of metallic glass by artificial macroscopic notches. *Acta Materialia*, 58(16):5420–5432.
- [Zhong et al., 2016] Zhong, C., Zhang, H., Cao, Q., Wang, X., Zhang, D., Ramamurty, U., and Jiang, J. (2016). Deformation behavior of metallic glasses with shear band like atomic structure: a molecular dynamics study. *Scientific reports*, 6(1):1–12.
- [Zhou et al., 2013] Zhou, H., Qu, S., and Yang, W. (2013). An atomistic investigation of structural evolution in metallic glass matrix composites. *International Journal of Plasticity*, 44:147–160.

FOLIO ADMINISTRATIF

THESE DE L'UNIVERSITE DE LYON OPEREE AU SEIN DE L'INSA LYON

NOM : LIANG
(avec précision du nom de jeune fille, le cas échéant)

DATE de SOUTENANCE : le 9 décembre 2022

Prénoms : Meng

TITRE : Analysis of small-scale plasticity of bulk Cu-Zr metallic glasses under deformation by atomistic simulations

NATURE : Doctorat

Numéro d'ordre : 2022ISAL0115

Ecole doctorale : ED 34 Matériaux de Lyon

Spécialité : Science des Matériaux

RESUME : Les verres métalliques sont de nouveaux matériaux très prometteurs du fait de leurs excellentes propriétés mécaniques. Ils ont potentiellement de nombreuses applications en micromécanique, microélectronique, bijouterie, dans le domaine biomédical, l'aérospatial et bien d'autres domaines. Cependant, leur faible plasticité à température ambiante limite pour l'instant leur large diffusion dans l'industrie. Par conséquent, l'amélioration de leur ductilité est devenue un enjeu majeur pour la science des matériaux. L'objectif de cette thèse est ainsi d'étudier la plasticité de verres métalliques préparés sous différentes conditions, par des simulations de dynamique moléculaire (MD) et de caractériser les événements plastiques survenant à l'échelle microscopique pendant leur déformation afin de comprendre comment la plasticité évolue, et finalement d'évaluer sous quelles conditions la ductilité peut être améliorée.

Le système étudié dans cette thèse est un modèle binaire Cu-Zr. Nous avons étudié l'effet de la vitesse de trempe, de la composition, de la vitesse de déformation et de la température. Nos simulations montrent que lors de déformations en cisaillement quasi-statique, la plasticité des verres Cu-Zr est plus homogène, c'est-à-dire que la localisation des déformations et la formation des bandes de cisaillement sont plus limitées, lorsque ces matériaux sont préparés avec des vitesses de trempe plus élevées, lorsqu'ils contiennent moins de cuivre, et/ou lorsqu'ils sont soumis à des vitesses de déformation et/ou des températures plus élevées.

Afin de comprendre les mécanismes microscopiques impliqués dans cette plasticité, nous avons développé une méthode pour identifier et caractériser les événements plastiques individuels. De cette façon, nous pouvons évaluer leur nombre, leur intensité plastique, leur taille moyenne et leur orientation. De plus, nous sommes capables de reconstruire le comportement mécanique simulé en considérant les événements plastiques comme des inclusions d'Eshelby dans une matrice élastique infinie.

Enfin, nous montrons que le cyclage thermique sous la température de transition vitreuse peut être, dans certaines conditions, un moyen efficace d'améliorer la ductilité des verres métalliques, via leur rajeunissement.

MOTS-CLÉS : Verres métalliques; Dynamique Moléculaire; plasticité ; propriétés mécaniques; cyclage thermique
Laboratoire (s) de recherche : Laboratoire MATEIS - INSA Lyon

Directeur de thèse: Laurent CHAZEAU INSA Lyon
 Claudio FUSCO INSA Lyon

Président de jury : Anne TANGUY INSA Lyon

Composition du jury : Rapporteur : Alain DEQUIDT, Université Clermont Auvergne
 Rapporteur : Jichao QIAO, Northwestern Polytechnical University
 Examinatrice : Kirsten MARTENS, Université Grenoble Alpes
 Invité: Julien MORTHOMAS, INSA Lyon
 Invité: Tristan ALBARET, Université Lyon 1

BIBLIOGRAPHY
